Set up and test of a cryogenic distillation column for the XENON1T experiment

Michael Murra

Master thesis

Institut für Kernphysik
Mathematisch-Naturwissenschaftliche Fakultät
Westfälische Wilhelms-Universität Münster

January 2014

Referent: Prof. Dr. C. Weinheimer

Koreferent: Prof. Dr. A. Khoukaz

WESTFÄLISCHE
WILHELMS-UNIVERSITÄT
MÜNSTER

Eigenständigkeitserklärung

Hiermit versichere ich, dass ich die vorliegende Arbeit mit dem Titel:

Set up and test of a cryogenic distillation column for the XENON1T experiment

selbständig verfasst habe, und dass ich keine anderen Quellen und Hilfsmittel als die angegebenen benutzt habe und dass die Stellen der Arbeit, die anderen Werken – auch elektronischen Medien – dem Wortlaut oder Sinn nach entnommen wurden, auf jeden Fall unter Angabe der Quelle als Entlehnung kenntlich gemacht worden sind.

_____

Ort, Datum   Unterschrift

Contents

1 Introduction

Chasing after a newly predicted, highly unknown, invisible yet noticeable matter that nobody has been able to detect so far has become the subject of contemporary research and scientific discussions in recent decades. In the hopes of discovering at least one possible representative of the ever elusive dark matter - namely, the Weakly Interacting Massive Particle (WIMP) - a number of experiments have been called into existence to achieve this goal.

The XENON Dark Matter Project represents one such experiment active in the field of direct WIMP detection. Using a xenon dual-phase time projection chamber, it measures an energy deposition in the detector by the scattering process of WIMPs with xenon nuclei. While the XENON100 experiment with its fiducial detector volume of $62\,\text{kg}$ was recently surpassed by the Large Underground Xenon dark matter experiment (LUX), it did set the most stringent upper limit of a spin-independent WIMP nucleon cross section in 2012. The next generation experiment XENON1T with a liquid xenon amount on the ton scale and with an expected sensitivity of more than one order of magnitude better than current experiments is already under construction.

For such high detector volumes, the internal background, introduced by intrinsic contaminations of the used target material xenon, is one of the most critical parameters of the final background level and thus of the sensitivity of the detector.

The concentration of the radioactive isotope ^{85}Kr in commercial available xenon as one intrinsic background source has to be reduced by a factor of 10^4 - 10^5, which can be achieved due to the different chemical properties of xenon and krypton with the help of cryogenic distillation. The functionality of a new distillation column for the XENON1T experiment, which has been designed and assembled by the collaboration group in Muenster, is currently investigated. The construction and first tests of the cryogenic system have been the main topic of this thesis.

Initially, to introduce this thesis, a brief presentation of the important pieces of evidence and properties of dark matter as well as the WIMP as a dark matter candidate will be given, followed by an overview of the XENON100 experiment, along with the design of the new XENON1T experiment.

Afterwards, the design of the new cryogenic distillation column will be explained on the basis of the McCabe-Thiele method, which can be used to determine the final height of the column tube. The construction and assembling of the different components as well as the measurement and slowcontrol system will be shown subsequently.

Lastly, at the end of this thesis, first tests with the distillation column will be presented, such as a cooling power test of a coldhead as well as a conductance measurement of a special custom-made cold valve. In addition, an example for one filling process of the column and one example for a stable distillation operation will be explained. As a brief outlook, one possible method for the determination of the separation efficiency of the cryogenic distillation will be shown, using ^{83m}Kr as radioactive tracer.

2 Dark Matter

In the past few decades, a lot of independent observations have formed an image of our universe, in which it is dominated by two components whose exact nature is still widely unknown. One is a new kind of matter, called dark matter, which is not perceivable by any interaction except the gravitational one. The second one is an almost perfectly uniformly distributed energy density, responsible for the acceleration of the expansion of the universe, called dark energy. These two components make up about 96 % of the energy density in contrast to the mere 4 % made of the standard model particles we originally thought of as the main constituents.

This chapter will introduce the most important pieces of evidence for dark matter, such as rotation curves of galaxies, gravitational lensing and the cosmic microwave background, and will present the most common candidate, the *Weakly Interacting Massive Particle* (WIMP). Furthermore, the different detection principles will be explained.

2.1 Evidence for dark matter

The first hint for the existence of dark matter was discovered by Fritz Zwicky in the 1930s. He was interested in the mass distribution of galaxies in the Coma cluster, which he calculated in two different ways: Firstly, he determined the mass distribution based on the number and luminosity of the galaxies. Secondly, he used an application of the virial theorem to compute the mass content of the cluster. This theorem relates the average over time of the total kinetic energy in a stable system with N particles with that of the total potential energy. A simplified version is shown in the following equation:

$$M_{tot}^2 \ \sim \ \langle E_{pot} \rangle = -2 \langle E_{kin} \rangle \ \sim \ v_{kin}^2 \tag{2.1}$$

By observing the motion of the galaxies inside the cluster (v_{kin}) he was able to calculate the total mass content (M_{tot}). The detailed calculation is shown in [Zwi37]. His findings concluded, that the motion based calculation was 400 times higher [Zwi37]. As a result of this, he suggested that there must be some form of hidden matter inside the galaxies, which cannot be observed in the visible light. He dubbed it *dark matter*.

2.1.1 Rotation curves of galaxies

Another evidence, confirming the existence of dark matter, was given by measuring the rotation velocity of spiral galaxies.

In a spiral galaxy, most of the luminous mass is located in the center around a black hole. By measuring the Doppler effect of the 21 cm hyperfine transition line of hydrogen, the rotation velocities

in dependence of the distance from the center can be obtained [Beg91]. For larger distances it was measured that the rotation velocities stay constant, which is shown in figure 2.1 for the galaxy NGC 6503.

However, according to the Newtonian dynamics, one would expect for stars of the outer arms of the spiral, with large radii, to move around the center of mass on a satellite-like track, that is, a body orbiting a central mass, with a rotation velocity dependence given by

$$v(r) \sim \frac{1}{\sqrt{r}}. \tag{2.2}$$

To compensate for this discrepancy, a mass distribution made of a halo of dark matter around the galaxy was introduced to the model. The observed curve is a composition of the expected rotation velocities given by the galactic disk, the galactic gas and the dark matter halo.
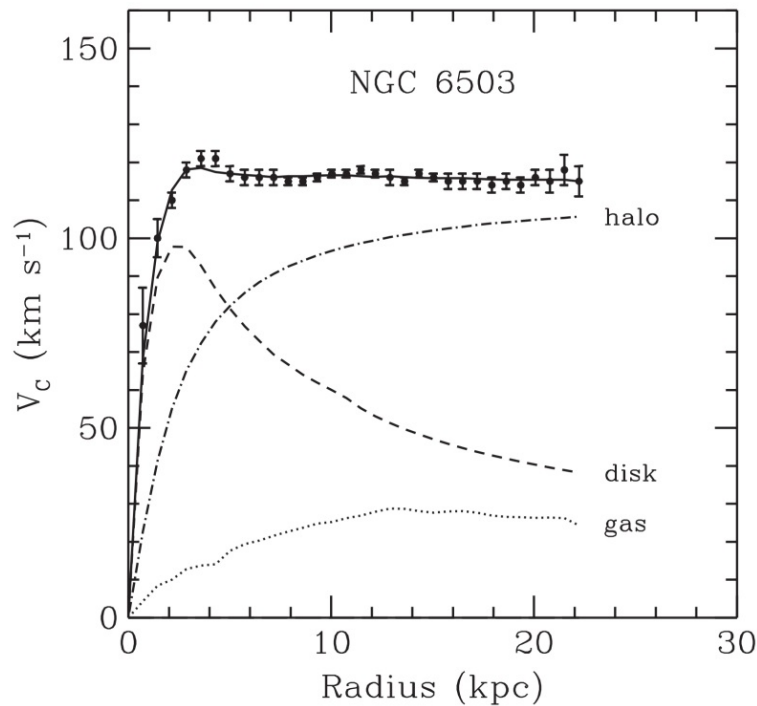
Figure 2.1: *Rotation curve of the spiral galaxy NGC 6503. The data points show the measurement of the circular rotation velocities in dependence of the distance from the galactic center. The data can be explained by a composition of the different rotation velocities induced by the galactic disk, the gas and a dark matter halo [Beg91].*

2.1.2 Gravitational lensing

In general relativity Albert Einstein predicted, that in presence of matter, the spacetime can be curved and the path of light is deflected as a result of this. In analogy to lenses in optics the bending object

is called gravitational lens.

A system where lensing occurs consists of a light source, the lens, an observer and an image. The light that is sent out by the source is deflected by the lens related to the amount of mass that the bending object has. Because of the bent spacetime and thus the bent path of the light, the observer sees a different amount of light and therefore a distorted image. A two-dimensional basic scheme is shown in figure 2.2.
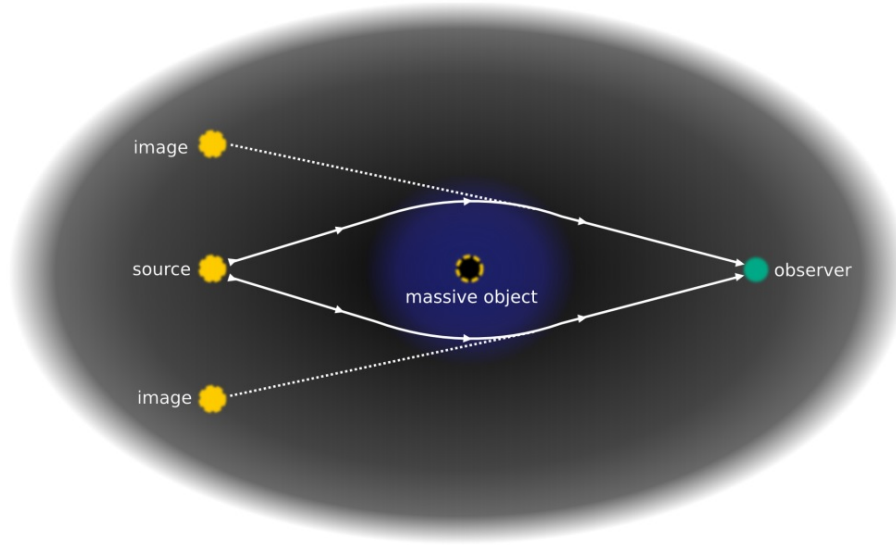

Figure 2.2: *Basic scheme of gravitational lensing. The light coming from the source behind a massive object, the gravitational lens, is deflected through the curvature of spacetime. Because of this, the observer will see several images under different angles [Sch11].*

Vice versa, it is possible to determine the amount of mass that the gravitational lens, e.g. a galaxy cluster, possesses by calculating the strength of the deflection. In parallel, one can obtain the mass of the luminous matter in the cluster with X-ray measurements. The comparison shows a discrepancy in the quantity of mass, which hints at the existence of dark matter.

One related example is the so-called *Bullet Cluster*, a system of two galaxy clusters, which collided about 150 million years ago. In a classical model, the clusters consist of mainly hot diffuse gas and a few percent of stellar components, which are described as point-like objects. When the two clusters intermixed, the stellar components only interacted gravitationally and therefore passed without any collisions. The gas interacted electromagnetically and slowed down due to friction. On the grounds of this discovery, one would expect, that the gravitational potential lies at the center of mass, where the slowed down gas is focused. Figure 2.3 shows that most of the mass is still located in the center of the clusters (green lines), which is measured through gravitational lensing, and clearly displaced from the hot gas (color-coded areas), which is determined by X-ray measurements [Clo06]. That paradox cannot be explained on the basis of the classical model, but it can be explained with the presence of dark matter. If the main part of the clusters were to be dark matter, which also only interacts gravitationally, then the two centers of mass would be bound to pass each other unaffected. That is
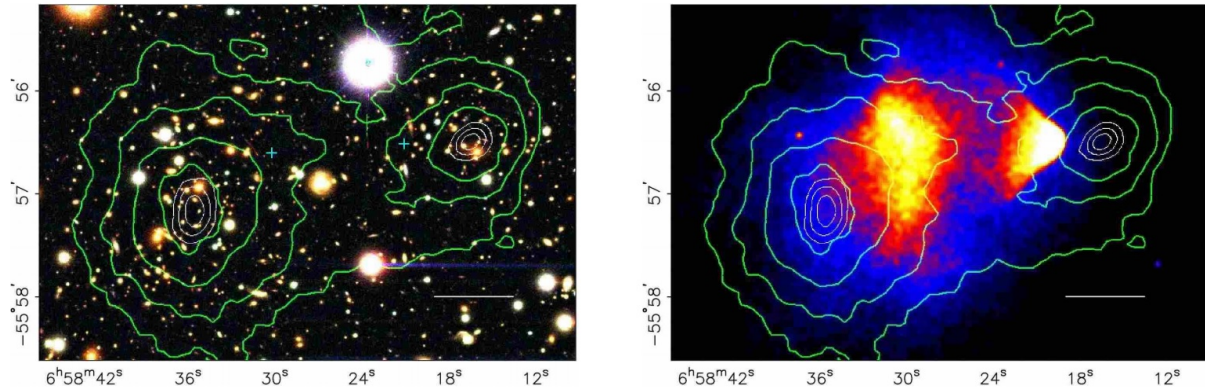
Figure 2.3: *Shown in the left panel is a color image from the Magellan images of the merging cluster 1E0657558. In the right panel is a Chandra image of the cluster. The blue +s (left panel) show the location of the centers used to measure the masses of the plasma clouds (color-coded area on right panel) that are clearly displaced from the actual centers of mass shown in green contours in both panels measured via weak gravitational lensing. Figure taken from [Clo06].*

very strong evidence for dark matter.

2.1.3 Cosmic microwave background radiation

The most precise determination of the quantity and one of the strongest arguments for the existence of dark matter, lies within the *Cosmic Microwave Background* (CMB) radiation, which consists of almost perfect isotropic distributed photons from the early universe.

At that time the energy density and the temperature were so high, that no neutral atoms or molecules could form, but that matter was nearly isotropically distributed as plasma. The plasma was so dense that photons were absorbed immediately and had no chance to escape. Due to expansion, the universe cooled down more and more. At some point, about 380,000 years after the *big bang*, the ionized atoms were able to recombine. Hence, the photons decoupled from matter and propagated freely in the now transparent universe until today. Because of the red-shift, the relic photons nowadays have a wavelength in the region of microwaves.

The measured spectral distribution is the most accurate blackbody radiation measurement of all time. It gives off a body temperature of $(2.7255 \pm 0.0006)\,\mathrm{K}$ [Fix09].

In precise measurements of the CMB, fluctuations in the range of µK can be observed. These anisotropies in temperature are directly linked to the matter distribution and are therefore the energy density at the point of recombination in the early universe. The fluctuations are usually expanded in terms of spherical harmonics that lead to an angular power spectrum, in which the power of the anisotropies is plotted in terms of a multipole moment and angular scale. In figure 2.4, a spectrum from the most recent Planck data is shown.

The angular power spectrum is dependent upon several parameters, which are composed in the ΛCDM model, such as the baryon density, the cold dark matter density and the dark energy density, to name
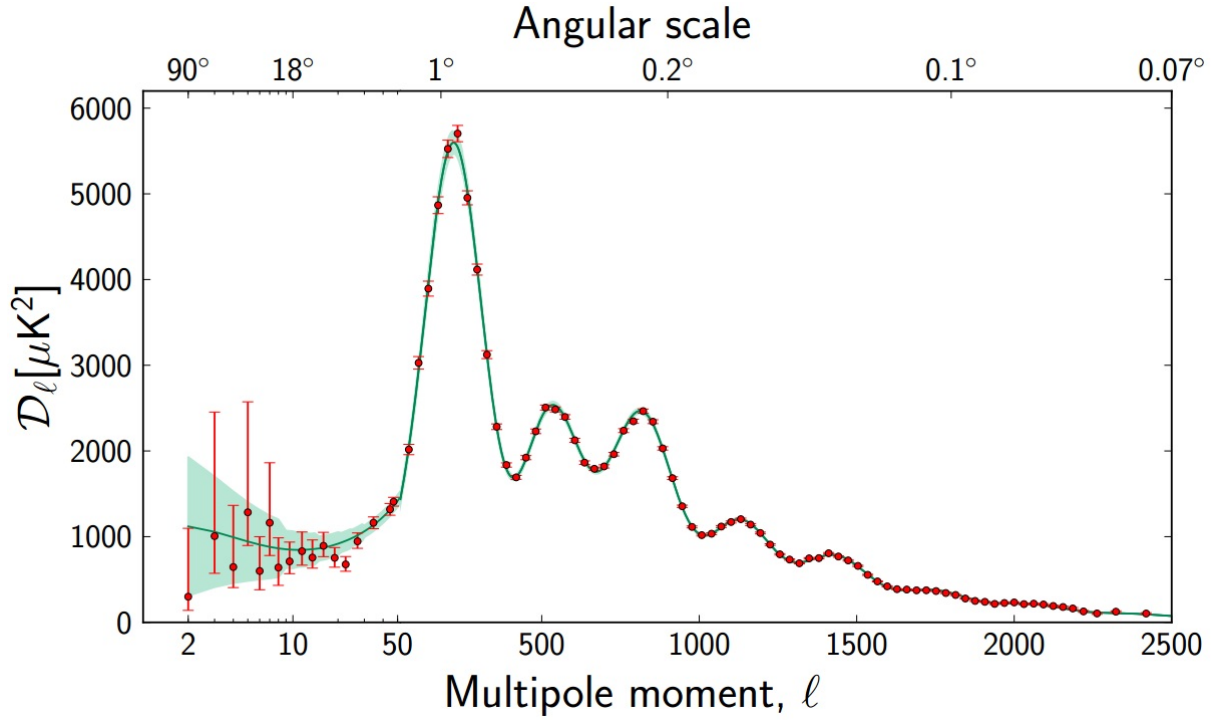
Figure 2.4: *The power spectrum of the CMB. The variation in temperature fluctuations (D_ℓ) in dependence of the multipole moment ℓ and the angular scale are shown. The fit for the recent Planck data is coming from a six parameter fit of the ΛCDM model, that provides information about the universe, such as the amount of dark energy, baryonic matter and dark matter. The error bars include cosmic variance, whose magnitude is indicated by the green shaded area around the best fit model. For $\ell \leq 50$ the plot is linear, after that, it has a logarithm scale [Pla13a].*

three of these parameters. Thus, by measuring the anisotropies in temperature, it is possible to place constraints on the cosmological parameters [Pla13a].

The actual computations for the energy density provide the following distribution:

$$\sim 68.3\,\% \text{ dark energy}$$
$$\sim \ \ 4.9\,\% \text{ baryonic matter}$$
$$\sim 26.8\,\% \text{ dark matter}$$

For detailed information see [Pla13a] and [Pla13b].

2.2 Dark matter candidates

As discussed in the previous section, there is overwhelming evidence for the existence of non-baryonic dark matter. In the next step the question arises of what kind of particle this matter is comprised of. The candidate needs to fulfill several constraints, coming from the observations of the different influences by dark matter. First off, there must not be interactions with photons, otherwise dark matter could be seen by absorbing or emitting light. If they do exist, they have to be intensely weak. Interactions with baryons should also be very weak, otherwise one would observe similar dark matter and baryonic disks in galaxies. The *Bullet Cluster* shows that the centers of mass in the clusters went through each other nearly unaffected. Therefore, the self-interaction between the dark matter particles must also be small. Furthermore, the candidate must be stable on the scale of the age of the universe. There is one type of particle from the Standard Model of particle physics, meeting all of these constraints: The neutrinos. However, CMB anisotropy measurements combined with large-scale structure data suggest that the physical neutrino density is constrained to be $\Omega_\nu h^2 < 0.0067$ (95% confidence limit) [Ber04] and thus clearly not abundant enough to compose a significant fraction of the dark matter.

Neutrinos also propagate with ultra-relativistic speed through the universe and are therefore too fast to explain the structure formation in the early universe, shown with N-body simulations in [Whi83]. They belong to the class of the so-called *hot dark matter* and only make up a small fraction of dark matter.

At the time where structure formation started, most of the dark matter had to have been *cold*, propagating with non-relativistic speed, to be able to clump and form galaxies and clusters due to gravitational force. Numerical N-body simulations of structure formation agree with most of the observed structures predicted by cold dark matter [Ost03].

The experiment this thesis is contributing to wants to detect one of the cold dark matter candidates, the *Weakly Interacting Massive Particle* (WIMP). This candidate and the connected theoretical model, the supersymmetry, will be briefly presented in the next sections.

2.2.1 Supersymmetry

The standard model (SM) of particle physics is a well-established theory and sufficiently describes the electromagnetic, weak, and strong interactions between the 12 constituents of matter, called fermions (quarks and leptons). The different forces are mediated via 12 bosons, namely γ, Z^0, $W^\pm$ and g_8.

Nevertheless, pieces of evidence for physics beyond the SM emerged and rose in the recent years. The concept of dark matter and dark energy, for example, cannot be explained by SM. Furthermore, experiments about neutrino oscillation showed that neutrinos are not massless as has previously been claimed by the SM. Also in theory, there are several aspects, that could not be explained by the SM alone. There is the gauge hierarchy problem, where the mass of the Higgs boson with m$\sim$125.5 GeV [Con13] is much lighter than the planck mass with m=1.2×10^{19} GeV [Fen10]. Another problem is the model of a grand unified theory, in which the strong, weak, and electromagnetic interactions can be understood as different manifestations of a single underlying force. These are just a few examples for the motivation of new theories beyond the standard model that are described in more detail in [Fen10]. Consequently, several extensions to the SM have been proposed, and one of these extensions is the so-called *supersymmetry* (SUSY), in which the SM is a special case for low energies [Ber04].

In SUSY, every particle of the standard model, effectively exists with a supersymmetric partner,
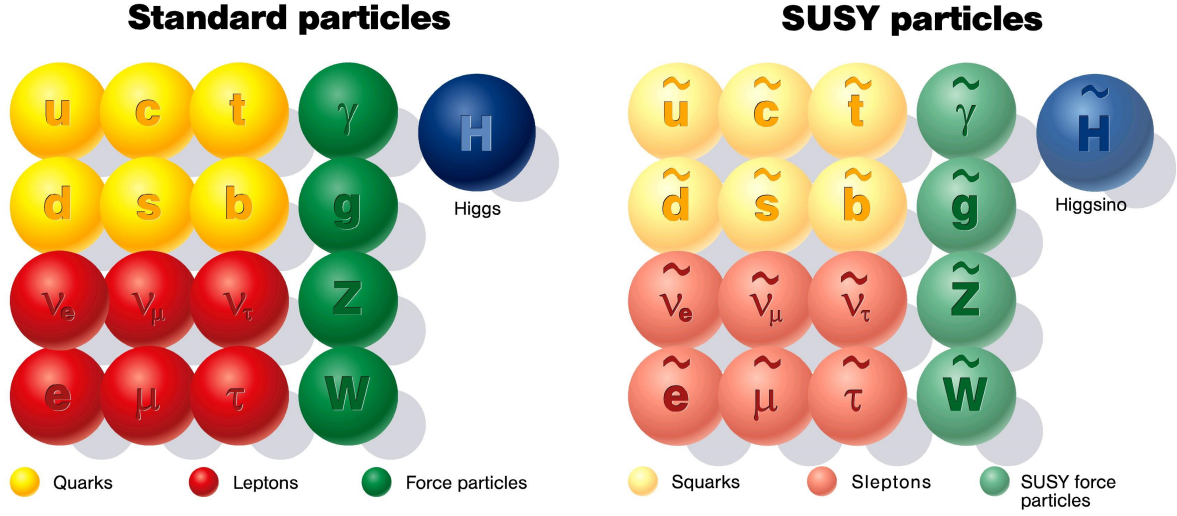

Figure 2.5: *Standard Model particles (left) and their corresponding supersymmetric partners (right) [Des05].*

so that bosons would have a supersymmetric fermion partner and fermions a supersymmetric boson partner, as shown in figure 2.5. In the case of an exact symmetry, all their quantum numbers except for the spin would be the same for a pair of SUSY partners, including mass. Due to the fact that no supersymmetric particles have been found at collider experiments yet, SUSY must be a broken symmetry to allow higher masses for the SUSY particles [Jun96].

One can introduce the multiplicative quantum number R-parity, which is −1 for SUSY particles and 1 for SM particles. Because R is a conserved quantity, the lightest stable particle (LSP) of this model cannot decay into standard model particles [Jun96]. With that, the model of supersymmetry, designed to address the gauge hierarchy problem, as one example, naturally predicts new particles with mass $m_{weak} \approx 10\,\text{GeV}-\text{TeV}$ that are stable and have the thermal relic density required to be dark matter.

2.2.2 The WIMP

For one model of supersymmetry, the *minimal supersymmetric standard model* (MSSM), the lightest stable particle is the neutralino χ, which is a linear combination of two higgsinos and two superpartners of gauge fields, the wino and the bino as listed in table 2.1.

It is one representative for the class of WIMPs. Assuming that the neutralino is a majorana particle, which would make it its own anti-particle and assuming that it interacts on the weak-scale, dark matter may be produced in a simple and predictive manner as a thermal relic of the big bang.

At the beginning, the early universe was hot and dense. Thus, all particles were in thermal equilibrium and the following reactions were allowed:

$$\chi + \chi \longleftrightarrow SM + SM, \tag{2.3}$$

Table 2.1: *Particles of the minimal supersymmetric standard model. Table taken from [Ber04].*

| Standard Model particles and fields | | Supersymmetric partners | | | |
| | | Interaction eigenstates | | Mass eigenstates | |
Symbol	Name	Symbol	Name	Symbol	Name
$q = d, c, b, u, s, t$	quark	$\tilde{q}_L, \tilde{q}_R$	squark	$\tilde{q}_1, \tilde{q}_2$	squark
$l = e, \mu, \tau$	lepton	$\tilde{l}_L, \tilde{l}_R$	slepton	$\tilde{l}_1, \tilde{l}_2$	slepton
$\nu = \nu_e, \nu_\mu, \nu_\tau$	neutrino	$\tilde{\nu}$	sneutrino	$\tilde{\nu}$	sneutrino
g	gluon	$\tilde{g}$	gluino	$\tilde{g}$	gluino
$W^\pm$	W-boson	$\tilde{W}^\pm$	wino		
H^-	Higgs boson	$\tilde{H}_1^-$	higgsino	$\tilde{\chi}_{1,2}^\pm$	chargino
H^+	Higgs boson	$\tilde{H}_2^+$	higgsino		
B	B-field	$\tilde{B}$	bino		
W^3	W^3-field	$\tilde{W}^3$	wino		
H_1^0	Higgs boson			$\tilde{\chi}_{1,2,3,4}^0$	neutralino
H_2^0	Higgs boson	$\tilde{H}_1^0$	higgsino		
H_3^0	Higgs boson	$\tilde{H}_2^0$	higgsino		

where χ indicates a dark matter particle and SM a standard model particle. While cooling more and more the universe reached a temperature T, at some point, below the mass m_χ of the dark matter particles and as a result of this the reactions above were no longer possible, because there was not enough energy to produce dark matter particles any more. Additionally, the number of dark matter particles became Boltzmann suppressed, dropping exponentially with $e^{-m_\chi/T}$ and would have dropped to zero, if there had not been an expansion of the universe. While the universe got larger the dark matter particles became so diluted that they could not find each other anymore to annihilate. They *froze out* with a number asymptotically approaching a constant, their thermal relic density that is given by:

$$\Omega_\chi h^2 = \frac{3 \cdot 10^{-27}\,\mathrm{cm^3/s}}{\langle \sigma_A v \rangle} \tag{2.4}$$

For a dark matter particle with an annihilation cross section $\langle \sigma_A v \rangle$ on the weak-scale, equation 2.4 naturally gives the right relic density required for dark matter. Detailed derivations and calculations can be found in [Jun96].

This phenomena is often referred as *WIMP miracle*. The described mechanism is also shown in figure 2.6.
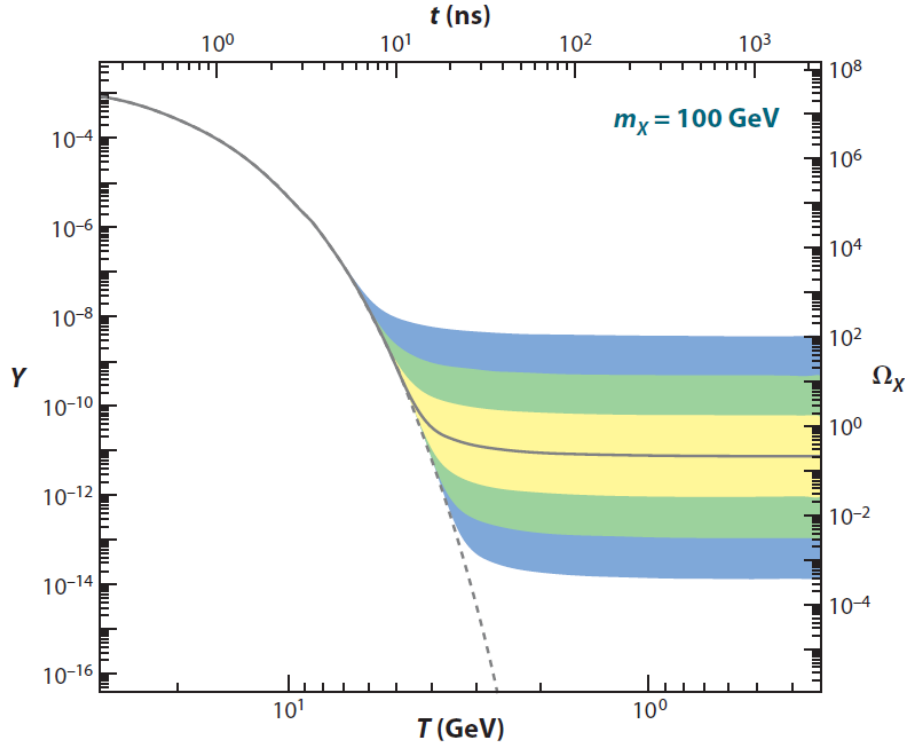
Figure 2.6: *The comoving number density Y (left) and resulting thermal relic density (right) of a 100 GeV dark matter particle as a function of temperature T (bottom) and time t (top). The solid gray contour is for an annihilation cross section that yields the correct relic density, and the shaded regions are for cross sections that differ by 10, 10^2, and 10^3 from this value. The dashed gray contour is the number density of a particle that remains in thermal equilibrium. Figure and caption taken from [Fen10].*

2.3 Detection of dark matter

The WIMP miracle provides a model-independent motivation for dark matter at the weak scale. To have the observed relic abundance the WIMPs must annihilate to other particles, such as standard model particles.

These assumptions suggest three promising strategies on how dark matter particles might potentially be detected:

1. Indirect detection: If WIMPs annihilate in the early universe into SM particles, they must also do it today. The annihilation products from processes near dark holes where a high density of dark matter is expected due to the high gravitational potential may be detectable.

2. Collider experiments: Dark matter particles may be produced in colliders by collisions of standard model particles. It is not possible to detect the DM particles directly, but they may be detected through missing mass in the collision products.

3. Direct detection: Dark matter may be detected via scattering with standard model particles, depositing energy in sensitive, low background detectors.

This thesis is contributing to the XENON Dark Matter Project and therefore the method of direct detection will be the only one presented in the next section.

2.3.1 Direct detection

Dark matter may be observed directly via scattering of normal matter in a large detector, depositing energy in form of recoil energy. The event rate per detector mass and recoil energy for this process can be derived from the cross section for WIMP nucleus scattering, considering the density of the dark matter halo ρ_χ and its velocity distribution.

$$\frac{dR}{dE} = \frac{\rho_\chi \sigma F^2(q)}{2m\mu^2} \int\limits_{v>\sqrt{ME/2\mu^2}} \frac{f(v,t)}{v} \mathrm{d}^3 v \tag{2.5}$$

$f(v,t)$ is the WIMP velocity distribution, μ is the reduced mass of the WIMP/nucleus system and $F(q)$ is the nuclear form factor. The WIMP can either have a spin coupling to a target nucleus (spin dependent), or it can couple coherently to the nucleus (spin independent). Therefore, the cross section σ can be expressed as the following:

$$\sigma_{SI} = \frac{A^2 \mu^2}{\mu_p^2} \sigma_p \qquad\qquad\qquad \text{Spin-independent} \tag{2.6}$$

$$\sigma_{SD} = \frac{4\mu^2}{\pi} |\langle S_p \rangle G_p + \langle S_n \rangle G_n|^2 \qquad\qquad \text{Spin-dependent} \tag{2.7}$$

One can see that the spin-independent cross section scales as atomic number squared (A^2), while the spin-dependent cross section depends on the spin content of the nucleon. Formula 2.5, 2.6 and 2.7 are taken from [Fre06].
The induced recoil energy by the WIMP scattering can be measured in three different ways:

1. Heat: The scattering creates phonons within the target material. Changes in temperature in the range of mK can be measured.

2. Charge: The target material gets ionised by scattering, producing electrons that can be measured as charge.

3. Light: The scattering process produces scintillation light that can be measured by photo sensitive detectors.

Most commonly, actual experiments for direct dark matter detection use two of the possible three ways of detection to be able to discriminate WIMP signals from background signals (see 3.4). Several experiments related to their detection method are shown in figure 2.7.
The XENON Dark Matter Project uses xenon as detector material and wants to detect WIMPs via charge and light signals. This project will be presented in the following chapter.
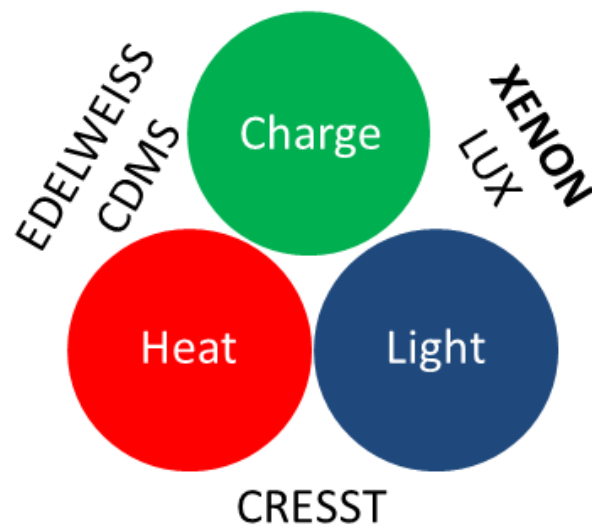
Figure 2.7: *The recoil energy introduced by a WIMP-nucleon scatter process can be measured via heat, charge or light. Most common, two detection principles are used to be able to discriminate background events from real WIMP events. Actual experiments, related to the used detection principles, are shown.*

3 The XENON Dark Matter Project

The XENON Dark Matter Project started in 2005 and aims for the direct detection of WIMPs by measuring light and charge signals produced in a liquid xenon detector.

The first experiment, namely the XENON10 experiment, was made of 15 kg xenon filled into a dual phase time projection chamber (TPC) used as detector, which is described in more detail in section 3.2. The project is located at the Laboratori Nazionali del Gran Sasso (LNGS) in Italy, an underground laboratory at a depth of 3600 m water equivalent to reduce the background produced by cosmic radiation. In the beginning of 2008, limits on the spin independent WIMP-nucleon scattering cross section were claimed as

$$\sigma_{SI} < 4.5 \cdot 10^{-44} \text{cm}^2 \qquad \text{and} \qquad \sigma_{SI} < 8.8 \cdot 10^{-44} \text{cm}^2 \tag{3.1}$$

for WIMPs with a mass of $30 \text{ GeV}/\text{c}^2$ and $100 \text{ GeV}/\text{c}^2$, respectively [Ang08], providing the most sensitive limit at that time. During 2008, the next generation experiment XENON100 started its operation and the analysis of 224.6 live days $\times$ 34 kg exposure has yielded no evidence for dark matter. The experiment set the most stringent limit on the spin-independent elastic WIMP-nucleon scattering cross section for WIMP masses above $8 \text{ GeV}/\text{c}^2$, with a minimum of

$$\sigma_{SI} < 2.0 \cdot 10^{-45} \text{cm}^2 \tag{3.2}$$

for a WIMP mass of $55 \text{ GeV}/\text{c}^2$ and 90 % confidence level in 2012 [Apr12b]. Just recently it was surpassed by the Large Underground Xenon dark matter experiment (LUX), that is of the same principle to the XENON detector. The analysis of their first WIMP search data set containing 85.3 live-days of data with a fiducial volume of 118 kg xenon yielded a spin-independent WIMP-nucleon elastic scattering cross section with a minimum upper limit of

$$\sigma_{SI} < 7.6 \cdot 10^{-46} \text{cm}^2 \tag{3.3}$$

for a WIMP mass of $33 \text{ GeV}/\text{c}^2$ and 90 % confidence level [LUX13b].

However, the next generation experiment XENON1T, designed for one ton of fiducial xenon, is already under construction and is aiming for more than one order of magnitude better sensitivity to the spin-independent cross section:

$$\sigma_{SI} = 2 \cdot 10^{-47} \text{cm}^2 \tag{3.4}$$

for a WIMP mass of $50 \text{ GeV}/\text{c}^2$. [Apr10]

The results of the XENON Dark Matter Project and of other experiments in the dark matter field are shown in an exclusion plot in figure 3.1. On this plot the WIMP-nucleon cross section is plotted against the possible WIMP mass. All WIMP candidates with a mass and cross section lying above the exclusion line are excluded to be dark matter. The regions given by the results of DAMA and CoGeNT, who already claimed to have found dark matter, are excluded independently by XENON,
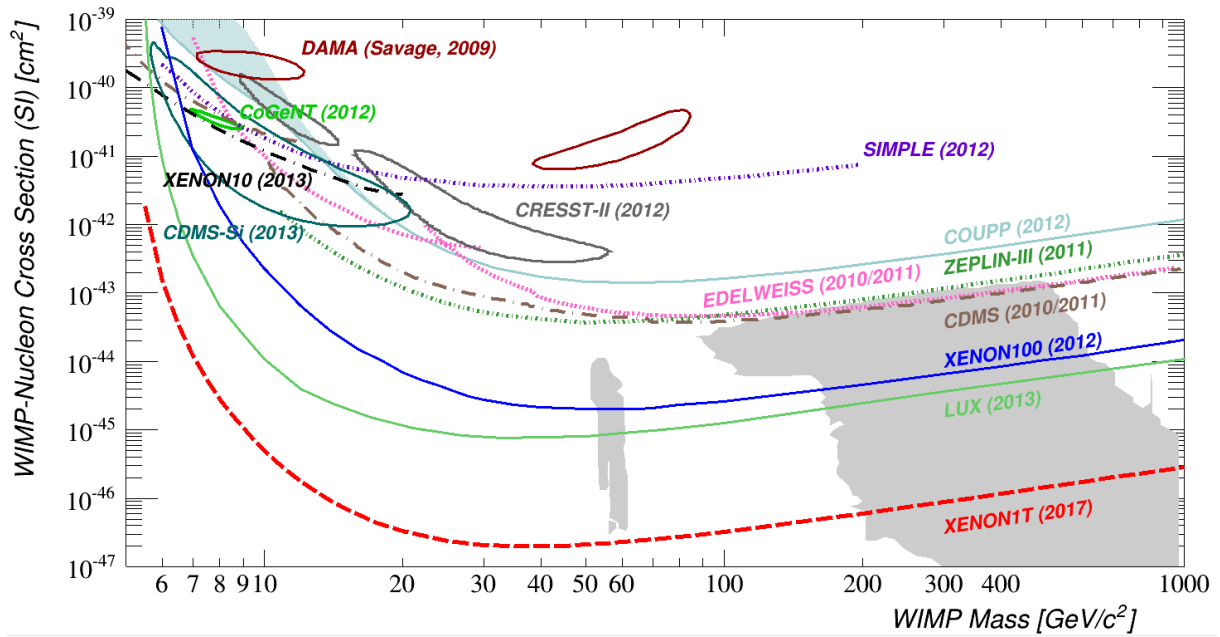
Figure 3.1: *The WIMP-nucleon cross section is plotted against the possible WIMP mass. Several exclusion plots of different experiments are shown. A WIMP with a certain mass and cross section lying above of such an exclusion plot is excluded to exist as dark matter. The most stringent level is set by LUX (light green). The region of the results by DAMA and CoGeNT that claimed to have found dark matter are excluded independently by XENON, LUX and CDMS. Likely dark matter candidates predicted by supersymmetry models are also ruled out (grey coloured region). Figure in courtesy of XENON collaboration.*

LUX and CDMS.

In the next section, the XENON Dark Matter Project will be described in more detail, beginning with xenon as a favourable detector material. After that, the working principle of a dual phase time projection chamber will be presented. In the end of this chapter the limitation of the detector sensitivity due to intrinsic and external background for a large scale detector as the XENON1T detector are explained.

3.1 Xenon as detector material for a dark matter experiment

Liquid xenon fulfills several requirements to be favourable dark matter detector material. The different aspects are presented in this section:

Heavy nucleus

Xenon has a heavy nucleus with A$\sim$131. The spin-independent cross section is proportional to A^2 as described in section 2.3.1. Therefore, xenon has a higher interaction rate than other detector materials,
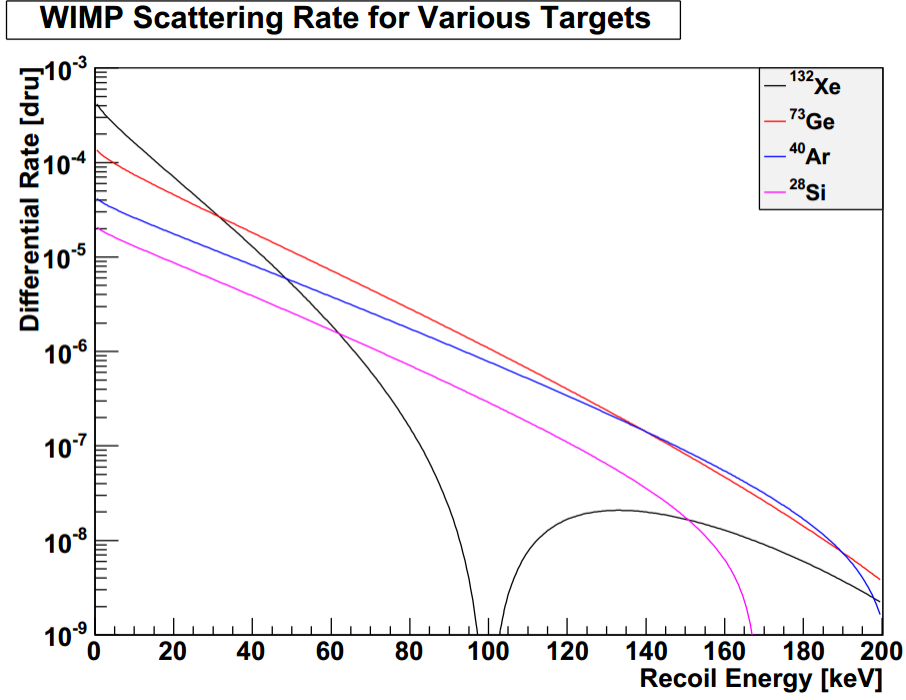
Figure 3.2: *Differential WIMP spin-independent scattering rate for several target materials with $m_\chi = 100 \, \text{GeV}/c^2$ and $\sigma = 10^{-44} \, \text{cm}^2$. For low recoil energies xenon has the highest interaction rate. Due to the form factor $F(q)$ the rate gets suppressed for higher recoil energies. Therefore xenon is favourable for low recoil energies with a WIMP mass around $100 \, \text{GeV}/c^2$ [Bro10].*

such as argon, germanium and silicon for low recoil energies as shown in figure 3.2. For higher recoil energies the scattering rate of WIMPs with xenon is suppressed due to the form factor $F(q)$ which is also mentioned in section 2.3.1. Detailed information on that are shown in [Bro10].

Even and odd isotopes

Table 3.1: *Xenon isotopes and their natural abundance. Table taken from [Apr09].*

^{124}Xe (0.09%)	^{126}Xe (0.09%)	^{128}Xe (1.92%)	^{129}Xe (26.44%)	^{130}Xe (4.08%)
^{131}Xe (21.18%)	^{132}Xe (26.89%)	^{134}Xe (10.44%)	^{136}Xe (8.87%)	

Natural xenon is composed of roughly half even and half odd isotopes as listed in table 3.1, which allows the detection of spin dependent interactions as discussed in section 2.3.1 and can be used to determine the character of the interaction by looking for both spin dependent and spin independent interactions.

Radioactivity

All naturally existing isotopes of xenon that are listed in table 3.1 are stable. The isotope ^{136}Xe is a candidate for double β-decay, but these rare interactions are the subject of other rare event searches and pose no significant background for dark matter experiments. However, the liquid xenon is intrinsically contaminated by the radioactive isotopes ^{85}Kr and ^{222}Rn, due to the production process of xenon and emanation from detector and system hardware, respectively. The produced background signals and their reduction will be explained in section 3.4.

Self-shielding

Xenon has a high self-shielding property due to its high charge number Z of 54. As a result of that the gamma stopping power is very high, so low energy gammas are not able to penetrate deeply into the target. With that, a background reduction by fiducialization accepting only events from the quiet central region of the detector is possible.
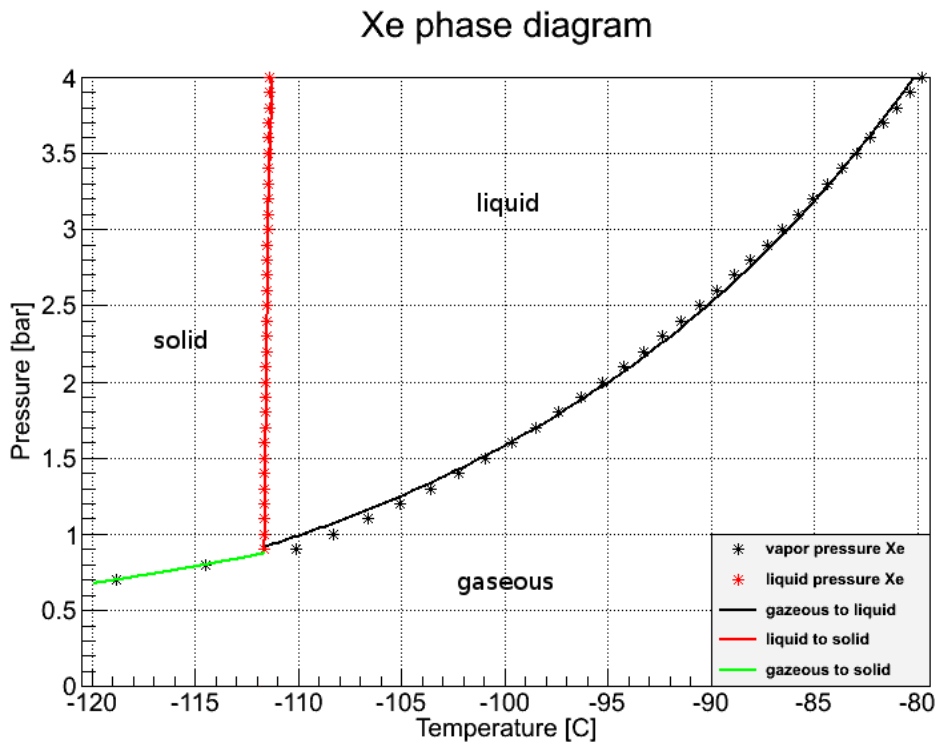
Handling

Figure 3.3: *Phase diagram of xenon. The region for gaseous, solid and liquid xenon are indicated. Drawing by F. Sprenger based on data from [NIST].*

The phase diagram of xenon is shown in figure 3.3. At atmospheric pressure the range for liquid

xenon is between 161.40 K and 164.82 K [NIST]. For lower temperatures, it begins to freeze out, for higher temperatures, it begins to evaporate. Increasing the pressure to 2 bar, the melting point stays almost the same, but the boiling point increases to about 177.88 K [NIST]. By further increasing of the pressure, the temperature range for liquid xenon would increase, but the stress on the detector hardware, especially on the PMTs, would also increase. Therefore, the operation at 2 bar is a good compromise for an acceptable liquid temperature range and low stress for the hardware. The design of the cryogenic system is easy and unproblematic, because standard cryocoolers are able to provide the necessary cooling power to cool down and liquefy the xenon even for large amounts up to a ton scale detector. These temperature and pressure requirements are much easier to handle than, for example, bolometer detectors from other dark matter experiments that are working at mK temperatures.
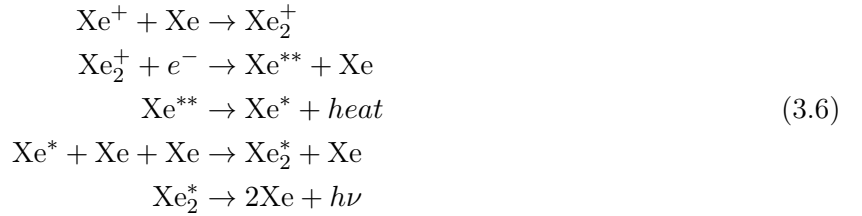
Scalability

Because of the high density of liquid xenon ($\sim 3\,\mathrm{g/cm^3}$) it is possible to design compact detectors. In addition, the easy handling at cryogenic temperatures makes it possible to build detectors with large dimensions and high target-masses that lead to higher scattering rates.

Light and charge

The scintillation light is emitted by an excited dimer ($\mathrm{Xe_2^*}$) decaying to the ground state, which is created by radiation in two different processes. The first one is shown in equation 3.5 and has an excited xenon atom ($\mathrm{Xe^*}$) as initial condition.

$$\mathrm{Xe^* + Xe \rightarrow Xe_2^*}$$
$$\mathrm{Xe_2^* \rightarrow 2Xe} + h\nu \tag{3.5}$$

The second one is made of several reactions starting with primary ionised xenon atoms ($\mathrm{Xe^+}$) and is shown in 3.6. During this process heat is also produced.

$$\mathrm{Xe^+ + Xe \rightarrow Xe_2^+}$$
$$\mathrm{Xe_2^+} + e^- \rightarrow \mathrm{Xe^{**} + Xe}$$
$$\mathrm{Xe^{**} \rightarrow Xe^*} + heat$$
$$\mathrm{Xe^* + Xe + Xe \rightarrow Xe_2^* + Xe}$$
$$\mathrm{Xe_2^* \rightarrow 2Xe} + h\nu \tag{3.6}$$

The reactions are referred to [Apr09].
Because the light is emitted by an excited dimer, the other xenon atoms do not absorb this light. In consequence, xenon is transparent for its own scintillation light. The emitted photons with a wavelength of about 178nm [Apr09] can propagate through the liquid and can be detected by UV sensitive photomultiplier tubes that are arranged around the detector.
The energy deposition, introduced by particle interaction with the target material, is split between ionisation and excitation. When an electric field is applied, some of the ionization component does not recombine as shown in equation 3.6, but can be collected independently from light as charge. The produced electrons are separated from the ions drifting along the field lines and can be measured as

described in section 3.2.

Combining charge and light, it is possible to discriminate between background signals, such as from gammas or electrons, and real WIMP events, because the ratio of energy deposited in scintillation and energy deposited in ionization depends on the kind of radiation (see section 3.4).

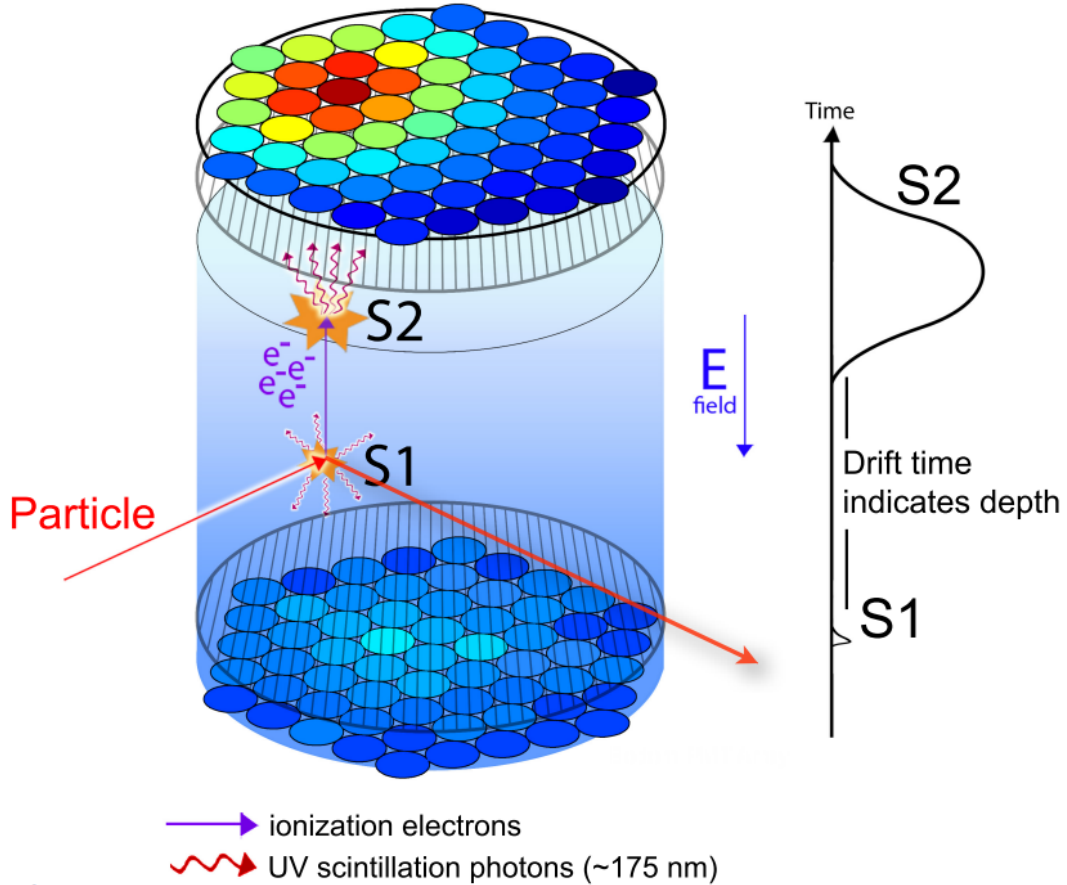## 3.2 A dual phase time projection chamber

Figure 3.4: *A scheme of the working principle of a dual phase xenon time projection chamber is shown. The prompt S1 signal due to a scintillation process and the delayed S2 signal due to ionisation and drifting electrons are shown. Because of the arranged arrays of PMTs a x- and y-position reconstruction is possible. Additionally, the depth of the interaction point is obtained by the drift-time of the electrons. With that, a full 3D position reconstruction of the recoil event and time is possible. Figure taken from [LUX13a]*

The cylindrical detector, made of polytetrafluoroethylene (PTFE), is used as a dual phase xenon time projection chamber. It is filled with liquid xenon to a certain level, with the top portion filled with gaseous xenon. The top and bottom are covered by arrays of PMTs. If an interaction of an

incoming particle with the target material occurs, light and charge are produced due to scintillation and ionisation processes as described in section 3.2. The light is promptly detected due to its speed of light propagation by the PMTs at the top and the bottom as S1 signal. The electron-ion pairs get separated due to an applied drift-field E_{field} and the electrons are guided upwards along the field lines to the edge of the liquid phase. Using a second electric field $E_{extract}$, the electrons are extracted from the liquid phase, accelerated into the gaseous phase, where they reach a sufficient energy to produce scintillation light. This signal can be detected also by the PMTs and is called S2.

The depth of the location of interaction, namely z-coordinate, can be obtained by the drift-time of the electrons, using the prompt S1 signal as start time and the delayed S2 signals as stop time. Due to the fact that the PMTs are arranged in an array, the x- and y-position of the interaction location can be determined depending on the hit pattern of the top PMT array. With that, a full 3D position reconstruction and the time of interaction can be obtained. The whole process is visualized in figure 3.4. In the following section the design parameters of the XENON100 detector will be briefly presented.

3.3 The XENON100 detector

The XENON100 TPC consists of 62 kg LXe as target material which is filled into the cylindrical PTFE reflector with 30.5 cm height and a diameter of 30.6 cm. The cylinder is mounted in a double-walled stainless steel cryostat and is covered by a 99 kg LXe active scintillator veto for background identification. The detector is passively shielded from inside to outside by a 5 cm layer of OFHC (oxygen-free high thermal conductivity) copper, followed by a 20 cm layer of polyethylene, 20 cm lead and 20 cm water. Additionally, the shield is purged with boil-off N_2 to suppress radon background [Apr12a].

In order to guide the electrons through the TPC, a drift-field of 530 V/cm is applied in the liquid phase and for the extraction and acceleration in the gas, an extraction-field of 12 kV/cm is applied to the gaseous xenon [Apr12b].

In total, 178 of 1″-square Hamamatsu R8520-AL PMTs with a low radioactivity and high quantum efficiency are used to detect the produced scintillation light. The S1 signal is mainly collected by the 80 PMTs at the bottom array due to total internal reflection of the UV light at the liquid surface. At the top the remaining 98 PMTs are arranged in concentric circles in order to improve the resolution of the radial event reconstruction. Furthermore, 64 PMTs that were originally used for the XENON10 detector are equipped to the active veto.

The depth z can be measured with a precision of 0.3 mm, and the uncertainty of the x- and y- position determination is lower than 3 mm in each direction [Apr12b].

3.4 Background discrimination and reduction

In order to improve the sensitivity of the detector, the discrimination and reduction of the background is an important key factor for a successful dark matter experiment. Especially for ton scale experiments, the sensitivity of the detector is limited by the level of background that can be achieved. The principles of background discrimination and reduction are presented in the following.
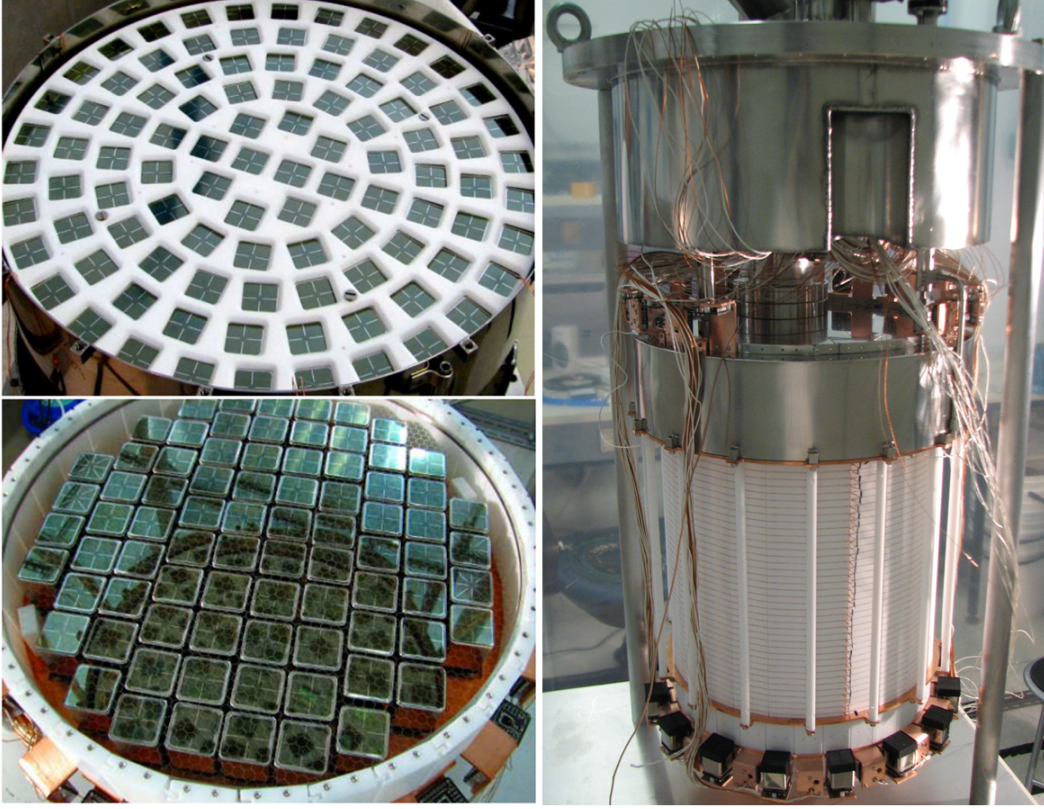
Figure 3.5: *On the left: (Top) The Hamamatsu R8520-06-Al PMTs on top of XENON100 are arranged in concentric circles in order to improve the reconstruction of the radial event position. (Bottom) On the bottom, the PMTs are arranged as closely as possible in order to achieve high light collection, as required for a low detector threshold. Caption and pictures taken from [Apr12a]. On the right: The assembled XENON100 detector consisting of the white PTFE reflector structure is shown. Picture in courtesy of XENON collaboration.*

3.4.1 Background discrimination

Because of the high self-shielding of LXe, radiation from outside is not able to penetrate deeply into the xenon. In a first step, a fiducial volume in the center of the target mass can be defined via calibration measurements. Signals outside this active area can be rejected as background, for example from the surface of the detector material. In a next step, interactions inside the fiducial mass can be analysed in more detail. Since WIMPs will only scatter once in the detector due to the extremely small cross section, double scatters from gammas or neutrons can be removed by multiple scatter identification. Scatters from neutrons or gammas belong to two different classes of recoil interactions. For a nuclear recoil, produced due to WIMP or neutron scattering, the ratio between the S2 and S1 signal is different than for an electronic recoil initiated by gamma or beta scattering as the following:

$$\left(S2/S1\right)_{\mathrm{NR}} \;<<\; \left(S2/S1\right)_{ER} \tag{3.7}$$

Hence, a discrimination between nuclear and electronic recoil is possible. Furthermore, the deposited energy for nuclear recoils can be used as another criterion. A signal can be rejected, if the corresponding energy deposition is too high in comparison with the expected energy deposition by WIMP scattering. Signals that are too low, cannot be distinguished from electronic noise and have to be rejected as well.
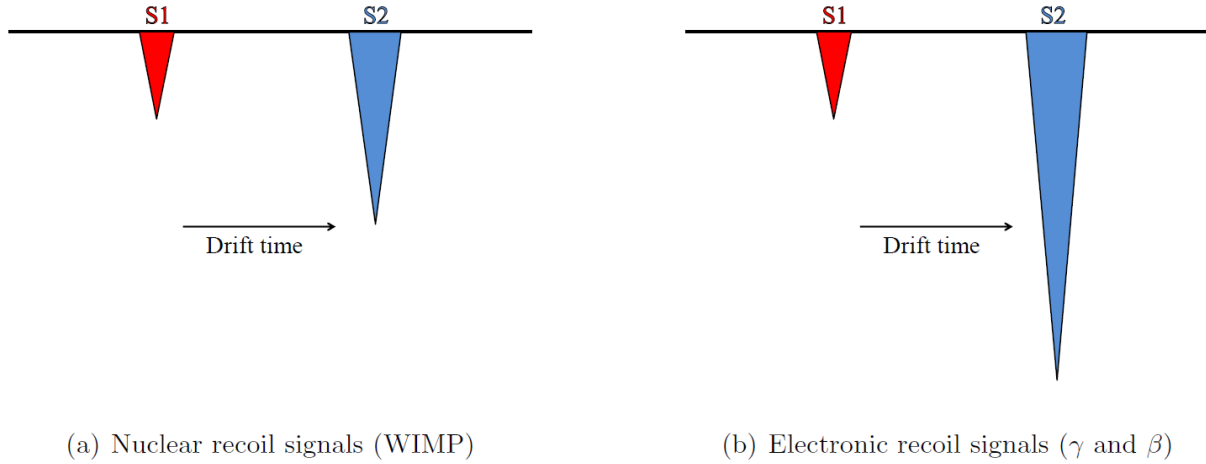

(a) Nuclear recoil signals (WIMP)   (b) Electronic recoil signals (γ and β)

Figure 3.6: *A schematic drawing of the waveforms of the light (S1) and charge (S2) signals for two types of events. A discrimination between nuclear recoils (a) and electronic recoils (b) is allowed due to the different ratio of the S2 and S1 signal [Apr12a].*

3.4.2 Background reduction

External background is introduced either by gamma interaction or neutron scattering. Alpha and beta radiation are not able to penetrate deeply into the detector and can be rejected easily by the active veto. If they are produced by an internal source, the energy deposition for alphas in the fiducial volume is at such a vast height, that these signals are of no concern to the dark matter search region.

As already mentioned, the XENON Dark Matter Project is set up in a deep underground laboratory in order to reduce the cosmic ray background. In the Laboratori Nazionali del Gran Sasso (LNGS) in Italy, which has an average depth of 3600 meter water equivalent (mwe), the muon flux is reduced by a factor of 10^6 [Amb95].

The remaining external background is made up of neutrons, produced in alpha-n reactions after an alpha decay, and of gammas generated by radioactive decays within the detector material and the experimental environment. These backgrounds are reduced by a passive shielding as already explained in section 3.3. The shield is purged with boil-off nitrogen in order to reduce radon background, especially the radioactive ^{222}Rn, which is produced in the decay chain of ^{238}U. Internal background, due to the detector hardware and material, is minimized by choosing only ultra clean material. Therefore, the selected hardware has been screened for its radiopurity beforehand. By the obtained activity of the detector material monte carlo simulations about the background are possible.

The final background level is determined by the leakage events from the described reduction techniques

and by intrinsic contaminations of the xenon itself. Electronegative impurities in the LXe, capturing free electrons and absorbing the scintillation light, reduce the drift-length of the electrons and the light yield used for the S2 and S1 signal, respectively. In consequence, the performance of the TPC is deteriorated. Therefore, the xenon is continuously recirculating through a hot getter outside the detector in order to reduce these impurities down to a required level of 1 ppb (oxygen equivalent) as shown in [Apr09]. Nevertheless, xenon is contaminated by noble gases that are unaffected by this process. One isotope of krypton, namely ^{85}Kr, is causing electronic recoil background inside the fiducial volume due to its β-decay, which has a half-life of 10.76 years with an endpoint energy of 687keV as shown in the decay scheme in 3.7.

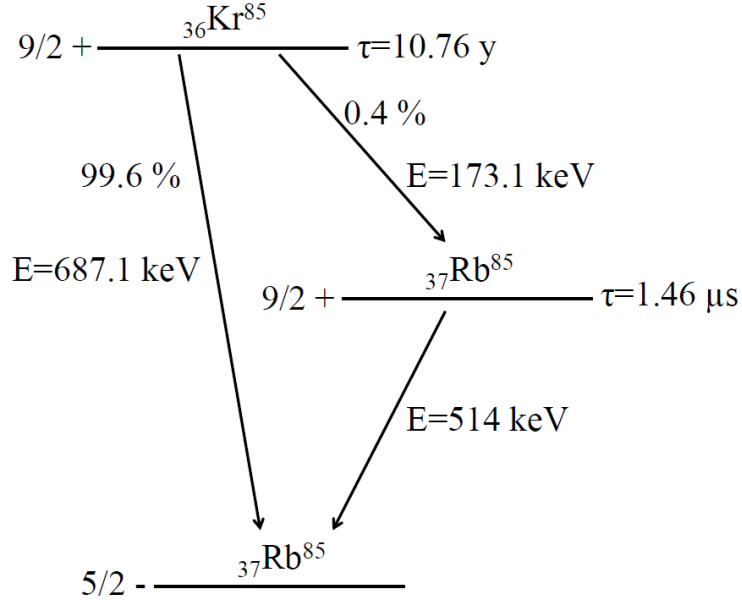Because, it is an intrinsic contamination, the background can not be reduced by fiducial volume cuts.

Figure 3.7: *Decay scheme of* ^{85}Kr *[Apr12a].*

Due to its long half-life, it is simply not possible to just wait until the krypton is decayed, but it has to be removed beforehand. This can be done by a cryogenic distillation column because of the different boiling points of krypton and xenon as described in chapter 4. The abundance of ^{85}Kr in natural krypton is

$$\frac{^{85}\text{Kr}}{^{nat}\text{Kr}} \sim 10^{-11} \qquad \text{[Che99].} \tag{3.8}$$

The isotope is produced in uranium and plutonium fission and is released to the environment by nuclear weapon tests and nuclear reprocessing plants. Commercial xenon normally has an abundance of natural krypton on the ppm[1] level. However, it is possible to buy pure xenon with a ^{nat}Kr/Xe ratio $\sim$10 ppb[2], but the required level for XENON100 is below 100 ppt[3] [Apr12a]. The distillation

---

[1] 1 ppm (parts per million) $= 10^{-6}$
[2] 1 ppb (parts per billion) $= 10^{-9}$
[3] 1 ppt (parts per trillion) $= 10^{-12}$

column for XENON100 has a total height of $3\,\mathrm{m}$ and was designed for a reduction factor of 1000. With a throughput of $0.6\,\mathrm{kg/h}$, a concentration of $(19 \pm 40)\,\mathrm{ppt}$ natural krypton in xenon was achieved [Apr12b].

3.5 The XENON1T experiment

The XENON100 experiment has reached its designed sensitivity with an upper limit for spin-independent WIMP-nucleon scattering cross section of

$$\sigma_{SI} < 2 \cdot 10^{-45} \mathrm{cm}^2 \tag{3.9}$$

with a WIMP mass of $55\,\mathrm{GeV/c^2}$ and $90\,\%$ confidence level [Apr12b]. In order to increase the sensitivity and push forward into new regions of the dark matter field, the next generation experiment XENON1T was designed, which is currently under construction. The new detector contains $2.4\,\mathrm{tons}$ of target mass of which $1\,\mathrm{ton}$ will be used as fiducial mass inside a TPC with a height and diameter of $1\,\mathrm{m}$ each. In total more than $3\,\mathrm{tons}$ of xenon are used in the whole experiment, including the detector and purification systems. The cryostat will be mounted in a water tank with a diameter and height of $10\,\mathrm{m}$, which will be used as passive shielding and as an active muon veto. The new detector aims for the discovery of WIMPs with an expected sensitivity of more than one order of magnitude better than current experiments. The sensitivity to the spin-independent WIMP-nucleon scattering cross section is expected to be

$$\sigma_{SI} = 2 \cdot 10^{-47} \mathrm{cm}^2 \tag{3.10}$$

for a WIMP mass of $50\,\mathrm{GeV/c^2}$ [Apr10].

The limitation of the sensitivity is given by the background level in the detector as mentioned before in section 3.4. For such high amounts of xenon, the intrinsic contamination becomes the most critical component for the final background level. Therefore, only one background event by the radioactive $^{85}\mathrm{Kr}$ in a volume of one ton of xenon is allowed during one year of exposure, which corresponds to a concentration of $^{nat}\mathrm{Kr}$ in xenon in the sub-ppt region. This relation can be derived by the following: In a first step, the number of $^{85}\mathrm{Kr}$ particles in $1\,\mathrm{ton}$ of xenon, which corresponds to a molar mass of $7633.6\,\mathrm{mol}$, can be estimated, using the fraction of $^{85}\mathrm{Kr}$ in $^{nat}\mathrm{Kr}$, which has been determined to be $2.1 \times 10^{-11}\,\mathrm{mol/mol}$ in the underground laboratory at Gran Sasso [Sel12]. For an assumed concentration of natural krypton in xenon of $1\,\mathrm{ppt}$ follows:

$$N_{85\mathrm{Kr}} = 7633.6\,\mathrm{mol} \cdot 10^{-12} \cdot 2.1 \cdot 10^{-11} \cdot 6.022 \cdot 10^{23} \,\frac{1}{\mathrm{mol}} = 9.7 \cdot 10^4 \tag{3.11}$$

In a next step, the activity A of the radioactive krypton is calculated with the number of particles, obtained above, and the decay constant λ, which can be derived from the half life of $10.75\,\mathrm{y}$:

$$A_{85\mathrm{Kr}} = N_{85\mathrm{Kr}} \cdot \lambda_{85\mathrm{Kr}} = N_{85\mathrm{Kr}} \cdot \frac{\ln(2)}{t_{1/2}} = 9.7 \cdot 10^4 \cdot \frac{\ln(2)}{10.75\,\mathrm{y}} = 6227.5 \,\frac{\mathrm{evt}}{\mathrm{y\,ton}} \tag{3.12}$$

According to [Sel12], most of the $^{85}\mathrm{Kr}$ decays ($>99\,\%$) produce single scatter events inside the detector, but only a fraction of $3\,\%$ lays within the crucial energy region of $[2,15]\mathrm{keV}$. This value has been derived from the integration of the beta-spectrum of $^{85}\mathrm{Kr}$ over the mentioned energy interval.

In a last step, the S2/S1 discrimination can be used in order to exclude $99.5\,\%$ of the remaining background signals. The $0.5\,\%$ left lead to a background event rate, assuming a concentration of $1\,\mathrm{ppt}$ natural krypton in xenon, of:

$$A_{85\mathrm{Kr}} = 6227.5 \cdot 0.03 \cdot 0.005 = 0.93 \ \frac{\mathrm{evt}}{\mathrm{y\ ton\ keV}} \tag{3.13}$$

On the basis of these calculations, a diagram showing the event background rate in terms of time, mass and energy dependent upon the concentration of natural krypton in xenon is presented in figure 3.8.
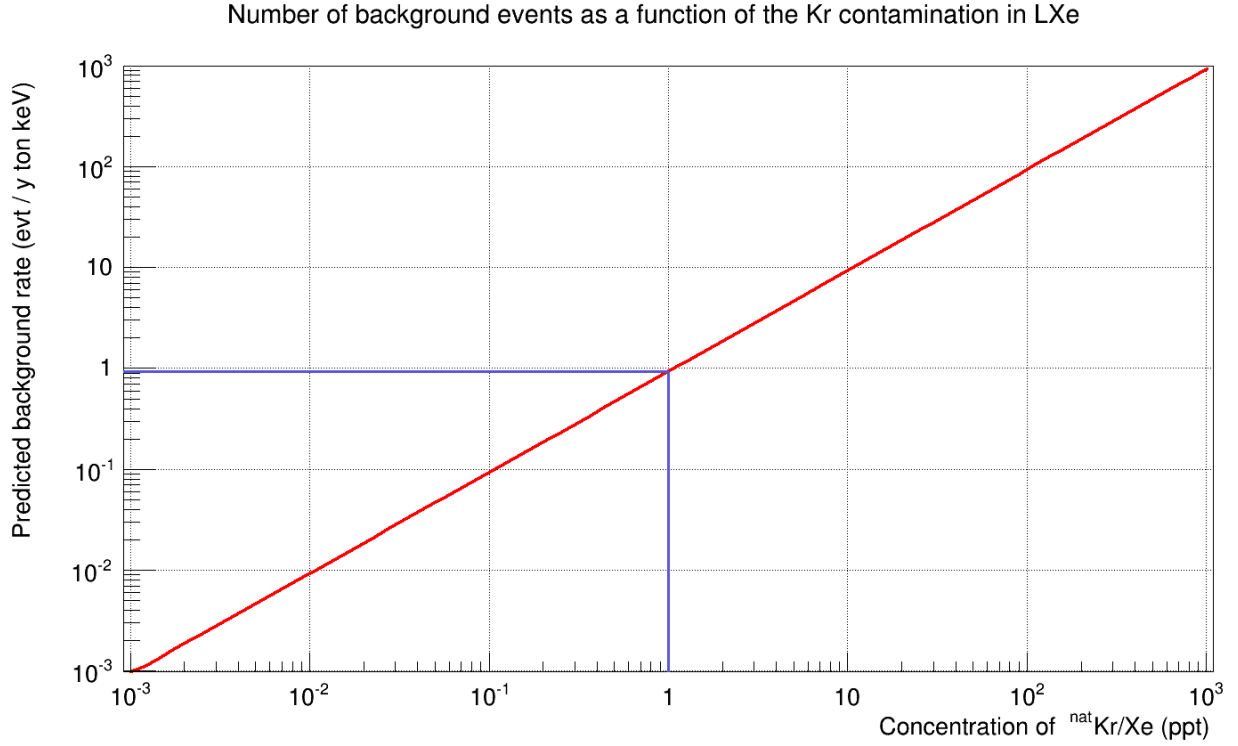

Figure 3.8: *The dependence of the background event in terms of time, mass and energy from the ratio of natural krypton in xenon is shown (red). Assuming a concentration of 1 ppt, a number of about one background event per year, ton and keV is expected (blue).*

In order to achieve a krypton in xenon ratio on the sub-ppt level, a new distillation column was designed and is currently under development in Muenster. The required design parameters will be presented in the following section.

3.5.1 Design parameters for the cryogenic distillation column

The existing cryogenic distillation column for the XENON100 project, with a throughput of $0.6\,\mathrm{kg/h}$, would need about 30 weeks of continuous distillation to clean 3 tons of xenon once. Furthermore, the achieved ratio of natural krypton in xenon with $(19 \pm 4)\,\mathrm{ppt}$ [Apr12b] is far too high for the XENON1T experiment.

Because of that, a new column with higher separation efficiency has to be designed and developed. In order to reduce the distillation time, the new column should have a throughput of $3\,\mathrm{kg/h}$, which would allow to clean the xenon once by 6 weeks of continuous distillation.

During the operation, $99\,\%$ of the distilled xenon should be recovered and used as detector material, while only $1\,\%$ is stored as krypton enriched off-gas.

Assuming the commercial xenon to have a concentration on the ppb-level of natural krypton inside as stated by the suppliers, a separation factor of 10^4-10^5 is needed to obtain a sub-ppt level.

The principle, design and set up of the cryogenic distillation column of the Muenster group will be presented in the next chapter.

4 Principle and design of a cryogenic distillation column

The XENON1T Dark Matter Project will use a liquid xenon detector as described in the previous section. For a very low background, ultra clean xenon is needed. One drawback of xenon is the radioactive contamination by the isotope ^{85}Kr ($t_{1/2}$=10.76 years, β-decay with Q_β=687.1 keV), which has a huge impact on the background. Therefore, the natural krypton concentration has to be reduced down to a sub-ppt concentration. The removal can be done by a cryogenic distillation column due to the different boiling points of xenon and krypton. Therefore, a cryogenic distillation column was designed, assembled and tested by the collaboration group in Muenster.

In this chapter the principle of cryogenic distillation is shown and the determination of the height of the column by the McCabe-Thiele method is explained. Unless stated otherwise, the following equations and explanations concerning the principle of cryogenic distillation and the McCabe-Thiele method can be found in [McC05] and [Loh07].

4.1 Principle of cryogenic distillation

The idea of cryogenic distillation is to take advantage of the difference in vapour pressure of the two components of the binary mixture, in this case: Krypton and xenon. In a closed system with constant temperature and pressure, the vapour pressure describes the probability that an atom migrates from liquid into gas phase until the equilibrium between the two phases is reached. Figure 4.1 shows that krypton is the high volatile component and xenon the low volatile component. Taking this into account, one can choose the operating conditions for temperature and pressure near to the boiling point of xenon. Thus, krypton will very likely migrate to the gaseous phase while most of the xenon will remain in the liquid phase. After the equilibrium in this single distillation stage is reached, there is a higher concentration of krypton in the gaseous phase (y_{Kr}) and a lower concentration in the liquid phase (x_{Kr}). In order to increase the separation efficiency, a multi-stages distillation column with a partial reflux can be used, that contains several connected distillation stages, as shown in figure 4.2.

Setting the reboiler stage as the starting point, the binary mixture is evaporated. As a consequence of vapour pressure, the composition of the generated steam is different from the liquid. As described, the high volatile krypton is enriched in the steam, while the low volatile xenon remains in the liquid phase. Assuming that the full steam will condense on the next stage (1. Plate), the generated liquid phase on this stage will have the same composition as the steam from the reboiler stage, and will therefore have a higher concentration of krypton compared to the starting mixture. By repeating this procedure for several stages, the fraction of krypton in xenon will be increased successively. On top of the tower the vapour is partially liquefied and fed back to the column. A small fraction of the gas is taken out as
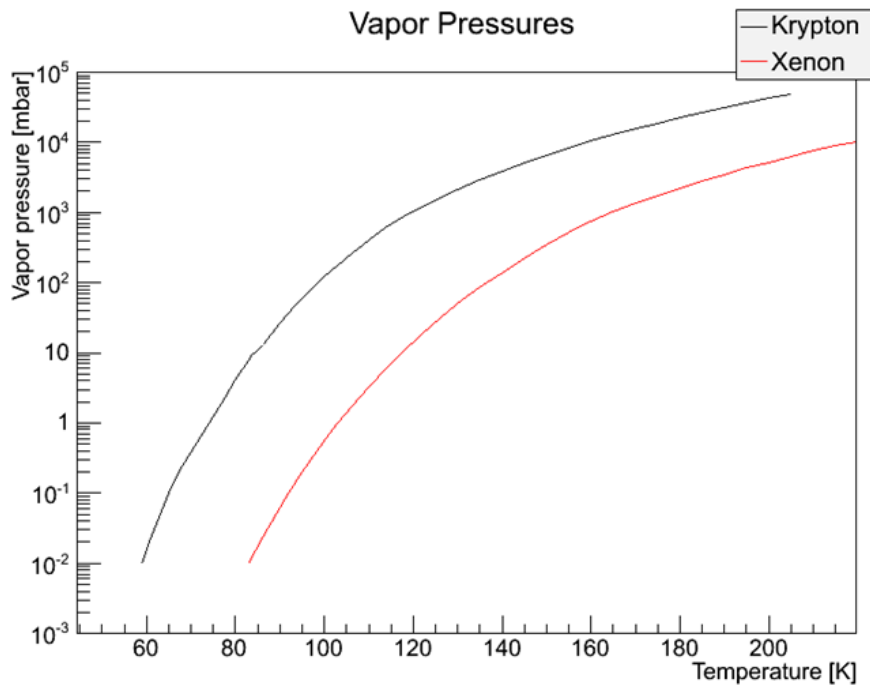
Figure 4.1: *Vapour pressures of krypton (black line) and xenon (red line) in terms of temperature. Because of the difference in vapour pressure, cryogenic distillation can be used to reduce the krypton concentration in xenon. Figure taken from [Bro13]*

krypton enriched off gas. The operation with a partial reflux is called rectification. Depending on the requested purity of the xenon at the bottom (purified xenon) and at the top (krypton enriched xenon) the number of theoretical stages can be calculated. Therefore, the different compositions for the gaseous and liquid phases of the different theoretical stages are plotted against each other in an equilibrium diagram based on the McCabe-Thiele method (Details in section 4.2), which is schematically shown in figure 4.2.

One way to realize the stages in the distillation column is to use a structured packing material which provides a large surface for a higher mass transfer and thus, a higher separation efficiency. Thereof, the required height for a defined separation factor of the column has to be calculated.

The McCabe-Thiele method and the calculation of the height of the column will be explained in the next sections.

4.2 The McCabe-Thiele method

The diagram in figure 4.2 is calculated by the McCabe-Thiele method, which is valid for distillation columns that operate with structured packing material and a partial reflux. This method leads to the number of theoretical stages that are needed to achieve a pre-defined separation factor.

In the diagram, the concentrations of krypton in the gaseous and in the liquid phase are plotted
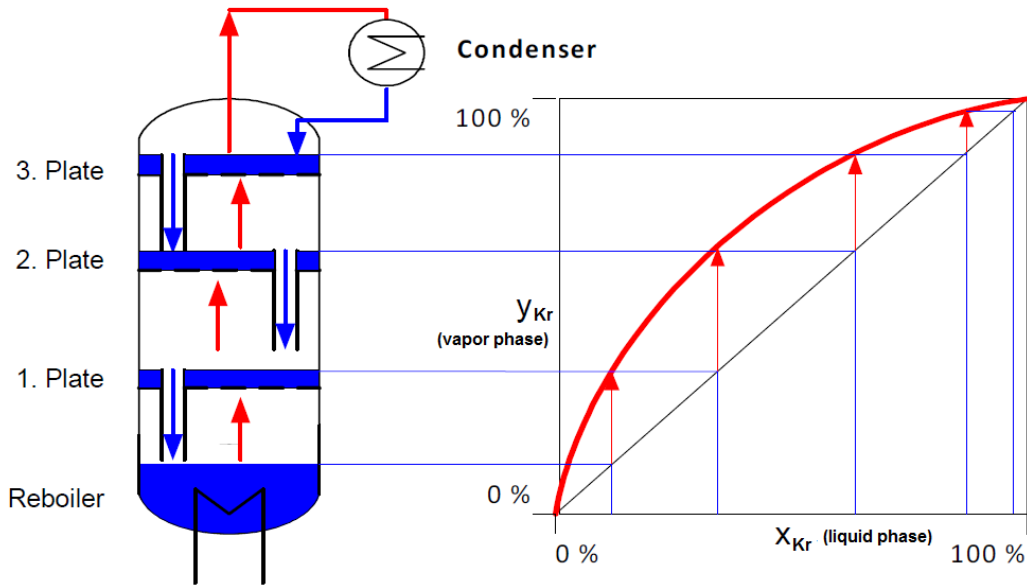
Figure 4.2: *On the left side a scheme of a multi-stages distillation column with partial reflux is shown. Its basic components consist of a reboiler, a condenser and several theoretical distillation stages. By evaporating the mixture from the bottom, the krypton concentration is increased step by step until it reaches the top of the column, based on the concept of vapour pressure. At the top the xenon is liquefied and filled back into the column while the krypton remains in the gaseous phase and is extracted as krypton enriched off-gas. The purified xenon can be extracted at the bottom. On the right side the concentrations of krypton in the gaseous and liquid phase are plotted against each other in a McCabe-Thiele diagram related to the different plates shown on the left. Scheme taken from C. Huhmann.*

against each other. An equilibrium line and an operating line can be observed. These two graphs will be explained in this section. After that, the construction of the diagram is shown.

4.2.1 Equilibrium line

For constant temperature and pressure the system drifts to equilibrium based on the concept of vapour pressure as described above. For each local concentration x_{Kr} of krypton in the liquid phase, there is a certain equilibrium concentration y_{Kr} in the vapour phase. Using Raoults law, one can calculate the partial pressures of the mixture given by:

$$p_{Xe} = P'_{Xe} \cdot x_{Xe} \qquad \rightarrow \qquad y_{Xe} := p_{Xe}/P \tag{4.1}$$

$$p_{Kr} = P'_{Kr} \cdot x_{Kr} \qquad \rightarrow \qquad y_{Kr} := p_{Kr}/P \tag{4.2}$$

with partial pressure p, vapour pressure P' and total pressure P. The relative volatility α is defined as

$$\alpha := \frac{y_{Kr}/x_{Kr}}{y_{Xe}/x_{Xe}} = \frac{P'_{Kr}/P}{P'_{Xe}/P} = \frac{P'_{Kr}}{P'_{Xe}} \tag{4.3}$$

and is a measurement for the separability of a binary mixture. For an operating temperature of 178 K the relative volatility is α=10.4 given by P'_{Kr}=2090 kPa and P'_{Xe}=201.4 kPa. This value is quite high and shows that in general the separation of krypton and xenon might be easy, but for such low concentrations of krypton the volatility becomes less important.

With $y_{Kr} = (1 - y_{Xe})$ and $x_{Kr} = (1 - x_{Xe})$ one can describe y_{Kr} as a function of x_{Kr}:

$$y_{Kr} = \frac{\alpha \cdot x_{Kr}}{1 + (\alpha - 1) \cdot x_{Kr}} \tag{4.4}$$

This relation is called equilibrium line and is shown in figure 4.3.

According to the low concentrations of krypton, one can estimate a separation factor for one theoretical stage to be in the order of 10 using equation 4.4 as the following:

$$\frac{y_{Kr}}{x_{Kr}} = \frac{\alpha}{1 + (\alpha - 1) \cdot x_{Kr}} \overset{x_{Kr} \ll 1}{=} \alpha \approx 10 \tag{4.5}$$

This has been investigated by pre-separation tests with the pre-cooler of the column, called preseparator, acting as one theoretical distillation stage and will be presented in [Ros14].
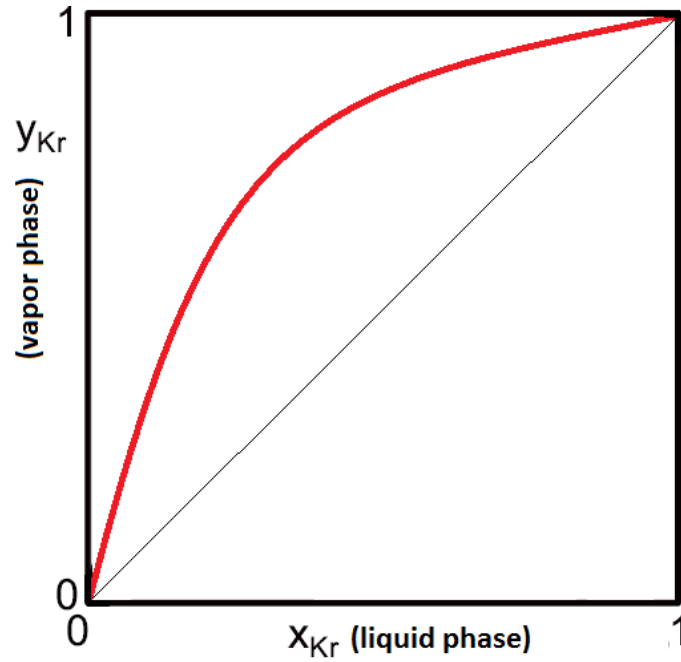

Figure 4.3: *A schematic equilibrium line of the McCabe-Thiele diagram is shown(red). The relation between the concentration of krypton in the liquid phase (x_{Kr}) and in the gaseous phase (y_{Kr}) is obtained by using Raoults law and the relative volatility.*

4.2.2 Operating lines

The column can be divided into the rectifying section, the feedpoint section and the stripping section. As the names state, in the top part, the rectifying section, an enhanced concentration of krypton in xenon is collected. At the bottom, the stripping section, a reduced krypton concentration is achieved. These two sections are separated by the feedpoint section, where the incoming raw xenon is fed to the column. By heating from the bottom and cooling from the top, the equilibrium inside the column is disturbed and particle flows upwards and downwards are introduced to the column.

As a result of that, the actual concentration of krypton in the gaseous phase related to the concentration in the liquid phase is now described by *operating lines* that are determined by the mass balance of each section. Between the equilibrium line and operating lines a forcing concentration gradient is ensued, driving the system toward the equilibrium via mass transfer between the ascended gaseous stream and the descended liquid stream.

In the following sections the calculation for the different mass balances are shown.

Total mass balance

Due to mass conservation, the incoming flow of xenon $\dot{F}$ has to be equal to the outgoing flow of xenon, which is the sum of the off-gas $\dot{D}$ and the liquid-out $\dot{B}$ as shown in figure 4.4:

$$\dot{F} = \dot{D} + \dot{B} \tag{4.6}$$

According to the different concentrations of krypton for each flow, the particle mass balance of the system can be calculated:

$$\dot{F} \cdot x_F = \dot{D} \cdot x_D + \dot{B} \cdot x_B \tag{4.7}$$

Using equation 4.6 and 4.7, the two outgoing flows can be written as:

$$\dot{D} = \frac{x_F - x_B}{x_D - x_B} \cdot \dot{F} \quad \text{and} \quad \dot{B} = \frac{x_D - x_F}{x_D - x_B} \cdot \dot{F} \tag{4.8}$$

Assuming to start with a concentration of x_F=100 ppb (10^{-7}) in the raw xenon gas and to reach a final concentration of x_B=1 ppt (10^{-12}) in the purified xenon, the krypton enriched off-gas should have a concentration of x_D=10 ppm (10^{-5}). With a pre-defined feeding flow-rate of $\dot{F}$=3 kg/h, equation 4.8 gives:

$$\dot{D} = 0.03 \, \text{kg/h} \quad \text{and} \quad \dot{B} = 2.97 \, \text{kg/h} \tag{4.9}$$

These values are also consistent with the requirement to lose only 1 % of the xenon during the process as krypton enriched off-gas.

The amount of xenon that is fed back either at the top as liquid or at the bottom as vapour is defined as the reflux ratio. There is one ratio for the rectifying section and one for the stripping section, defined as:

$$R = \frac{\dot{L}}{\dot{D}} \quad \text{and} \quad R' = \frac{\dot{L'}}{\dot{B}} \tag{4.10}$$

A higher reflux ratio increases the number of theoretical stages and improves the separation efficiency. In consequence, an almost total reflux is necessary. According to the results of a similar distillation
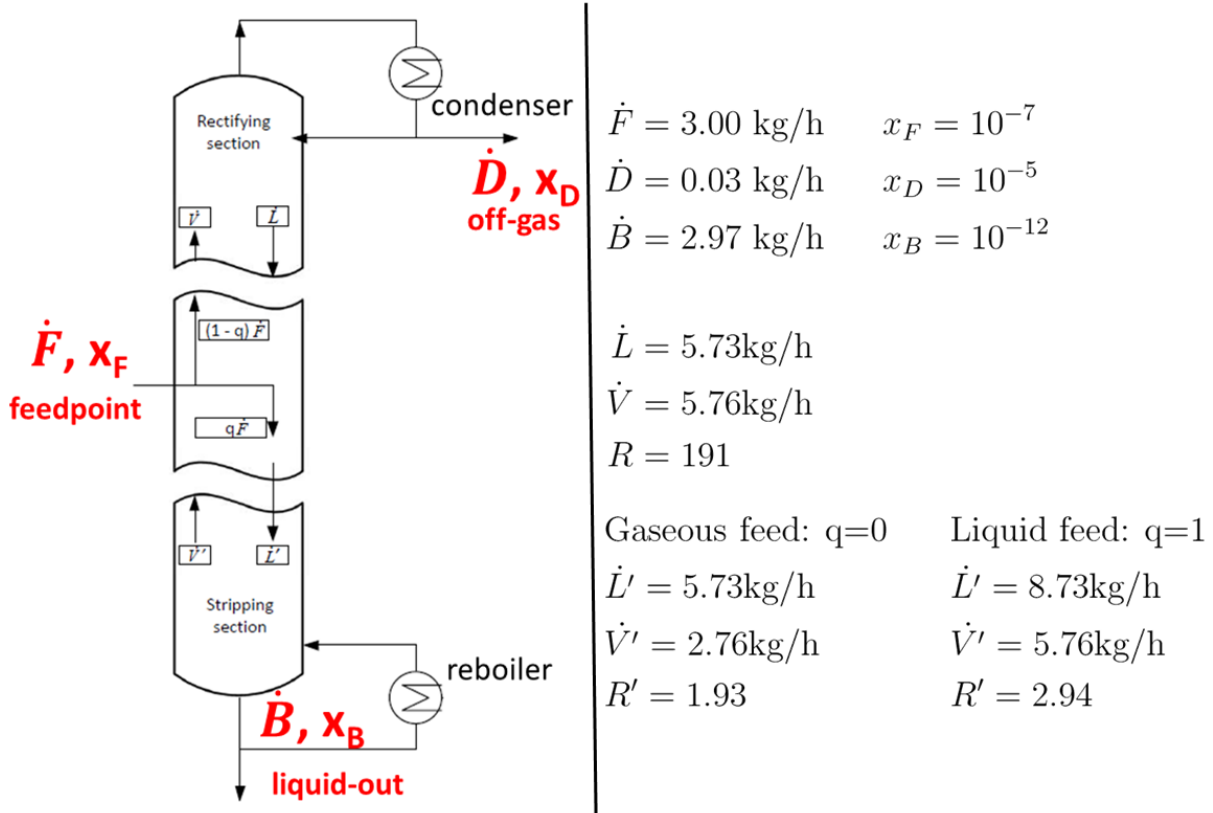
$\dot{F} = 3.00 \text{ kg/h} \qquad x_F = 10^{-7}$

$\dot{D} = 0.03 \text{ kg/h} \qquad x_D = 10^{-5}$

$\dot{B} = 2.97 \text{ kg/h} \qquad x_B = 10^{-12}$

$\dot{L} = 5.73 \text{kg/h}$

$\dot{V} = 5.76 \text{kg/h}$

$R = 191$

Gaseous feed: q=0	Liquid feed: q=1
$\dot{L}' = 5.73 \text{kg/h}$	$\dot{L}' = 8.73 \text{kg/h}$
$\dot{V}' = 2.76 \text{kg/h}$	$\dot{V}' = 5.76 \text{kg/h}$
$R' = 1.93$	$R' = 2.94$

Figure 4.4: *A scheme of several flows of the column are shown. $\dot{F}$, $\dot{D}$ and $\dot{B}$ are the flows of the input and output of the column, where x_F, x_D and x_B are the corresponding concentrations of krypton in xenon. $\dot{V}$ and $\dot{L}$ describe the flow of the rectifying section, $\dot{V}'$ and $\dot{L}'$ the ones for the stripping section. The factor q is a number between 0 and 1 and is in indication, if the feed is gaseous or liquid xenon. With the several flows and concentrations it is possible to calculate the particle flow in the column. The values for the several parameters are shown on the right. Figure based on [Loh07].*

column from the XMASS collaboration that reached a level of 3 ppt, the value for R was chosen to be 191 [Abe08]. In general, reflux ratios <10 will be found in industrially used distillation plants, otherwise the costs of energy and operation would be uneconomical. With given R=191 and equation 4.10, the flow $\dot{L}$ can be calculated:

$$\dot{L} = 191 \cdot 0.03 \text{ kg/h} = 5.73 \text{ kg/h} \tag{4.11}$$

Using $\dot{D}$ and $\dot{L}$, the flow-rate of the gaseous flow $\dot{V}$ can be obtained:

$$\dot{V} = \dot{D} + \dot{L} = 5.76 \text{ kg/h} \tag{4.12}$$

The parameters R', $\dot{L}'$ and $\dot{V}'$ depend on the phase composition of the fed xenon and will be calculated later on in the feedpoint section.

Mass balance of rectifying section

The upcoming gas flow $\dot{V}$ with an unknown concentration y has to be equal to the sum of the down-going liquid flow $\dot{L}$ with an unknown concentration x and the out-going off-gas flow $\dot{D}$ with a certain concentration x_D. As in the section above, one can calculate the particle mass balance for this part of the column:

$$\dot{V} \cdot y = \dot{L} \cdot x + \dot{D} \cdot x_D \tag{4.13}$$

Thereof, the relation between the concentration in the gaseous phase and liquid phase can be obtained:

$$y = \frac{\dot{L}}{\dot{L} + \dot{D}} \cdot x + \frac{\dot{D}}{\dot{L} + \dot{D}} \cdot x_D \tag{4.14}$$

With the definition of the reflux ratio R follows:

$$y = \frac{R}{R+1} \cdot x + \frac{x_D}{R+1} \tag{4.15}$$

This is the operating line for the rectifying section and it is called the *collection line*. It is shown on the right of figure 4.5.
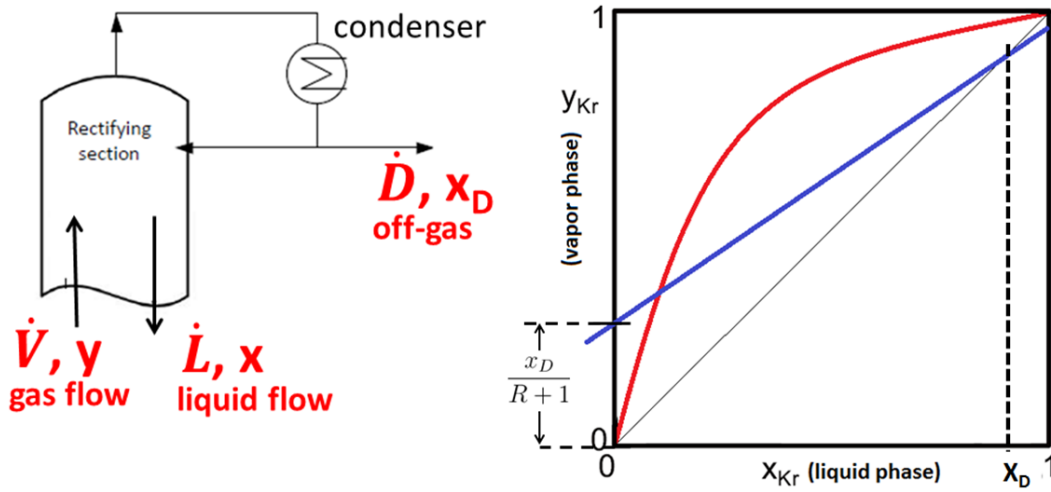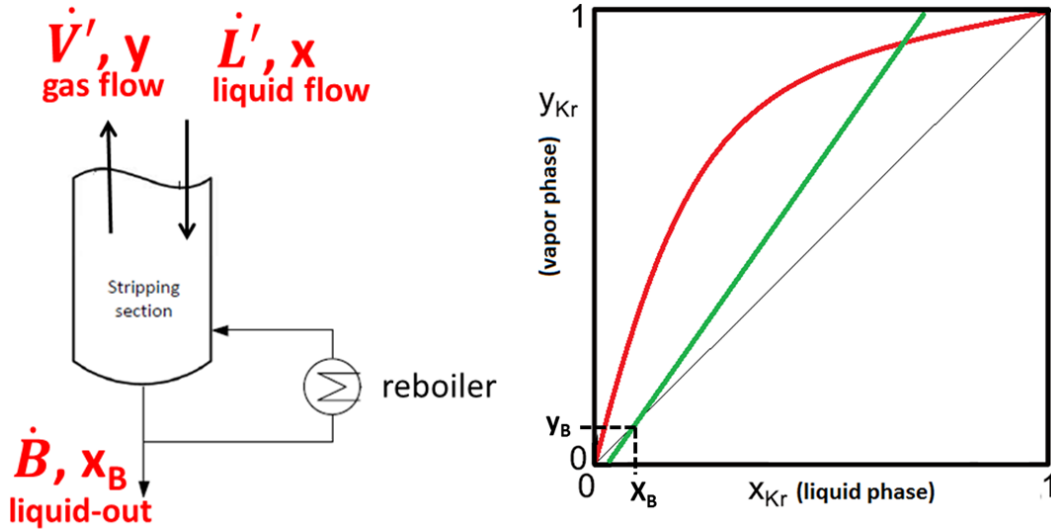

Figure 4.5: *A scheme of the rectifying section of the column is shown on the left. The upcoming gas flow $\dot{V}$, the down-going liquid flow $\dot{L}$ and the outgoing off-gas flow $\dot{D}$ are indicated together with the corresponding concentrations y, x and x_D. Using these values, it is possible to obtain the relation between the concentration of krypton in the gaseous and the liquid phase, which is called collecting line (blue) and is shown schematically on the right. The diagram also shows the equilibrium line (red). The y-axis value is given by $\frac{x_D}{R+1}$. For large R the slope of the collection line converges to 1.*

Mass balance of stripping section

Analogue to the rectifying section, the operating line for the stripping section can be obtained over particle mass balance. The involved flows are the down-coming liquid flow $\dot{L}'$, the up-going gas flow $\dot{V}'$ and the out-going liquid-out flow $\dot{B}$. It follows:

$$\dot{V}' = \dot{L}' - \dot{B} \tag{4.16}$$

The particle balance is given by:

$$\dot{L}' \cdot x = \dot{V}' \cdot y + \dot{B} \cdot x_B \tag{4.17}$$

The relation for the concentration between gaseous and liquid phase is:

$$y = \frac{\dot{L}'}{\dot{L}' - \dot{B}} \cdot x - \frac{\dot{B}}{\dot{L}' - \dot{B}} \cdot x_B \tag{4.18}$$

With the reflux ration $R' = \frac{\dot{L}'}{\dot{B}}$ for the stripping section follows:

$$y = \frac{R'}{R' - 1} \cdot x - \frac{x_B}{R' - 1} \tag{4.19}$$

This operating line is called *condensation line* and is shown in figure 4.6.

Figure 4.6: *A scheme of the stripping section of the column is shown on the left. The up-going gas flow $\dot{V}'$, the down-coming liquid flow $\dot{L}'$ and the out-going liquid-out flow $\dot{B}$ are indicated together with the corresponding concentrations y, x and x_B. Using these values, it is possible to obtain the relation between the concentration of krypton in the gaseous and the liquid phase, which is called condensation line (green) and is schematically shown on the right. The diagram also shows the equilibrium line (red).*
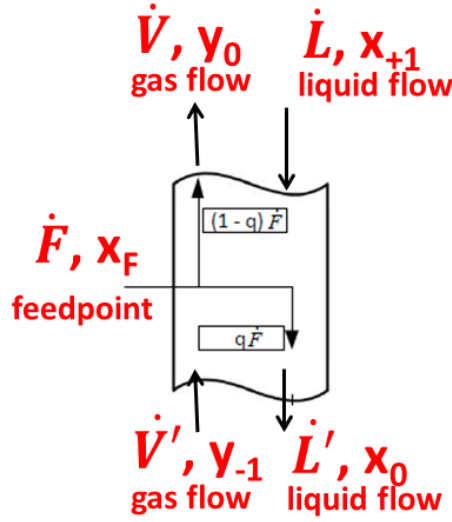
Mass balance of feedpoint section

Figure 4.7: *A scheme of the feedpoint section of the column is shown. There are three incoming flows to this section, namely the feed flow $\dot{F}$, the gas flow $\dot{V}'$ and the liquid flow $\dot{L}$. The gas flow $\dot{V}$ and the liquid flow $\dot{L}'$ are the outgoing flows. Every flow is indicated with its corresponding concentration of krypton in xenon. Using the caloric factor q and the krypton particle mass balance for this section, one obtains the intersection line, where the collection and condensation line crosses.*

Five flows in total are present in this section of the column. Specifically, the three incoming flows are the feed flow $\dot{F}$, the gas flow $\dot{V}'$ and the liquid flow $\dot{L}$, while the gas flow $\dot{V}$ and the liquid flow $\dot{L}'$ are the outgoing ones. The incoming xenon can be fed either in gaseous, in liquid or in a mixture of both phases. Therefore, a caloric factor q is defined, which describes the ratio of the amount of liquid to the amount of gas in the feed flow:

$$q = \frac{\dot{L}' - \dot{L}}{\dot{F}} \tag{4.20}$$

Analogously follows:

$$(1 - q) = \frac{\dot{V} - \dot{V}'}{\dot{F}} \tag{4.21}$$

Because of this definition, q can have a value between 0 and 1. The special cases for a gaseous and liquid feed are presented in the following.

Gaseous feed: q=0

If the xenon is fed to the column in gaseous phase, it is fully added to the vapour stream $\dot{V}'$, going directly up. Consequently, nothing is added to the liquid stream $\dot{L}'$. It follows:

$$\dot{L}' = \dot{L} + q \cdot \dot{F} = 5.73\,\text{kg/h} + 0 \cdot 3\,\text{kg/h} = 5.73\,\text{kg/h} \tag{4.22}$$

$$\dot{V}' = \dot{L}' - \dot{B} = 5.73\,\text{kg/h} - 2.97\,\text{kg/h} = 2.76\,\text{kg/h} \tag{4.23}$$

$$R' = \frac{\dot{L}'}{\dot{B}} = 1.93 \tag{4.24}$$

Liquid feed: q=1

If the xenon is fed to the column in liquid phase, it is fully added to the liquid stream $\dot{L}'$, going directly down. Consequently, nothing is added to the vapour stream $\dot{V}'$. It follows:

$$\dot{L}' = \dot{L} + q \cdot \dot{F} = 5.73\,\text{kg/h} + 1 \cdot 3\,\text{kg/h} = 8.73\,\text{kg/h} \tag{4.25}$$

$$\dot{V}' = \dot{L}' - \dot{B} = 8.73\,\text{kg/h} - 2.97\,\text{kg/h} = 5.76\,\text{kg/h} \tag{4.26}$$

$$R' = \frac{\dot{L}'}{\dot{B}} = 2.94 \tag{4.27}$$

A mixture between gas and liquid would lead to a splitting of the two phases and consequently, the calculated parameters would be inside the range of the two special cases.
To obtain the operating line for this section, one can again line up the krypton particle balance:

$$\dot{F} \cdot x_F + \dot{V}' \cdot y_{-1} + \dot{L} \cdot x_{+1} = \dot{V} \cdot y_0 + \dot{L}' \cdot x_0 \tag{4.28}$$

With ideal feeding $y_0 = y_{-1} = y$ and $x_0 = x_{+1} = x$ follows:

$$y = \frac{q}{q-1} \cdot x - \frac{x_F}{q-1} \tag{4.29}$$

This relation is the intersection line of the collection line of the rectifying section and the condensation line of the stripping section, on which the two lines cross.

4.2.3 McCabe-Thiele diagram

Putting together the different graphs from the latest sections, the McCabe-Thiele diagram with the concentration of krypton in the liquid phase on the abscissa axis and the concentration of the krypton in the gaseous phase on the ordinate axis can be drawn. The process of cryogenic distillation takes place between the equilibrium line and the operating line. On the left side from the intersection point, the condensation line pertains. The collection line pertains on the right side. To obtain the number of theoretical stages, one can do a step by step construction of each stage starting at the concentration x_D and stopping at concentration x_B. Four stages are needed in the schematic example. A schematic drawing of a full diagram is shown in figure 4.8.
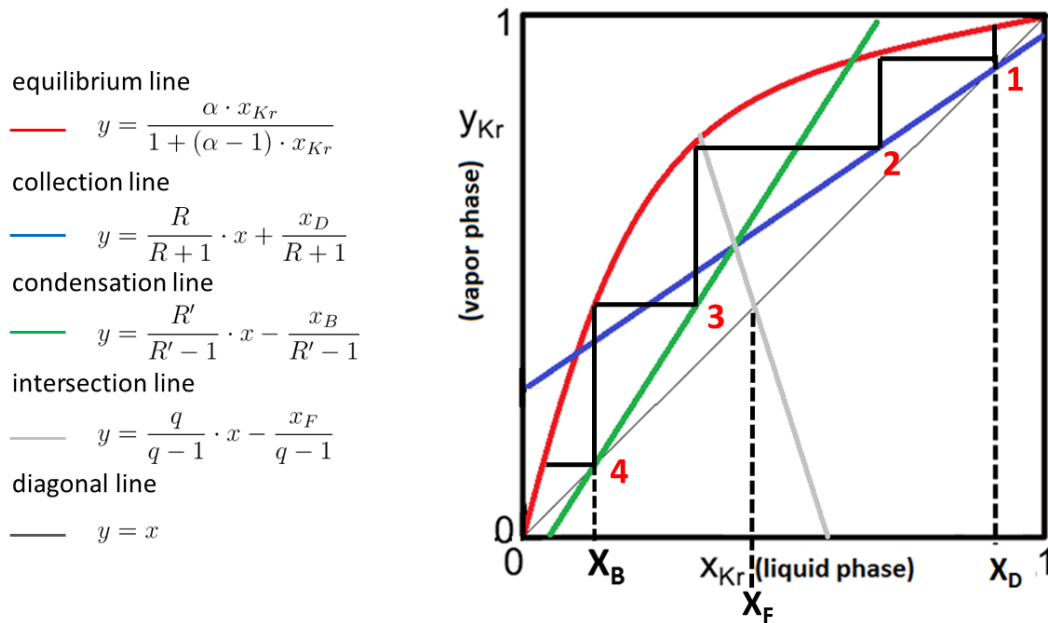
Figure 4.8: *A schematic drawing of a McCabe-Thiele-diagram. The concentration of krypton in the liquid and gaseous phase are plotted against each other. The equilibrium line (red), collection line (blue), condensation line (green), intersection line (grey) and diagonal line (dark grey) are shown. The three operation lines can be obtained by calculation of the krypton particle mass balance in a certain section. For liquid concentrations (x_{Kr}) lower than the intersection point the condensation line is valid, for higher concentrations the collection line. Using a step by step construction starting at concentration x_D, one can obtain the number of theoretical stages. In this example four stages are needed.*

Using the calculated parameters for the Muenster distillation column, the McCabe-Thiele diagram for a gaseous and a liquid feed are shown in figure 4.9 and 4.10. For the gaseous phase it is shown that in total 10 theoretical stages are needed to reach a krypton in xenon level of 1 ppt for the given design parameters. If the feed is changed to liquid, the condensation line is slightly different from before due to the change of the reflux ration R' from the bottom of the column. As shown above, the liquid is fully

added to the liquid stream $\dot{L}'$. The amount of evaporated xenon in the reboiler must be increased as a result of mass conservation. Thus, the mass transfer between the liquid stream and gaseous stream is enhanced. In consequence, the number of required stages is reduced to 9 stages. For a mixture of a gaseous and liquid feed the number of stages is either 9 or 10, changing at some point.

Because the column will be tested in all three different ways with gas only, liquid only and a mixture feed, the estimation of the final height of the column will be done with 10 stages and is shown in the next section.

The location of the feed point depends on the concentration of krypton inside of the incoming xenon, which has to be added to a stage with an equal composition in order to achieve an effective distillation process. Due to that fact, several feed ports along the column have to be installed at different heights.
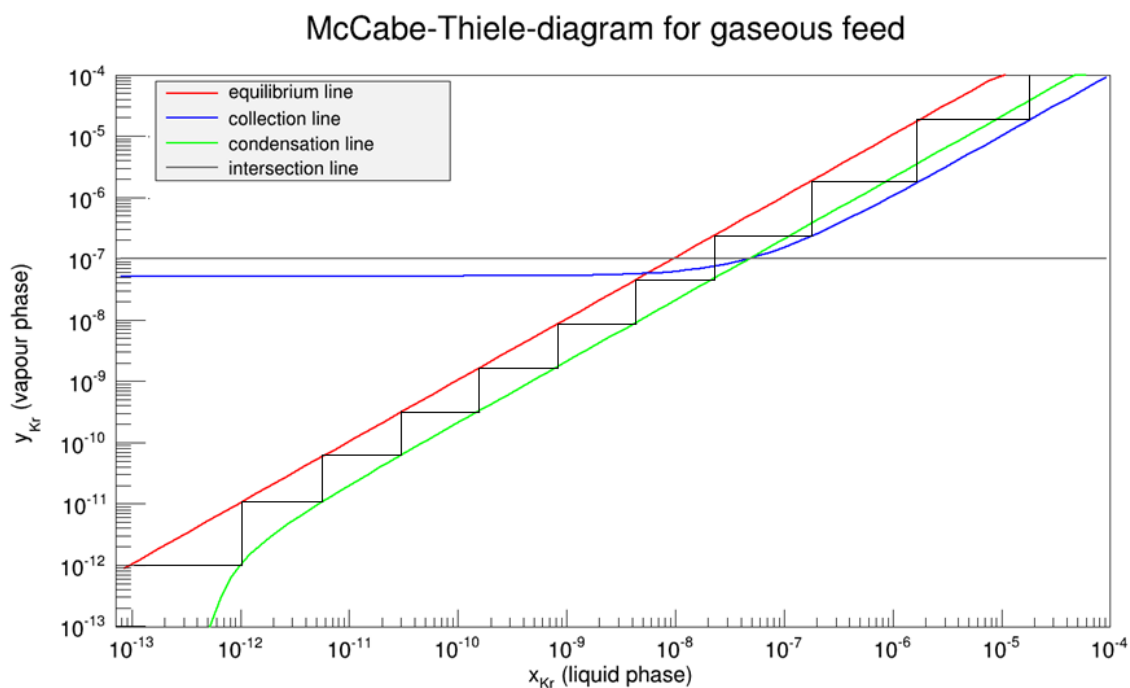
Figure 4.9: *The McCabe-Thiele diagram for a gaseous feed of the new cryogenic distillation column of Muenster. The equilibrium line, collection line, condensation line and intersection line are shown. The number of required theoretical stages are determined to be 10 stages to reach a krypton in xenon level of 1 ppt using a step by step construction.*
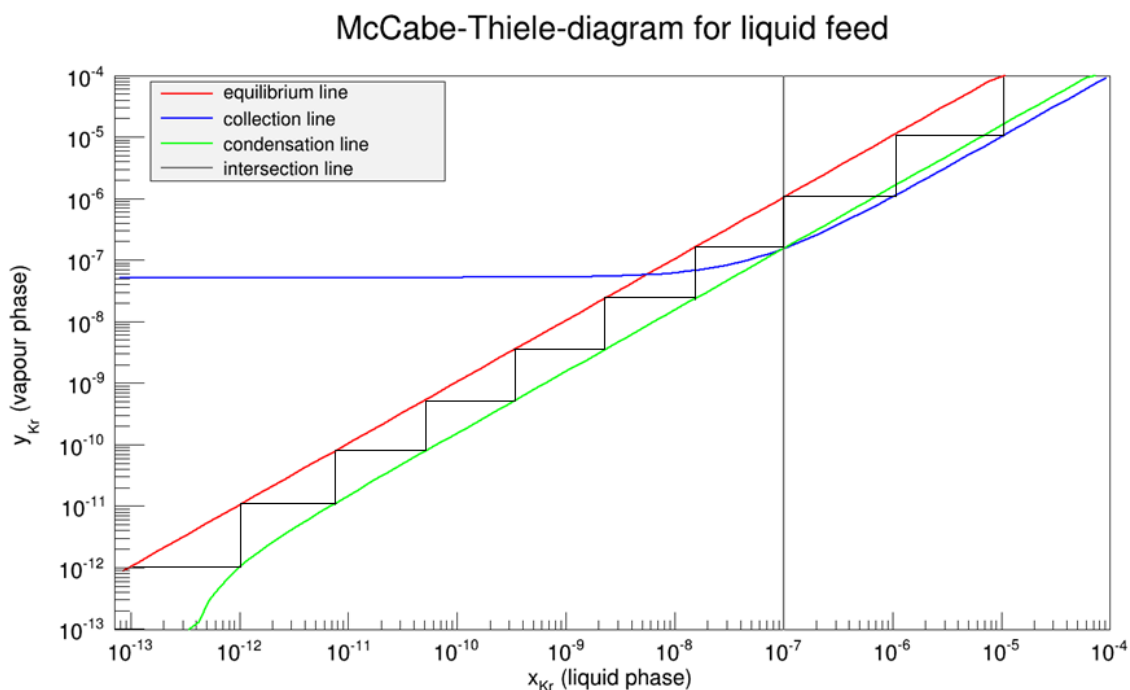

Figure 4.10: *The McCabe-Thiele diagram for a liquid feed of the new cryogenic distillation column of Muenster. The equilibrium line, collection line, condensation line and intersection line are shown. The number of required theoretical stages are determined to be 9 stages to reach a krypton in xenon level of 1 ppt using a step by step construction.*

4.3 Determination of the final height
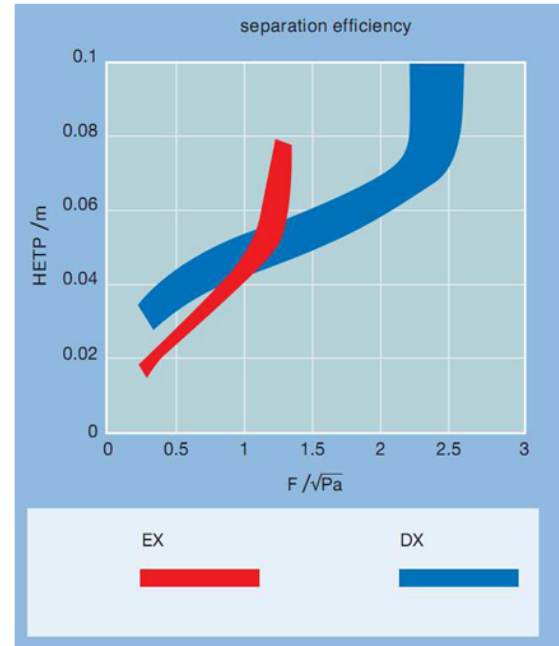
Figure 4.11: *On the left: The used structured packing material Sulzer EX inside the column tube is shown. On the right: The dependence of the HETP-value from the gas load F for two different kinds of packing material from the company Sulzer are shown. The higher the gas load F is, the higher the packing material to act as one theoretical stage at a given separation factor must be. Diagram taken from [Sul].*

The final height of the distillation column can be calculated with the number of theoretical stages and the HETP-value (Height Equivalent for one Theoretical Plate) that is specific for the used packing material inside the column tube. The structured packing material as shown in figure 4.11 is used in order to enlarge the surface inside the column. For higher surfaces the interaction between the liquid and gas stream is enhanced and therefore also the mass transfer. In consequence, the transmission of krypton from the liquid into the gas phase is increased. Thus, the separation efficiency is also increased. The HETP-value gives the height of the packing material that corresponds to one theoretical stage. The final height is then given by:

$$H = N_{th} \cdot \text{HETP} \tag{4.30}$$

The HETP-value and therefore the separation efficiency of the used packing material Sulzer EX depends on the gas load F during the distillation process as shown in figure 4.11. For higher gas loads, the HETP-value is enlarged and consequently the separation efficiency is reduced for a fixed height of the package. In the following, the maximum HETP-value corresponding to the lowest separation efficiency will be calculated. All values below this maximum would lead to a smaller and therefore not efficient enough distillation column.

The gas load F is defined as:

$$F = u_v \cdot \sqrt{\rho_{GXe}} \tag{4.31}$$

The density ρ_{GXe}=18.68 kg/m^3 [NIST] is given by the operation conditions at a temperature of 178 K and a pressure of 2 bar. In order to obtain F, the gas velocity u_v of the vapour stream has to be calculated beforehand. The velocity u_{empty} for the empty column tube depends on the amount of the evaporated xenon $\dot{V}'$ from the reboiler and the diameter d_c=45 mm of the column:

$$u_{empty} = \frac{4 \cdot \dot{V}'}{\pi \cdot d_c^2 \cdot \rho_{GXe}} \tag{4.32}$$

The highest gas load that correspond to the maximum HETP-value, is reached for $\dot{V}'$=5.76 kg/h, assuming a liquid feed. That gives:

$$u_{empty} = \frac{4 \cdot 5.76 \, \text{kg/h}}{\pi \cdot (45 \, \text{mm})^2 \cdot 18.68 \, \text{kg/m}^3} = 0.054 \, \text{m/s} \tag{4.33}$$

The inserted packing material reduces the cross section of the throughflow of the vapour stream and as a result, the gas velocity is enhanced. Because it is not possible to calculate the gas velocity at each location inside the column, the real gas velocity is calculated as a mean effective velocity depending on the voidage ϵ introduced by the packing:

$$u_v = \frac{u_{empty}}{\epsilon} \tag{4.34}$$

According to the company Sulzer, the voidage of the packing is between 90-97%. In order to get the maximum HETP-value, ϵ=90 % was chosen:

$$u_v = \frac{0.054 \, \text{m/s}}{0.90} = 0.060 \, \text{m/s} \tag{4.35}$$

With that, the gas load F is:

$$F = 0.06 \, \text{m/s} \cdot \sqrt{18.68 \, \text{kg/m}^3} = 0.26 \, \text{Pa}^{1/2} \tag{4.36}$$

According to figure 4.11 the HETP-value would be $\sim$20 mm, but this diagram is based on a standard mixture, such as Benzene/Toluene at concentrations at least in the percentage range. The behaviour of the mixture Kr/Xe at such low concentrations is rather unknown and therefore the HETP-value was conservatively enlarged in discussion with Sulzer to be $\sim$30 mm in a first step. With the number of 10 theoretical stages, the final height of the column is determined as the following:

$$H = 10 \cdot 30 \, \text{mm} = 300 \, \text{mm} \tag{4.37}$$

That would lead to a final height of 30 cm, but the limitation of the McCabe-Thiele method due to the low krypton concentrations in xenon was neglected until now. It was designed for "higher" concentration and has not been tested for the regime between 10^{-5}-10^{-12} yet. As explained, the method is based on the concept of vapour pressure, describing the "probability" that an atom migrates from liquid into gas phase until the equilibrium between the two phases is reached. This process is

governed by the atom-atom or molecule-molecule binding energies, but neglects the interaction between atom-surface or molecule-surface interactions, such as the interaction with the packing material. The assumption was made, that at least one monolayer (or more) shall cover the packing material of the column, so that atom-atom interaction is dominant over surface interaction. An estimation about the number of monolayers covering the surface inside the column per one meter of height was done and is presented in the following.

4.3.1 Calculation of the number of monolayers per one meter column height

In a first step, the size of the surface inside the column has to be calculated. 20 pieces of the package with a diameter of 39 mm and height of 53 mm each are needed for one meter column height. According to the company, the surface is given by $1500 \, \text{m}^2/\text{m}^3$. Furthermore, the surface of the column tube itself with a diameter of 45 mm has to be added. That gives a total surface of:

$$A_{total} = A_{packing} + A_{tube} = 2.04 \, \text{m}^2 \tag{4.38}$$

In a next step, the surface of one xenon particle is calculated with the van-der-Waals radius of 216 pm, assuming the xenon particle to be spherical. Using the total surface, the number N_{Xe} of xenon particles for one monolayer can be obtained.

$$N_{Xe} = \frac{A_{tot}}{A_{Xe}} = \frac{2.04 \, \text{m}^2}{1.47 \cdot 10^{-19} \, \text{m}^2} = 1.39 \cdot 10^{19} \tag{4.39}$$

This value can be translated into the weight $m_{Xe,ML}$ of one monolayer xenon using the Avogadro constant and the molar mass of M_{Xe}=131.3 g/mol:

$$m_{Xe,ML} = 3.03 \cdot 10^{-3} \, \text{g} \tag{4.40}$$

In order to achieve the number of monolayers, the amount of liquid xenon inside the column for a certain time interval has to be known. That can be calculated via the velocity of the liquid stream depending on the flow parameter $\dot{L}'$ and cross section of the column:

$$u_l = \frac{\dot{L}'}{A_c} = 0.000\,35 \, \text{m/s} \tag{4.41}$$

For a section of 1 m, the calculated velocity corresponds to an amount of liquid xenon of $\sim$455 g. Using the amount for one monolayer, the total number of monolayers can be calculated to be:

$$N_{ML} \sim 150\,000 \tag{4.42}$$

In the beginning, it was asked for at least one monolayer of liquid xenon to cover the surface of the packing material in order to allow the concept of vapour pressure. That is definitely fulfilled, shown by the estimation above. The biggest uncertainty is given by the calculation of the liquid velocity. The influence of friction between the liquid and the packing material was neglected. However, introducing the friction would lead to a lower velocity and thus to an even higher amount of monolayers.

Now that the basic requirements for the concept of vapour pressure are given, the influence of such

low krypton concentrations has to be discussed. By definition of vapour pressure, all krypton particles should be in the gas phase and not in the liquid phase at the operation conditions, but nevertheless there are still some in the liquid phase. The concentration of krypton is so low, that one krypton particle in the liquid is completely surrounded by xenon particles. It's obvious that the binding energies between the xenon atoms are higher than between the krypton and xenon. Taking this into account, if energy is introduced, e.g. by heating power, the "probability" for the transition from liquid phase to gas phase is higher for a certain krypton particle than for a certain xenon particle. This portability can be seen as vapour pressure. In consequence, there should be as much interactions as possible between the gas and liquid phase to remove the krypton from the liquid phase.

Therefore, the HETP-value was further enhanced by a factor of 10 in order to be conservative and to reach the pre-defined purification. The final height of the packing tube is then determined to be:

$$H = 3000\,\text{mm} = 3\,\text{m}. \tag{4.43}$$

4.4 Heating and cooling power

In this section the required cooling and heating power during the distillation process will be calculated for the different cases of a gaseous and a liquid feed.

Table 4.1: *Saturation properties for xenon. Data taken from [NIST].*

Phase	Pressure (bar)	Temperature (K)	Enthalpy h (kJ/kg)
liquid	2	178	4.4
vapour	2	178	96.9

4.4.1 Gaseous feed

In a first step, the incoming xenon has to be cooled from room temperature of $300\,\text{K}$ down to the operation temperature of $178\,\text{K}$. The specific heat capacity of xenon is quite constant over a wide range of temperatures, so that the required cooling power is given by:

$$\begin{aligned}
\dot{Q}_{CD} &= \dot{m} \cdot c_p \cdot \Delta T \\
&= 3\,\text{kg/h} \cdot 0.17\,\text{kJ/kgK} \cdot 122\,\text{K} \\
&= 62.2\,\text{kJ/h} \\
&= 17.3\,\text{W}
\end{aligned} \tag{4.44}$$

In the next step, the cooled gas is fed into the column and is fully added to the vapour stream $\dot{V}$. At the top, almost all of the xenon is liquefied and refilled into the column. Only a small amount is taken out as krypton enriched off-gas. The required cooling power depends on the enthalpy of the vapour

and liquid phase that is shown in table 4.1 and is calculated to be:

$$
\begin{aligned}
\dot{Q}_C &= \dot{L} \cdot \Delta h_{v,Xe} \\
&= 5.73\,\mathrm{kg/h} \cdot \left(96.9\,\mathrm{kJ/kg} - 4.4\,\mathrm{kJ/kg}\right) \\
&= 530.0\,\mathrm{kJ/h} \\
&= 147.2\,\mathrm{W}
\end{aligned}
\tag{4.45}
$$

The heating power depends upon the amount of xenon that has to be evaporated in the reboiler due to mass conservation. For a gaseous feed the vapour stream $\dot{V}'$ is 2.76 kg/h and therefore the required heating power is:

$$
\begin{aligned}
\dot{Q}_H &= \dot{V}' \cdot \Delta h_{v,Xe} \\
&= 2.76\,\mathrm{kg/h} \cdot \left(96.9\,\mathrm{kJ/kg} - 4.4\,\mathrm{kJ/kg}\right) \\
&= 255.3\,\mathrm{kJ/h} \\
&= 70.9\,\mathrm{W}
\end{aligned}
\tag{4.46}
$$

4.4.2 Liquid feed

Assuming a liquid feed, the energy balance of the column will change. For the first cooling down of the incoming gaseous xenon a power of 17.2 W is required as shown in equation 4.44. In addition, further cooling power is necessary in order to liquefy the xenon. For a feed flow rate of $\dot{F}{=}3\,\mathrm{kg/h}$ follows:

$$
\dot{Q}_L = \dot{F} \cdot \Delta h_{v,Xe} = 77.1\,\mathrm{W}
\tag{4.47}
$$

In total, a cooling power of 94.3 W is required to provide a liquid feed.

In the next step, the liquid is fed to the column and fully added to the liquid stream $\dot{L}'$. Because of the fact that the flows of the rectifying section $\dot{V}$, $\dot{L}$ and $\dot{D}$ are independent from the composition of the feed as shown in section 4.2.2, the cooling power at the top is the same as for a gaseous feed:

$$
\dot{Q}_C = 147.2\,\mathrm{W}
\tag{4.48}
$$

As a consequence of a liquid feed, the liquid stream $\dot{L}'$ is enhanced and therefore a higher amount of xenon has to be evaporated in the reboiler as a result of mass conservation. Thus, more heating power is required at the bottom of the column. With the vapour stream $\dot{V}'{=}5.76\,\mathrm{kg/h}$ follows:

$$
\dot{Q}_H = \dot{V}' \cdot \Delta h_{v,Xe} = 148.0\,\mathrm{W}
\tag{4.49}
$$

This is the maximally required heating power. The comparison of the cooling and heating power shows, that for a full liquid feed, the required powers are almost equal. For a mixture of the composition, the heating power is between the calculated values of a gaseous and a liquid feed.

The experimental equipment to provide the needed cooling and heating power will be presented in the next chapter.

4.5 Floodpoint of the distillation column

For higher mass flows, the interaction between the up-going gaseous and down-going liquid phase of xenon is increased and thus a better separation efficiency can be achieved.

These flows along the packing material can be enhanced by increasing the heating and cooling power. The pressure drop along the column tube stays constant during increasing heating power, until the floodpoint of the distillation column is reached. At this point, the amount and velocity of gaseous xenon is such high, that droplets from the liquid stream are torn up. As a result of that, the differential pressure between the top and bottom raises and no stable operation is possible any more. A schematic diagram is shown in figure 4.12.

It's advisable to work 20 % below the floodpoint in order to have a good compromise between a high separation and a safely operation.

In the case of the distillation column from Muenster, a differential pressure around 1 mbar is recommended.
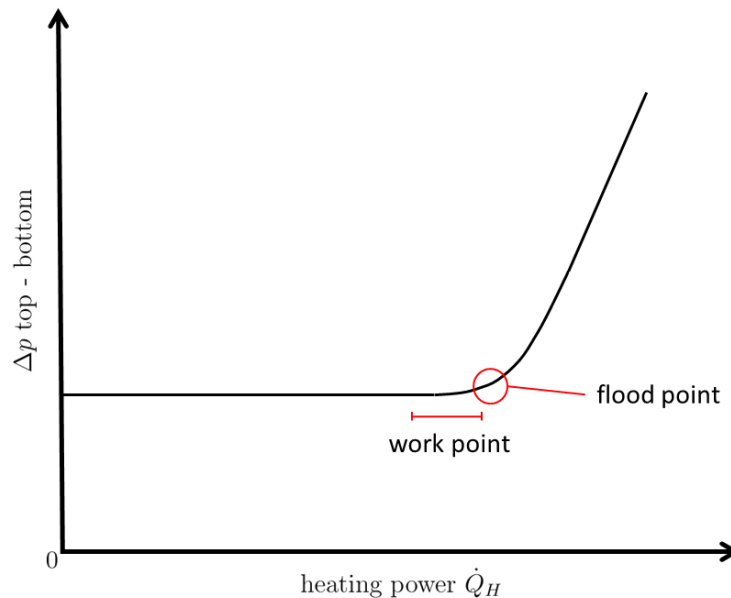
Figure 4.12: *Schematic diagram of floodpoint. The differential pressure along the column against an increasing heating power is shown. At the floodpoint, the pressure raises and no stable operation is possible any more.*

5 Experimental set-up of the cryogenic distillation column in Muenster

The new cryogenic distillation column for the XENON1T experiment was designed in Muenster according to the parameters described in the last chapter. The experiment is split into a two-phase set-up. In order to ensure easier handling and for a number of performance tests, it was decided to build a distillation column with a packing material of only 1 m as opposed to 3 m for the first step. This column only differs in the height of the packing material, while the main components, such as preseparator, reboiler and top condenser, are the same as for the final column.

Considering the high purity of xenon, the cleanness of the installed components of the system, especially those which are in contact with the xenon, is a crucial key factor for the success of such an experiment. Therefore, all used pipes and tubes are electropolished stainless steel 316L and 316LN. The connections are made either by VCR connections with metal gaskets or copper sealed CF flanges. The fittings for the VCR connection are orbitally welded to the pipes. Also, the packing material is 100 SS 316L and has been treated with the same meticulous cleaning process as every component. All parts have been cleaned two times in an ultrasonic bath, first with a special cleaning agent (Almeco$^{\textcircled{C}}$), second with deionized water.

Before filling the column with xenon, the system is evacuated and baked out. The maximal temperature for baking the entire set-up is limited by the coldhead in the top of the column with 50 °C. This section has to be heated carefully. Other parts such as the packing material can easily be baked with a much higher temperature of ∼100 °C. After the baking, gaseous xenon is circulating through the column and a hot getter in order to reduce the remaining electronegative impurities.

The vacuum components such as the insulation vessels and tubes are made of SS 304 and are viton sealed.

In this chapter an overview of the main components of the 1 m distillation column, which is shown in the technical drawing in figure 5.1, will be presented. A picture of the whole set-up is shown in 5.2. The description is split into three major parts: The bottom, the middle and the top of the column.

The assembling of the complete set-up was done together with Stephan Rosendahl, who will also describe the system in his upcoming PhD-thesis, and Christian Huhmann, who made all the technical drawings, shown in this chapter.
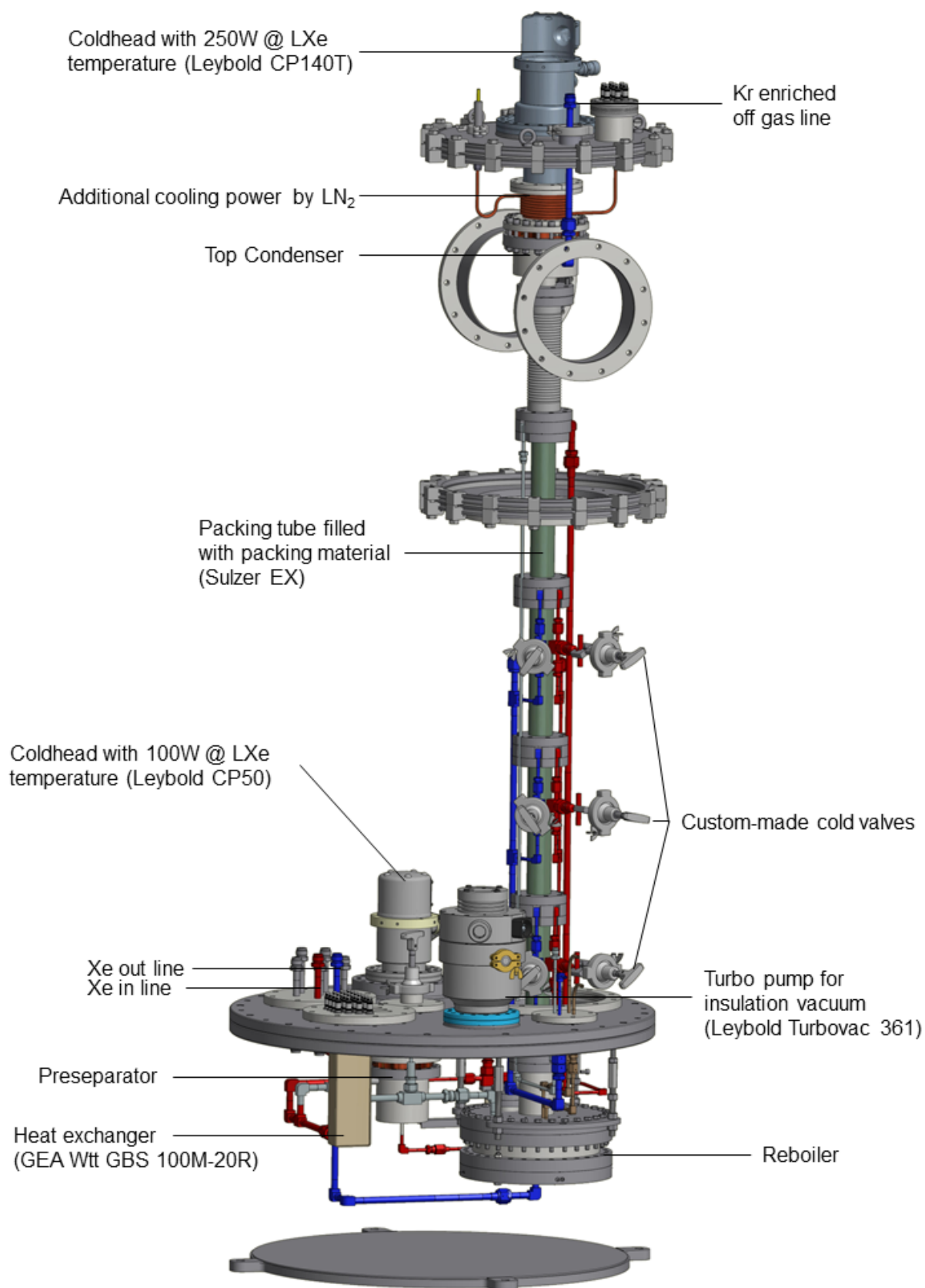
Figure 5.1: *Technical drawing of the 1 m distillation column. The main features such as the reboiler and preseparator at the bottom, the tube with the packing material inside in the middle and the top condenser at the top of the column are shown. Drawing done by C.Huhmann.*
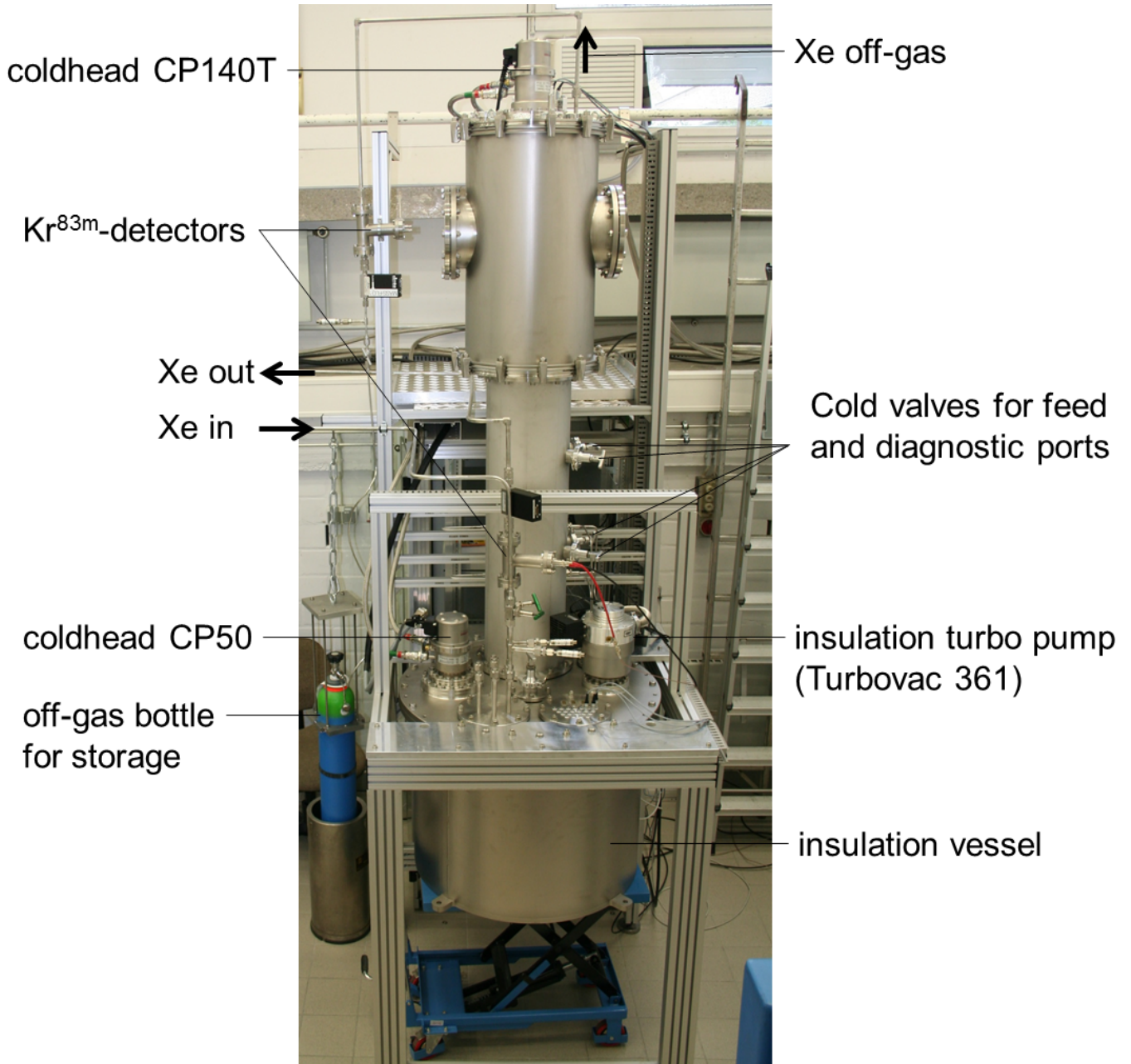
Figure 5.2: *A picture of the whole set-up is shown, along with the supply line (Xe in), the return line (Xe out) and the off-gas line (Xe off-gas). A ^{83m}Kr-detector has been inserted into each of the lines in order to analyse the separation efficiency of the column. Two of them are visible in the picture. Both coldheads that are used for cooling down and that liquefy the xenon, as well as the insulation vessel that is evacuated by a turbo pump, are indicated. Several diagnostic and feed ports can be opened and closed using custom-made cold valves.*

5.1 Bottom part: Pre-cooling and reboiler

Figure 5.3: *An insight into the bottom insulation vessel is shown. It contains the heat exchanger and the preseparator which are used to cool down and liquefy the xenon as well as the reboiler that is used to evaporate the xenon during the distillation process.*

The bottom part of the column is made of an extensive insulation vessel with a diameter of $750\,\mathrm{mm}$ and a height of $600\,\mathrm{mm}$ in order to separate the components from thermal contact to the outside during the distillation process. An insulation vacuum in the range of $10^{-8}\,\mathrm{mbar}$ was achieved with a rotary vane pump (Trivac D16B, Leybold) as the fore pump and a turbomolecular pump (Turbovac 361, Leybold). The measurement was taken with a pressure sensor from Leybold (PTR90 Penningvac).
The vessel is closed with a custom-made flange that provides several feed-throughs for pumping, piping and electrical wires. It houses three main components of the distillation system, namely the heat exchanger, the preseparator and the reboiler. These devices will be presented in the following sections.

5.1.1 Preseparator and heat exchanger

The cooling tower in this part, often referred to as preseparator, consists of three components: In order to collect the liquid xenon, the housing of the funnel-shaped input condenser (d=100 mm, h=93mm) is connected to a Gifford-McMahon (GM)-type refrigerator (CP 50, Leybold) over a lamellar structured piece of (OFHC) copper which works as a gasket itself, as shown in figure 5.4. The cooling fins are used to enlarge the surface of the condensation of the incoming xenon. Two heat cartridges with a power of 100 W each and a Si-diode (DT-670D-DI, Lakeshore) temperature sensor as well as a PT1000 sensor are installed on the copper inside the cooling tower. In addition, three PT1000 temperature sensors are connected to the outside of the condenser in order to estimate the liquid level in the preseparator

during the operation process. The cold head can be dismounted without opening the cooling tower, e.g. for maintenance.

This device should provide a cooling power of about 100 W at the operation conditions in order to
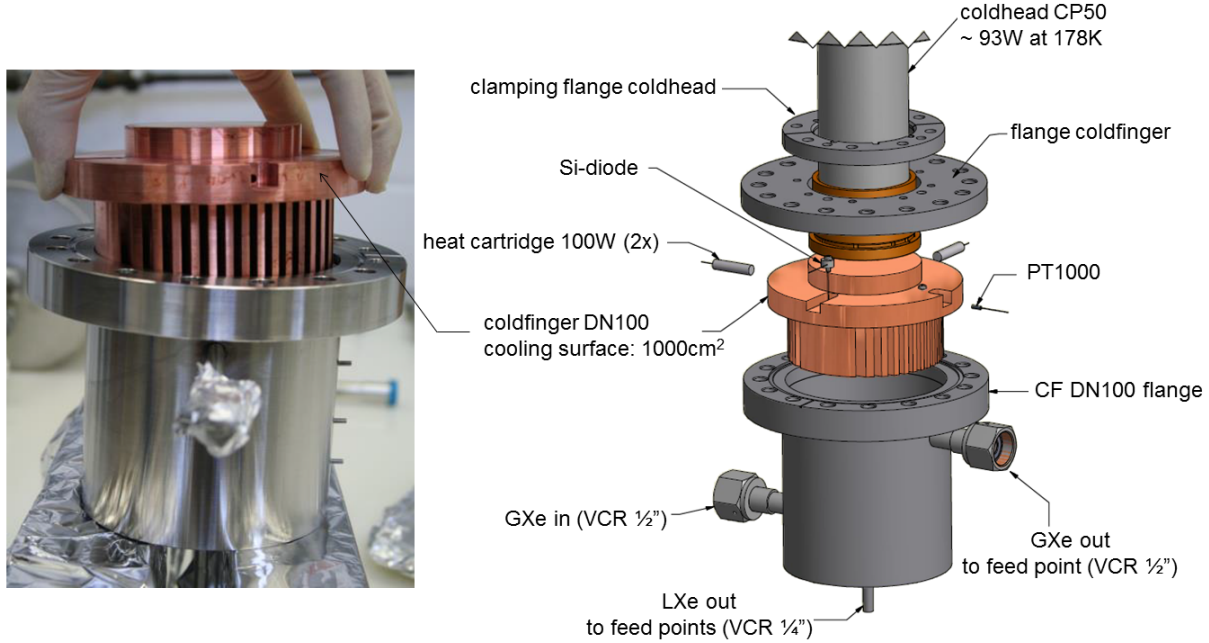

Figure 5.4: *On the right, a technical drawing of the several components of the preseparator is shown. The cooling tower is made of a vessel, a copper coldfinger and a coldhead CP50. The port for the xenon supply line as well as the gaseous and liquid feed lines are indicated. For temperature and cooling power control a Si-diode and heat cartridges are applied to the copper. On the left a picture of the preseparator during the assembling is shown. Technical drawing done by C. Huhmann.*

cool down the gas and liquefy the xenon. The cooling power at a temperature of 178 K for a coldhead of the same type was measured to be ∼93 W in a similar set-up in [Sch11] and is shown in figure 5.5. That value is reasonable, assuming possible thermal losses due to contact such as the contact to the insulation vessel.

The maximal required cooling power for a liquid feed is 94.3 W as described in 4.4.

The comparison shows, that the preseparator alone is unable to cool and liquefy the incoming xenon. Thus, the supply line containing the warm xenon as well as the return line containing the liquid purified xenon from the reboiler are connected to a plate heat exchanger (GEA Wtt GBS 100M-20R), so that the incoming warm xenon is cooled by the out-going xenon. In consequence, a gaseous and liquid feed can be provided by the combination of the heat exchanger and the cooling tower.

Due to the fact, that some fraction of the xenon stays in the gaseous phase, while the rest is liquefied in the vessel, a first separation between krypton and xenon takes place. Therefore, the vessel can be seen as a first distillation stage and is called preseparator as a result. First preseparation tests have been done during the construction of the full system and will be presented in [Ros14].

Due to the funnel shaping, the liquid xenon is collected at the bottom of the preseparator. By creating
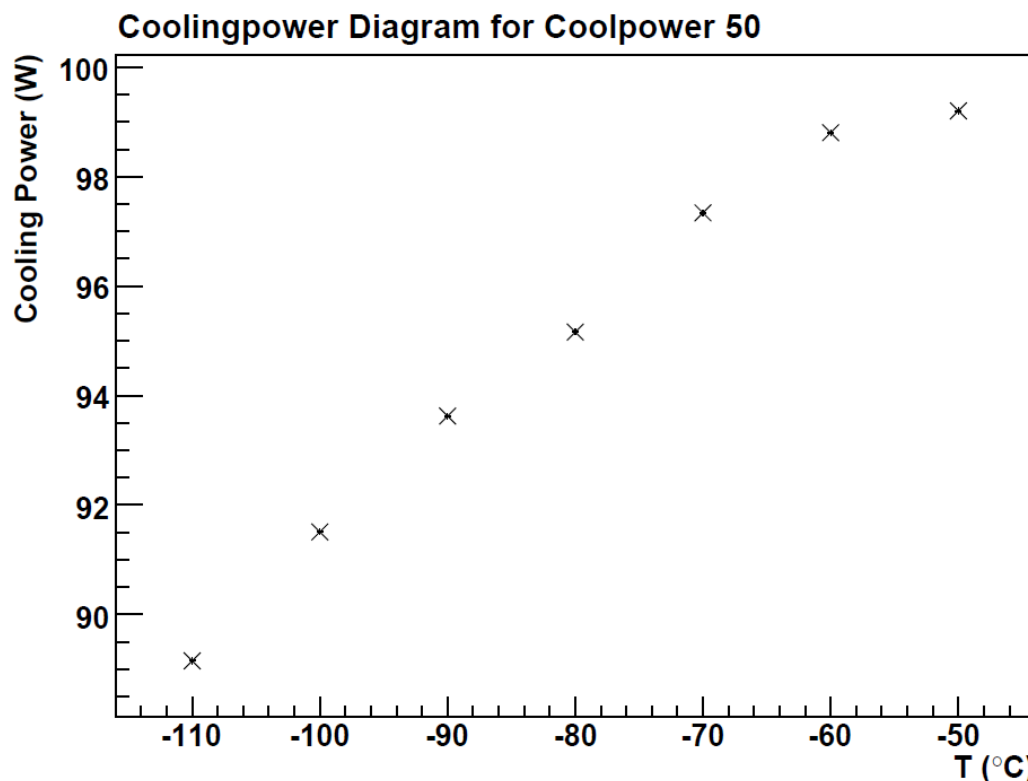

Figure 5.5: *Cooling power as a function of the temperature at the end of the cold head for the MS-TPC setup, which uses the same components as the cooling tower in the bottom part of the column. The power is calculated by measuring the current through a 100 W heater for different temperature set-points. The error bars of this measurement are smaller than the symbols. Caption and figure taken from [Sch11].*

an overpressure in this device, it is possible to push the liquid upwards to three different feedpoints that differs only in height. These feedpoints can be closed off by custom-made cold valves and are shown in section 5.2. Over a bypass-valve it is also possible to directly connect the preseparator and the reboiler.

Additionally, the possibility of a gaseous feed is given due to an extra line at the top of the preseparator up to the very top of the column. This line can be closed off by a specially-made cold-valve that can regulate the flow of the gaseous feed. A potentiometer with a $1\,k\Omega$ resistance and 10 turns that is connected via two gears to the shaft of the valve, gives the possibility of reading the actual position, depending on the resistance of the potentiometer. The transmission between the two gears was designed to be 1:3, so that one turn of the valve corresponds to three turns of the potentiometer. The valve is turned by a stainless steel fork that is connected to the outside in order to reduce thermal losses at this location as shown in figure 5.6. Conductance measurements for several valve positions have been done and will be presented in chapter 6.
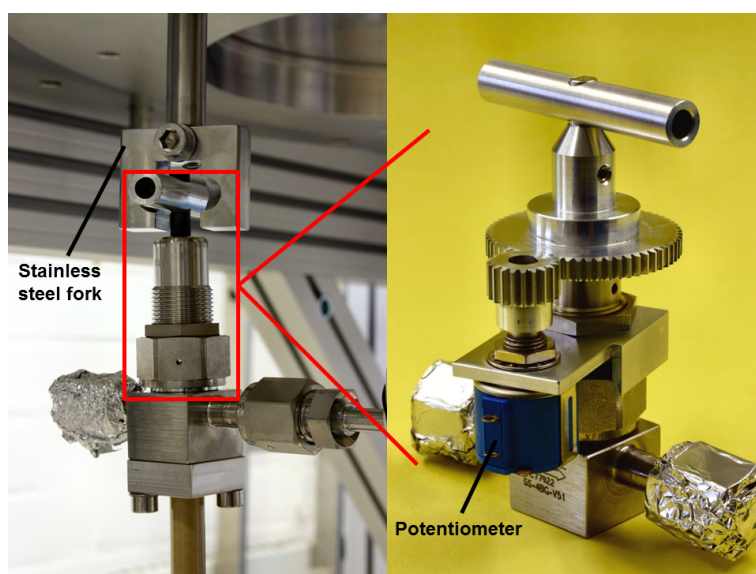
Figure 5.6: *On the left, the original installation of the cold valve for the gaseous feed line is shown. The valve is turned by a custom-made stainless steel fork that is guided to the outside of the vessel in order to avoid thermal losses during the distillation process. In the new installation, a potentiometer (1 kΩ, 10 turns) is connected via two gears to the shaft of the valve as shown on the right, with which the actual position of the valve can be read out, depending on the resistance of the potentiometer.*

5.1.2 Reboiler

Another main component of the distillation process is called the reboiler, which is a cylindrical, stainless steel vessel with a diameter of 250 mm and a height of 75 mm, closed on both sides with CF flanges as shown in figure 5.7. In the funnel-shaped bottom, the return line that is connected to the heat exchanger is installed in order to extract the purified xenon. On the top flange, the reboiler is connected to the packing tube. The vessel can store up to 3 l of liquid xenon and is held by four rods that are connected to the insulation vessel. In order to reach the required heating power of ∼300 W, as described in 4.4, 2×2 heater cartridges of 150 W each are installed at the bottom. The temperature in this location is measured via a silicon diode (DT-670D-CU, Lakeshore) and in addition, via a PT1000 sensor as coverage.

In order to monitor the amount of liquid xenon inside the vessel, two different methods to determine the liquid level are applied. Four PT1000 temperature sensors are installed at different heights inside the vessel. If the liquid reaches a sensor, the temperature will drastically decrease as an indication for reaching the liquid level.

The other method includes measuring the differential pressure inside the reboiler between two pipes that are guided into the vessel. One stops at the top and one towers to the bottom as shown by the yellow pipes in figure 5.7. Depending on the liquid level, the hydrostatic pressure will change and thus, the differential pressure. One calculation for a certain temperature and pressure is shown in figure 5.7
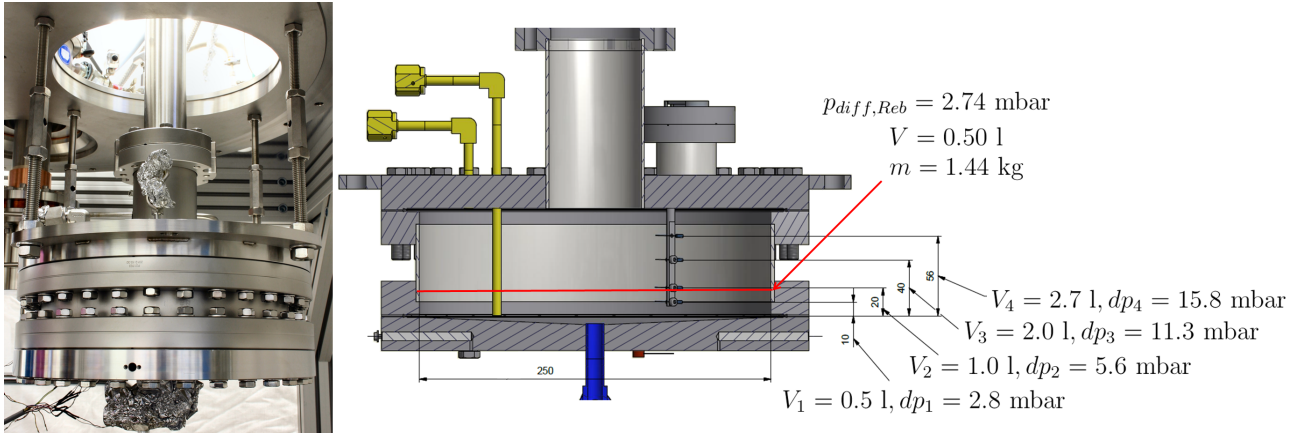
$$p_{diff,Reb} = 2.74 \text{ mbar}$$
$$V = 0.50 \text{ l}$$
$$m = 1.44 \text{ kg}$$

$$V_4 = 2.7 \text{ l}, dp_4 = 15.8 \text{ mbar}$$
$$V_3 = 2.0 \text{ l}, dp_3 = 11.3 \text{ mbar}$$
$$V_2 = 1.0 \text{ l}, dp_2 = 5.6 \text{ mbar}$$
$$V_1 = 0.5 \text{ l}, dp_1 = 2.8 \text{ mbar}$$

Figure 5.7: *On the left picture the mounted reboiler is shown. It is held by four rods and can store up to 3 l of liquid xenon. On the right, a technical drawing is shown. The yellow coloured pipes are used to measure the differential pressure inside the vessel that depends on the change in the liquid level. The determination of the level for one measurement with a differential pressure of 2.74 mbar at a temperature of −98.7 °C and a pressure of 1.7 bar is indicated by the red line. The heights of the four PT1000 temperature sensors as a second method are shown translated to the expected corresponding differential pressure. Technical drawing by C. Huhmann.*

and will be briefly presented in the following:

Liquid level inside the reboiler

The calculation is based on the concept of hydrostatic pressure that depends on the height of the liquid level inside the reboiler and on the density of the liquid xenon which in turn depends on the temperature and pressure inside the vessel. For a measured temperature of −98.7 °C and a pressure of 1.7 bar the density of the liquid is 2878.3 kg/m^3 [NIST]. It is assumed that the reboiler is cylindrical, neglecting the small influence by the funnel shape in the bottom. With

$$p_{diff} = \rho_{LXe} \cdot g \cdot h \tag{5.1}$$

and the determined differential pressure of $p_{diff}=(2.74 \pm 0.20)$ mbar the height of the liquid level can be determined to be:

$$h_{2.74 \ mbar} = (1.0 \pm 0.1) \text{ cm}. \tag{5.2}$$

Using the diameter $d_{reb}=250$ mm the volume of the liquid is:

$$V = \pi \cdot \left(\frac{d_{reb}}{2}\right)^2 \cdot h = (0.5 \pm 0.1) \text{ l} \tag{5.3}$$

Together with the determined density, that volume corresponds to an amount of xenon of (1.44 ± 0.30) kg. In addition, the height of the installed temperature sensors can be translated into differential pressures

that are also dependent upon the prevailing temperature and pressure conditions and the values can be compared. The related heights and differential pressures are:

$$h_1 = 1.0\,\text{cm} \rightarrow p_1 = 2.8\,\text{mbar}$$
$$h_2 = 2.0\,\text{cm} \rightarrow p_2 = 5.6\,\text{mbar}$$
$$h_3 = 4.0\,\text{cm} \rightarrow p_3 = 11.3\,\text{mbar}$$
$$h_4 = 5.6\,\text{cm} \rightarrow p_4 = 15.8\,\text{mbar} \tag{5.4}$$

According to the values, the liquid level in this measurement is around the first temperature sensor and therefore only this sensor should indicate that it is covered in liquid. In figure 5.8, the confirmation of the calculations, using a measurement during a filling process, is shown. In the top diagram, the rising differential pressure depending on the rising of the liquid in the reboiler can be observed. In the bottom diagramm, the four temperatures measured by the PT1000 sensors are indicated. All four temperatures are falling as a result of the cool down by cold xenon gas in the reboiler, but only the bottom PT1000 sensor (red) indicates the liquid level at a temperature of $-96.7\,^{\circ}\text{C}$, while the other three sensors stay in the gaseous phase, shown by their measured temperatures.
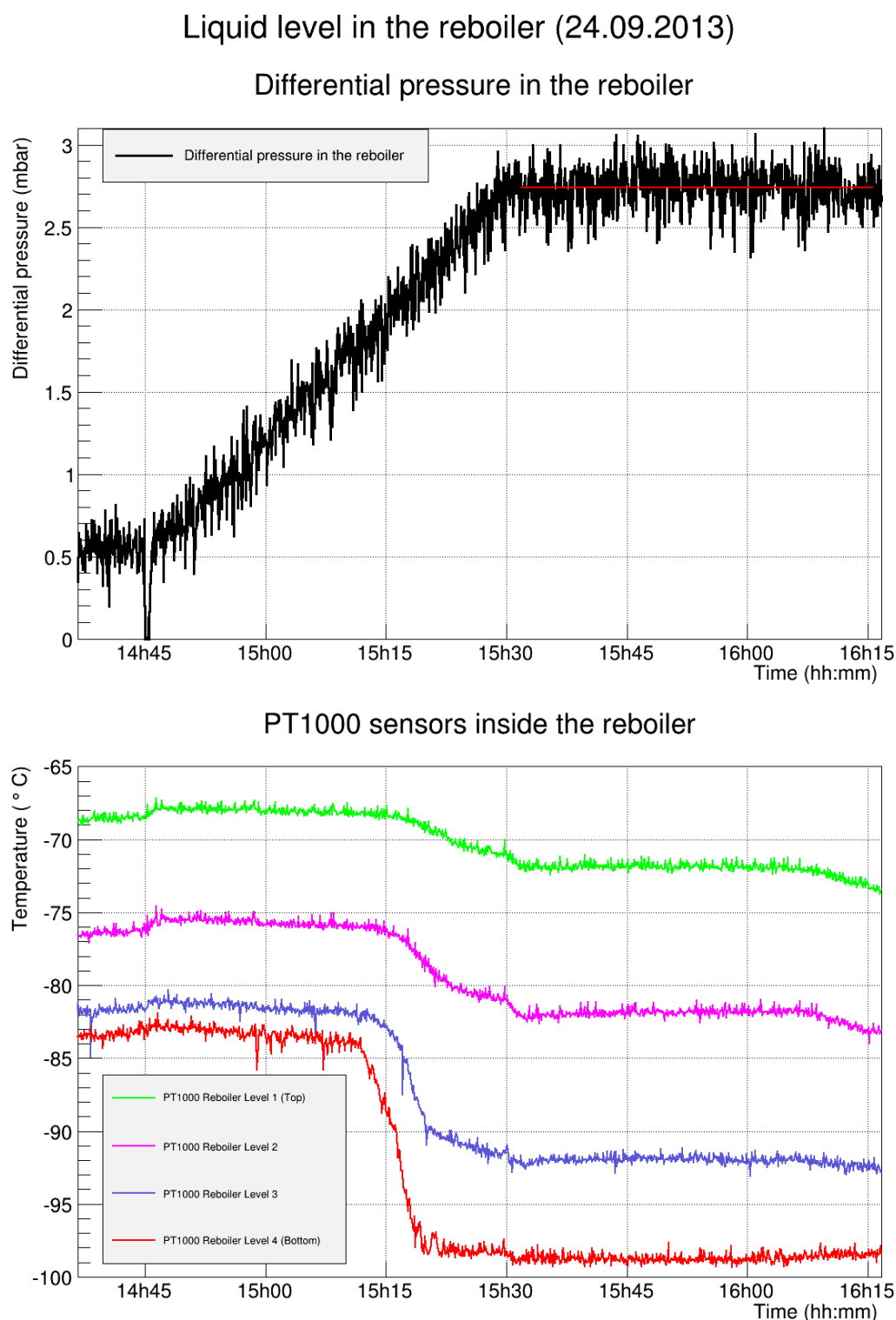
Figure 5.8: *Measurement of the liquid level inside the reboiler. In the top diagram, the determination of the liquid level using a differential pressure sensor is shown during a filling process. The pressure is rising and stays constant at 2.74 mbar that corresponds to a height of about 1 cm in the reboiler. As a cross check, a measurement of the four temperatures obtained by PT1000 sensors in the reboiler is shown. The lowest sensor (red) installed at a height of about 1 cm indicates that it is covered in liquid with a temperature at -98.68 °C, while the other sensors show higher temperatures and are thus covered by gaseous xenon. The two methods are in agreement and can be used for the determination of the liquid level in the reboiler.*

5.2 Middle part: packing tube
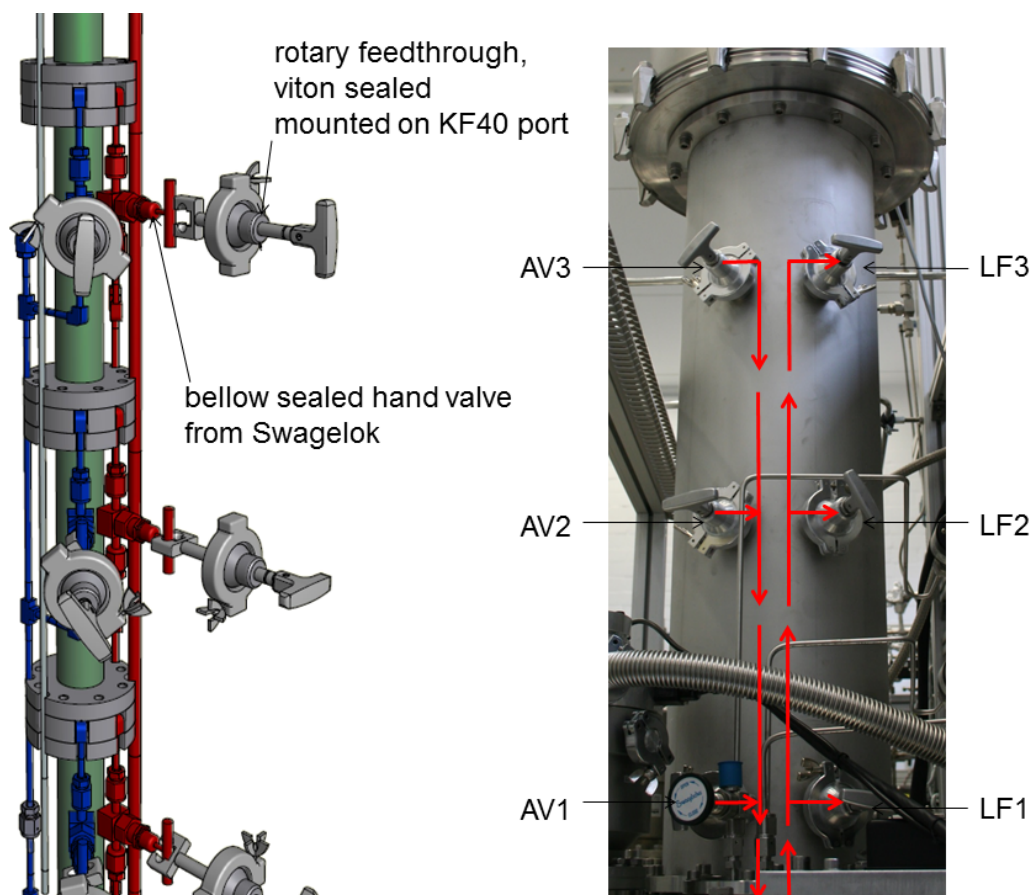
Figure 5.9: *On the left, a technical drawing of a segment of the packing tube is shown, along with the feed and diagnostic ports that can be opened and closed by bellow sealed hand valves using special forks. On the right, the middle part with the six valves from the outside is shown. The red arrows indicate the flow of the xenon inside the analysis line and feed line. The three Liquid Feeds (LF) as well as the Analysis Valves (AV) are labelled. Technical drawing done by C. Huhmann.*

The middle part basically consist of the packing tube itself, along with some additions. A heating belt is wrapped around the tube giving the possibility of a bakeout before starting the filling process. The column is housed in an insulation tube with a diameter of 259 mm and a height of 1000 mm. Along the column tube itself four pipes are installed: One pipe is guided to the very top and is used for the gaseous feed, another pipe connects the three possible liquid feed ports that are distributed over different heights to the preseparator. These feed ports can also be used as gaseous feeds. The third pipe connects three diagnostic ports to a port on top of the insulation vessel flange. This pipe is closed by a valve and can provide gas samples during the distillation process which can be analysed

online as described in 5.5.1. The last pipe connects the top part of the column with the reboiler in order to measure the differential pressure along the whole column with the differential pressure sensor 221B Baratron by MKS Instruments (Range of 100 mbar, resolution of ±0.01 % of full scale, ±0.5 % of reading accuracy).

All seven ports can be closed by specially-made cold valves. The gas feed valve was already introduced in section 6.2. The other six valves can be turned by stainless steel forks as shown in figure 5.6. In order to keep and stabilize the correct aligning of the valves and the forks during the distillation process at low temperatures, a stainless steel retainer was mounted to hold all six valves in the right spot.

The assembling of the packing tube is shown in the following.

5.2.1 Assembling of the column tube

The column tube was assembled in a special clean-room in order to avoid any contamination of the large surface of the packages. 5 pieces of packing material were put alternately twisted with 90° into every single tube with a diameter of 44.3 mm and a height of 300 mm using a Teflon rod as shown in figure 5.10. Afterwards, the four tubes were connected via special-made CF flanges that each have a feed and diagnostic port installed. The total column tube has a height of about 1200 mm containing 1000 mm packing material. The bottom part is later connected to the reboiler and the top part is connected to a bellow that is mounted to the top condenser.
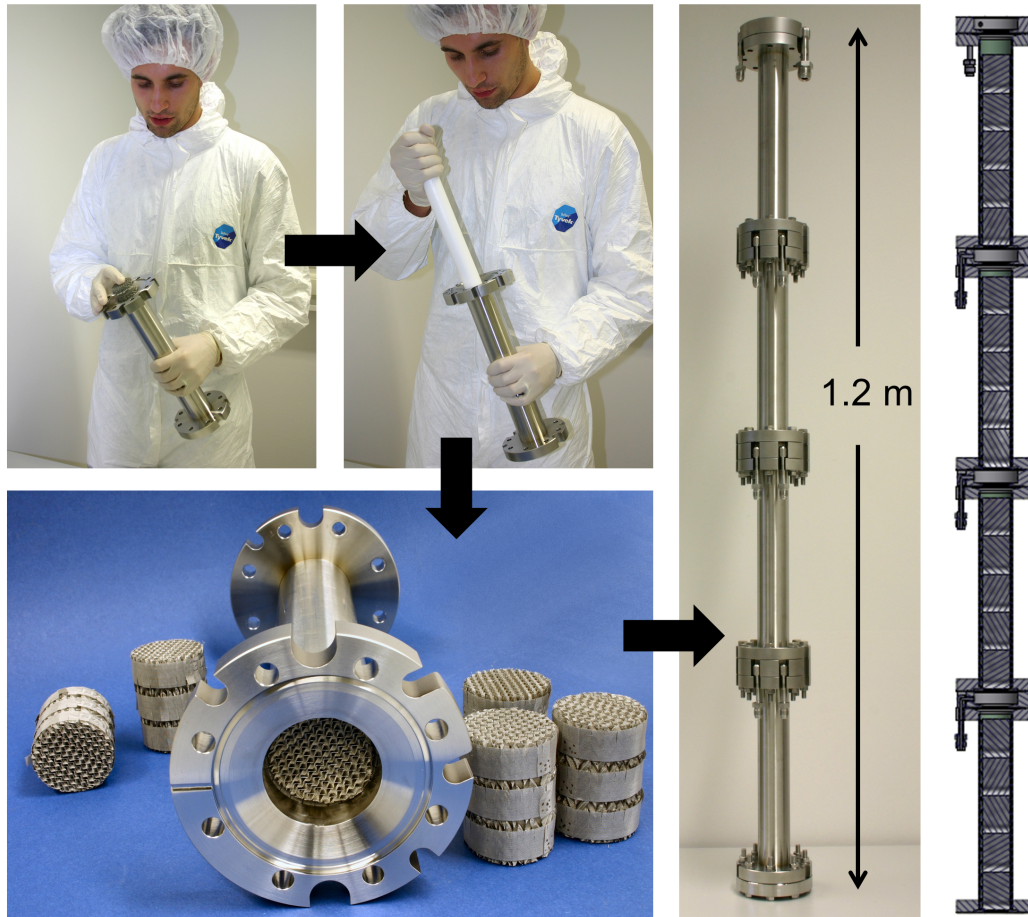
Figure 5.10: *The construction steps of the column tube are shown. In a clean room, 5 pieces of the packing material are pushed into one segment of the column using a Teflon bar. The four tubes are connected via special CF flanges that provide diagnostic and feed ports. The resulting column has a height of about 1.2 m and houses 1 m of packing material. A technical cross section of the assembled column is shown on the very right. Technical drawing done by C. Huhmann.*
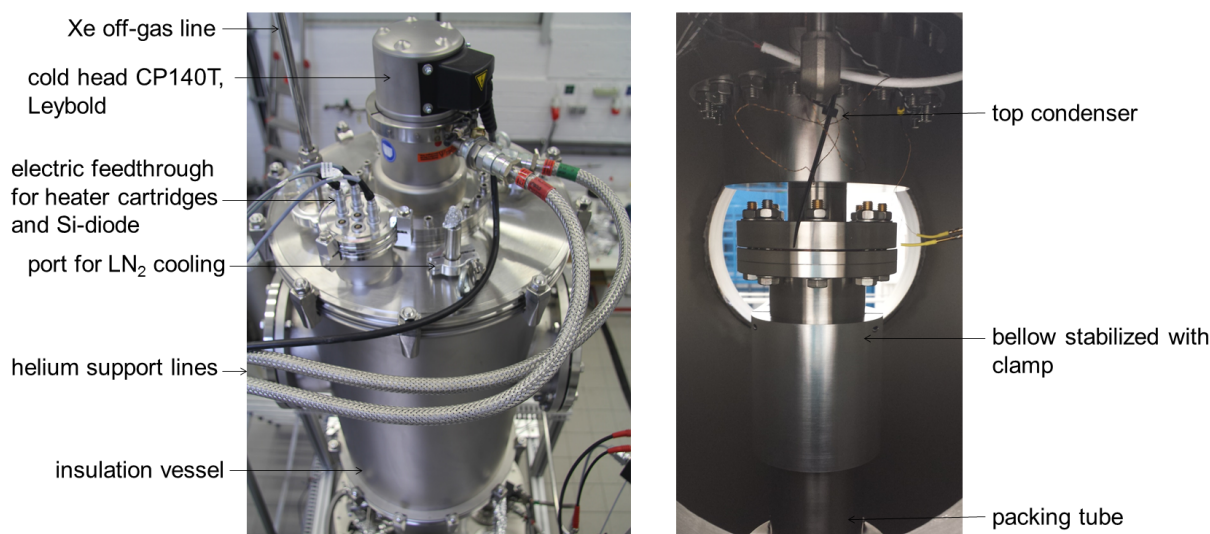
5.3 Top part: Top cooling tower

Figure 5.11: *On the left, a picture of the top of the column is shown. The coldhead CP140T is connected to two helium support lines. The flange provides feed-troughs for electric wires and the off-gas pipe as well as two ports for LN$_2$ cooling. On the right, the connection between the column tube and the condenser using a bellow that is stabilized by a clamp can be observed.*

The connection between the column tube and the top condenser is done by a stainless steel bellow with a flexible shaft that has a length of 65 mm and is designed for an operating pressure up to 3 bar. Additionally, it is covered by a clamp as shown in figure 5.11 for further stabilization. A bellow is used in order to compensate small differences of the height and position of the column tube compared to the position of the top condenser and to reduce the stress on the hardware that starts to deform and move slightly at the low operating temperatures.

The top part is surrounded by an insulation vessel with a diameter of 400 mm and a height of 700 mm that provides feed-throughs for electrical wires such as the heat cartridges and the Si-diode and for the off-gas pipe. This pipe also contains a rapture disk due to safety constraints with a maximal pressure allowance of 3.5 bar $\pm 10\,\%$. A picture of the top part is shown in figure 5.11. The design of the top cooling tower will be presented in the next subsection.

5.3.1 Top Condenser

The cooling tower of the top part is designed with the same principle as the preseparator and mainly differs in size and the used coldhead. The vessel is also funnel-shaped and has a diameter of 125 mm and a height of 66 mm, and the coldhead (CP140T, Leybold) provides a cooling power of $\sim$250 W at 178 K according to the company. In addition, both ends of a spiral copper pipe that covers the connection of the vessel with the coldhead as shown in figure 5.12 are guided through the top flange

to the outside. That gives the possibility of additional cooling by liquid nitrogen with a cooling power ~ 55 W/kg. This tool is currently under development and will not be presented further in this thesis. At the top of the vessel a port is installed for the extraction of the krypton-enriched xenon gas as off-gas.

For the monitoring of the temperature and the control of the cooling power, a Si-diode (DT-670D-DI, Lakeshore) is installed to the copper as well as two heat cartridges with a power of 300 W each. A schematic drawing, along with the assembled cooling tower, is shown in figure 5.12. The cooling power of the CP140T for different temperatures has been measured and will be presented in chapter 6.
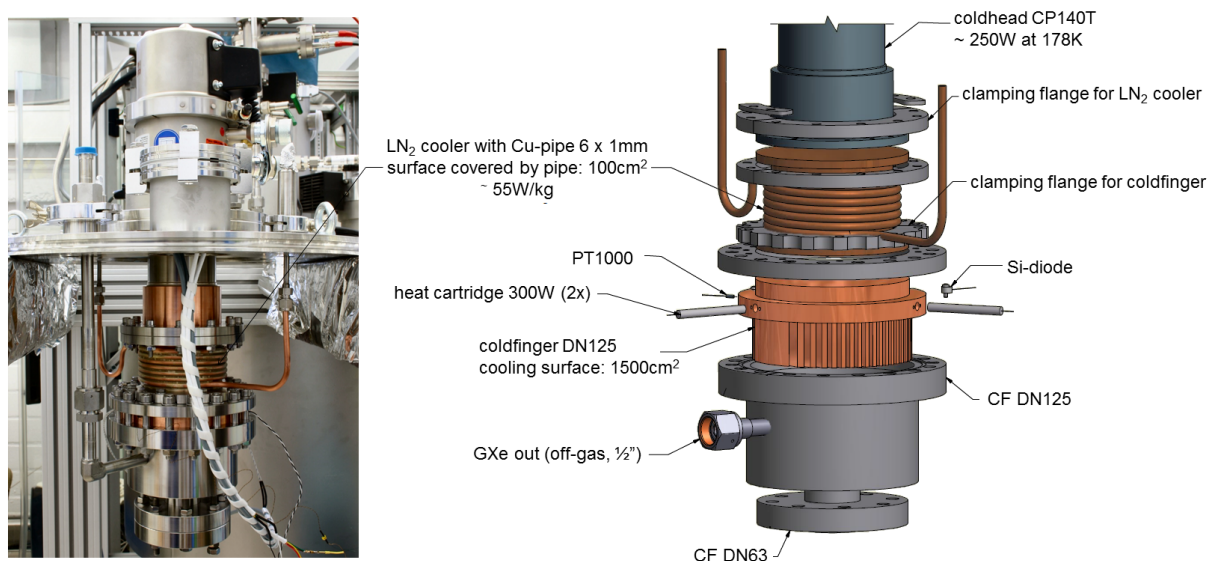
Figure 5.12: *On the right, a technical drawing of the top condenser is shown. The cooling tower is made of a vessel, a copper coldfinger and the coldhead CP140T. The vessel contains a port for the off-gas line and is connected to a bellow with a CF flange at the bottom. For temperature and cooling power control, a Si-diode as well as heat cartridges are applied to the copper. The possibility of extra cooling by LN_2 is given due to a spiral copper pipe that covers the connection between the copper and the coldhead. On the left, the assembled cooling tower mounted to the top flange of the column can be observed. Technical drawing done by C. Huhmann.*

5.4 Measurement and slowcontrol system

The whole set-up contains 27 parameters that are monitored as well as controlled by a LabVIEW based slowcontrol. A flowchart of all sensors and controllers are shown in figure 5.13. The installed sensors for temperature, pressure, flow, heating and insulation vacuum are presented in the following subsections.
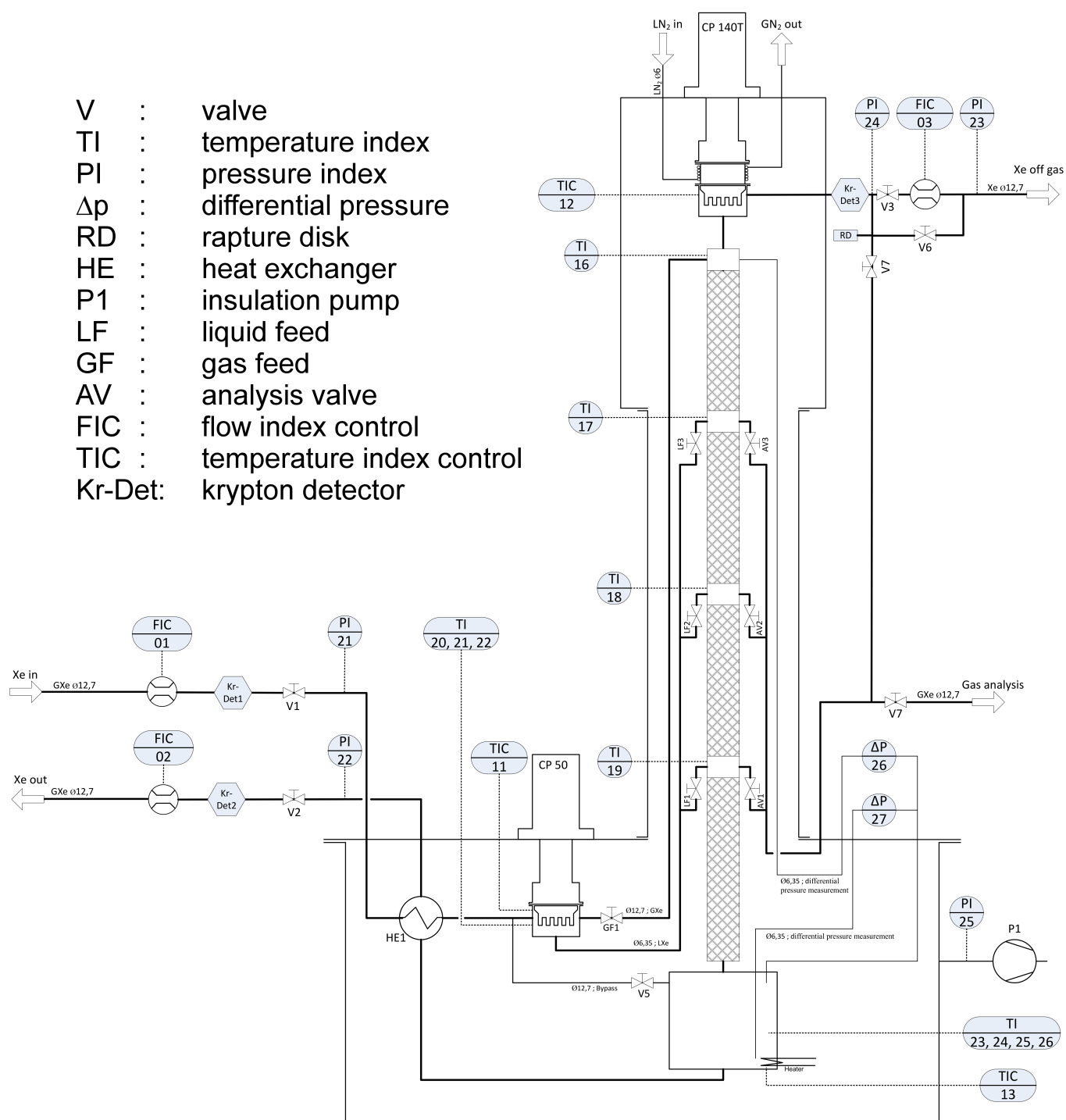
V   :   valve
TI   :   temperature index
PI   :   pressure index
Δp :   differential pressure
RD   :   rapture disk
HE   :   heat exchanger
P1   :   insulation pump
LF   :   liquid feed
GF   :   gas feed
AV   :   analysis valve
FIC   :   flow index control
TIC   :   temperature index control
Kr-Det: krypton detector

Figure 5.13: *Flowchart of the distillation column that indicates the location of the installed sensors and valves in the system. Drawing done by C.Huhmann.*

Measurement and control of the flows

Three flow controllers are used for the measurement and control of the input and output of the column. The xenon supply line is controlled by the flow controller 1479B from the company MKS Instruments (FIC01) at a maximum flow rate of 20 slpm (accuracy of 1 % of full scale, 1 % of reading). The same type of controller is installed to the return line (FIC02), containing the purified xenon. The off-gas line is also attached to the flow controller MKS 1479B (FIC03), but provides only a maximum flow rate of 0.1 slpm. The amount of xenon inside the system can be estimated with the integration of the input and output flows over time during the filling and distillation process.

Temperature sensors

Three Si-diodes are installed at the key components preseparator (TIC11), top condenser (TIC12) and reboiler (TIC13). Each location also hosts a PT1000 sensor installed as coverage, but not to be read-out at the moment. The silicon diodes are connected to a temperature controller (LakeShore 336), where the temperatures are measured with a four point measurement in order to reduce the noise picked up at the cables, on three different channels.

The remaining temperature sensors are PT1000 sensors. These are platinic measuring resistances that change their electric resistance depending on the environmental temperature. By introducing a constant current to the sensor, the change in the resistance can be translated into an analogue voltage using Ohm's law. The measured voltage can be translated back into the corresponding temperature using a LabvIEW based slowcontrol.

Four PT1000 sensors are installed to the column tube (TI16, TI17, TI18, TI19) in order to monitor the temperature distribution over the hole packing material.

Three PT1000 sensors are connected to the outside of the preseparator vessel (TI20, TI21, TI22) for the determination of the liquid level inside.

The liquid level of the reboiler is monitored by four PT1000 sensors (TI23, TI24, TI25, TI26) that are installed inside the vessel.

In total, 14 temperature sensors are distributed over the set-up.

Pressure sensors

The set-up possesses four absolute and two differential pressure sensors as well as a vacuum gauge for the measurement of the insulation vacuum.

The insulation vacuum is obtained by a PTR90 Penningvac from Leybold that is connected to a CenterOne measuring unit from the company Leybold.

The pressure inside the preseparator (PI21) and the reboiler (PI22) are measured with the same type of absolute pressure sensor (PTU Series UHP Transducer, Swagelok), which has a range of -1 bar to 9 bar giving a analogue output voltage between 0 V and 10 V. The pressure in the whole column tube (PI24) is obtained by a 121A Baratron sensor by MKS Instruments (Range 10 000 mbar, resolution of ±0.01 % of full scale, ±0.5 % of reading). Additionally, one sensor (PTU Series UHP Transducer, Swagelok) is used to monitor the pressure over the storage bottle for the krypton enriched off-gas (PI23).

With two differential pressure sensors (121A Baratron MKS, range 100 mbar, resolution of ±0.01 % of

full scale, $\pm0.5\,\%$ of reading), the pressure drop along the packing tube (ΔP26) as well as the liquid level inside the reboiler (ΔP27) are measured.

Measurement and control of the heating power

The heating power and thus the cooling power are controlled by different heat cartridges that are installed at the preseparator, top condenser and reboiler. As a result of heating and cooling, the temperatures and pressures in the different locations can be changed and controlled.

The preseparator contains a 100 W heat cartridge that is connected to the Lakeshore 336. The heating power is regulated on the temperature by defining a set-point. In order to converge to the set-point, a Proportional-Integral-Derivative (PID) circuit provided by the LakeShore is used and will be explained in section 5.4.1.

The segment consisting of the reboiler, the packing tube and the top condenser can be controlled separately from the preseparator. At the top, two heat cartridges connected in parallel with a resistance of $170\,\Omega$ each are installed to the condenser. These are connected to a controllable power supply (EA-PSI 8160-04R) that provides a heating power of 150 W for each heater, so that in total, a power of 300 W is available at this spot. The actual power is indicated on the display of the power supply and is determined by measuring the current and voltage flowing through the cartridge. In addition, the device is connected to the LakeShore 336 and can be controlled remotely by analogue voltages. At the bottom, 2$\times$2 cartridges, connected in parallel, are installed at the reboiler. Only two of them are used at the moment. As well as at the top, another EA power supply is used providing a total heating power of 300 W.

The column can be regulated and controlled in different modi:

If the system is regulated at the top and the bottom at the same time, it gets over-determined as a result and thus no stable distillation process can be achieved. Therefore, the system is either regulated at the top or at the bottom.

In the preseparator, the regulation depends on the defined temperature. Measurements and tests have shown, that a temperature regulation works well for the filling process of the column. Nevertheless, during distillation, a pressure regulation was more favourable. Several examples for the different options will be presented in chapter 6.

Each regulation option has its own PID-circuit that is provided by the LabVIEW based slowcontrol.

Processing of the measured signals

The LakeShore 336 is connected via an Ethernet cable to a micro-controller, the compactRIO-9074 from National Instruments (NI). As a result of that, the three silicon diodes, the heater of the preseparator, as well as both power supplies for the heating at the top and the bottom that are connected to the LakeShore can be controlled by the cRIO and thus by the LabVIEW based slowcontrol.

The cRIO contains two modules of the type NI-9205 (32 single-ended analogue input channels, 16 bit resolution, max. input range of $\pm10\,$V) and one module of the type NI-9263 (4 analogue output channels, 16 bit resolution, max. output of $\pm10\,$V). The remaining sensors, as described above, provide analogue voltage signals that are collected inside an electronic box, assembled at the electronic workshop in Muenster. The signals are forwarded from the box by two 37-pole cables to the cRIO and are connected to the modules NI-9205. The third module (NI-9263) provides an analogue output voltage
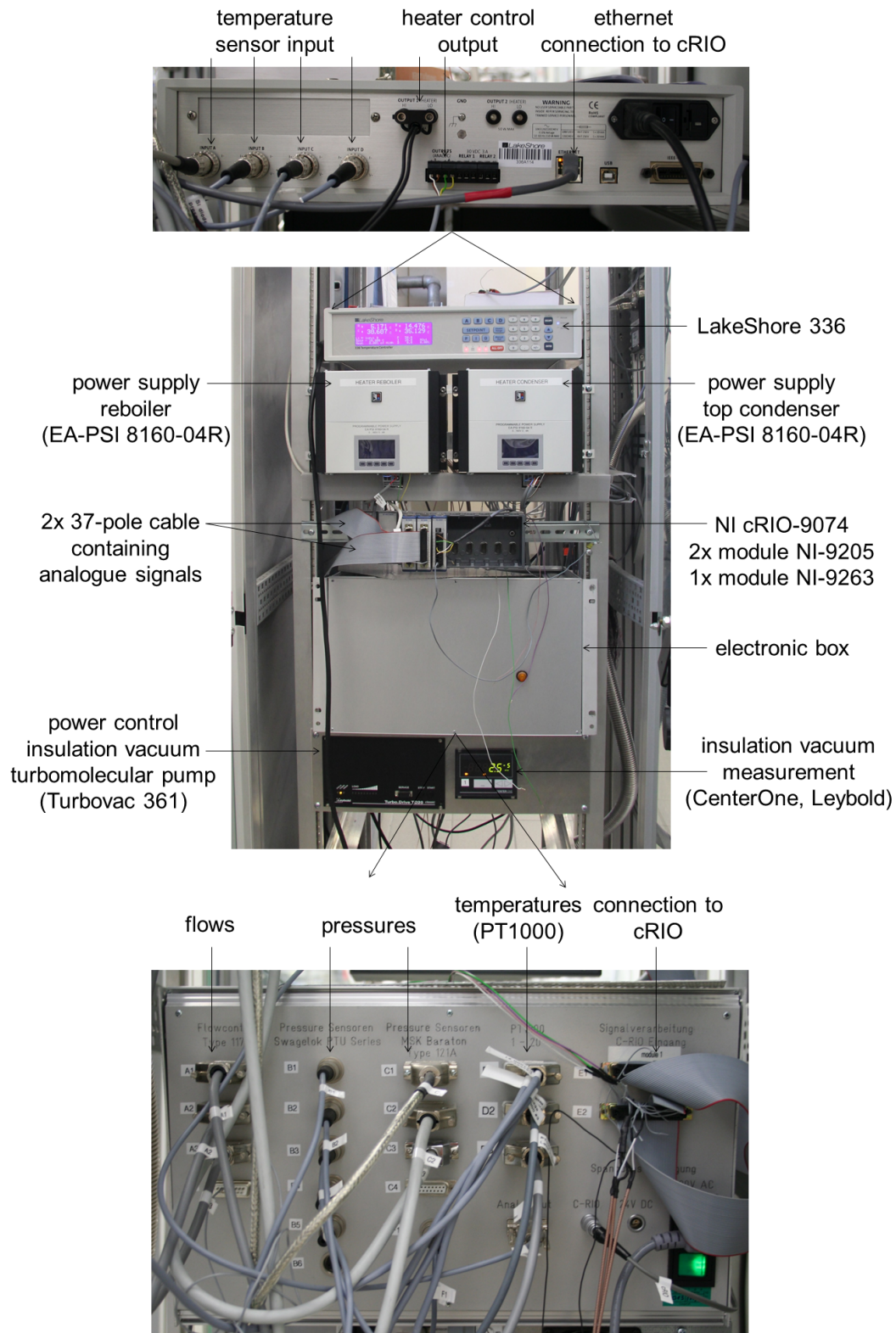
Figure 5.14: *A picture of the electronic rack for the distillation column is shown. Several temperature sensors as well as both power supplies for the heating at the top condenser and reboiler are connected to the LakeShore 336 (top). The device is connected to the cRIO-9074 from National Instrument. The analogue voltage signals from the remaining sensors are collected in the electronic box (bottom) and are also forwarded to the cRIO over two 37-pole cables. All signals are guided to the column computer (not in picture) and are processed by a LabVIEW based slowcontrol. At the bottom, the power control of the insulation turbo pump and the measuring unit for the insulation vacuum can be observed.*

of up to 10 V, controlling the three flow controllers.

The cRIO itself is connected via an Ethernet cable to the column-computer and the signals are processed by a LabVIEW based slowcontrol, as already mentioned. A picture of the front of the electronic rack is shown in figure 5.14. The slowcontrol of the system is presented in the following.

5.4.1 Labview based slowcontrol

The acquired signals from the cRIO are processed by a LabVIEW software. The measured voltages are translated into their corresponding variables, such as temperature, pressure, flow and heating and are displayed in the sorted manner in the front panel of the slowcontrol as shown in figure 5.15. Parameters that belong together are monitored on live-plots with a time window of 30 min. In addition, it is possible to scroll back and see the data from the last 3 h.

 Every regulation process in the system is controlled by its own Proportional-Integral-Derivative (PID) circuit. This kind of controller measures the difference between the actual value of a process variable and the defined set-point for this variable. In the case of the preseparator for example, the temperature measured by the silicon diode is the process variable. Depending on the calculated error value, the PID controller changes the control variable, in this case the heating power. The P-value of the circuit reacts to the present error, the I-value regards the accumulation of past errors and the D-value is a prediction on future errors. A fast convergence to the set-point and a stable operation afterwards can be optimized by choosing the right values for the PID circuit. That optimization is not trivial, and can be done by an educated trial and error process observing the response of the controller for different set-points and values. The circuit for the preseparator is provided by the LakeShore 336, while the remaining PID-controllers are programmed by the LabVIEW slowcontrol.

As already mentioned, the regulation for the distillation process can be split into temperature regulation and pressure regulation as shown in figure 5.16. In both cases the preseperator is regulated by the temperature measured by its silicon diode. The different options are explained in the following.

Temperature regulation

On the left side of figure 5.16, the temperature regulation is shown. The process variable in this modus is given by the temperature at the top condenser measured by the Si-diode at the top. The set-point can be typed into the box "Setpoint Top Condenser [°C]" and the set-point for the preseparator is given by "Setpoint Presep [°C]". Depending on the modus, either the heater cartridges at the top condenser are used as control variable, while the heater at the bottom can be controlled manually (Regulation Top) or vice versa (Regulation Bottom).

The input and output flows can be controlled as well.

Pressure regulation

The process variable in this modus is given by the pressure inside the column tube, indicated as "Setpoint pressure in column [bar]", as shown on the right side of figure 5.16. The set-point for the preseparator stays the same, visible as "Setpoint Presep [°C]". As for the temperature regulation, either the heater cartridges at the top condenser are used as a control variable, while the heater at the bottom can be controlled manually (Regulation Top) or vice versa (Regulation Bottom). In addition,
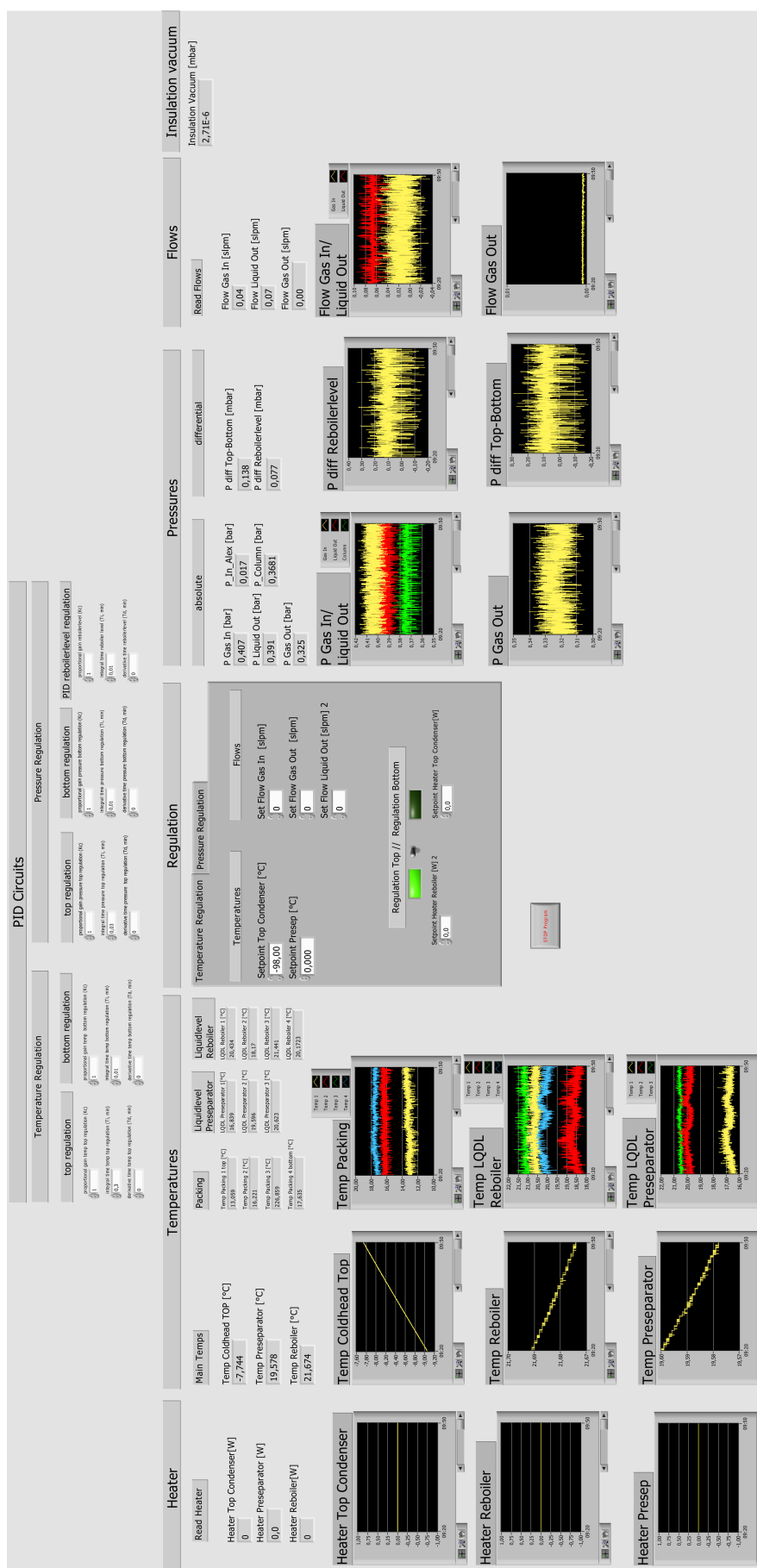
Figure 5.15: *Front panel of the LabVIEW based slowcontrol.*

Figure 5.16: *The temperature regulation (left), using the temperature measured by the silicon diode at the top as process variable, and the pressure regulation (right), using the pressure inside the column tube as process variable, are shown. In both cases, the control variable is either given by the heat cartridges at the top (Regulation Top), while the heater at the bottom can be controlled manually, or vice versa (Regulation Bottom). In both cases, all three flows can be controlled as well as the temperature in the preseparator. In addition, an automated regulation for the liquid level in the reboiler was implemented for pressure regulation.*

an automated regulation for the liquid level in the reboiler, indicated as "Reboilerlevel", depending on the differential pressure in the reboiler as process variable, was implemented, but has not been tested yet. Therefore, the regulation is done manually by the flow controller "Liquid Out" at the moment. The other two flow controllers for the "Gas In" and "Gas Out" can be controlled as well.

In order to avoid accidents, the main key variables, such as the pressure and temperature in the column tube, are monitored over 24 h a day by a second LabVIEW program (savedata.vi). If one value is outside a user defined range, an SMS alarm as well as an email alarm containing the crucial values is sent to the XENON group members of Muenster in order to alert them. Furthermore, the program sends a status mail of the key variables to all members three times a day. A picture of the front panel of these program as well as the alarm variable list are shown in figure 5.17. All variables are connected to a time-stamp and stored into a txt-file by this program as well.
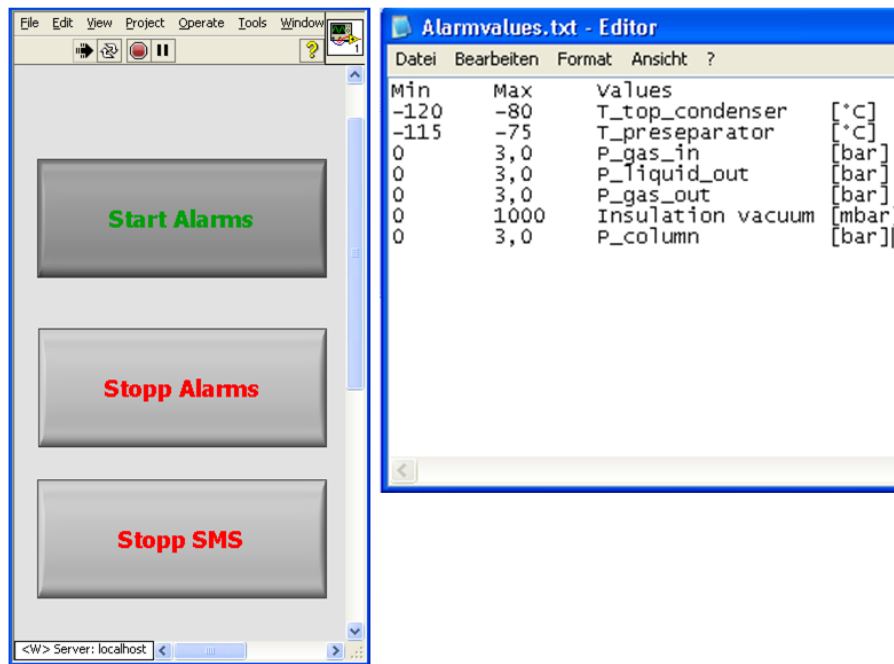
Figure 5.17: *On the left, the front panel of the LabVIEW observation program is shown. It's possible to start and stop the alarms. In the case of an alarm, it can be stopped by pressing the button "Stop SMS". The allowed ranges of the crucial variables can be set in the txt-file for the alarm values, shown on the right, which is read by the observation program. All measured variables of the system are stored into a txt-file, while this program is running.*

5.5 Diagnostic tools for the determination of the separation efficiency

In order to estimate the separation efficiency of the distillation column, two major diagnostic tools are currently under development in Muenster. The first one is a residual gas analyser (RGA) combined with a cold trap, measuring absolute krypton concentrations in the xenon gas, while the other one uses a ^{83m}Kr-doping method. Both tools will be briefly presented in the following subsections.

5.5.1 RGA with cold trap

Measuring low concentrations of krypton in xenon at the ppb to sub-ppb regime is not possible with common RGAs, since they are working only at pressures up to 10^{-5} mbar with a sensitivity for partial pressures down to 10^{-14} mbar at optimized conditions. Thus, a method using a liquid nitrogen trap combined with a custom-made valve has been developed.

At a temperature of 77 K, the concentration of the dominant gas species xenon is reduced due to the concept of vapour pressure that is determined to be P^0_{Xe}=2.5 × 10^{-3} mbar for xenon and P^0_{Kr}=2.0 mbar for krypton according to [Bro13]. As a result, a bulk of xenon is frozen out in the trap, while krypton can pass nearly unattached and can be measured by the RGA at a temporarily reduced pumping speed. With this set-up, a sensitivity of 40 ppt has been reached and an ultra pure gas sample from

the company Air Liquide was investigated. The unknown concentration of krypton in xenon was determined to be (330 ± 200) ppt for this sample [Bro13].

This method can be used to measure the absolute concentration of the gaseous input flow, the krypton-enriched off-gas and to some extent the distilled xenon gas. A schematic drawing of the set-up is shown in figure 5.18. More details can be found in [Bro13].
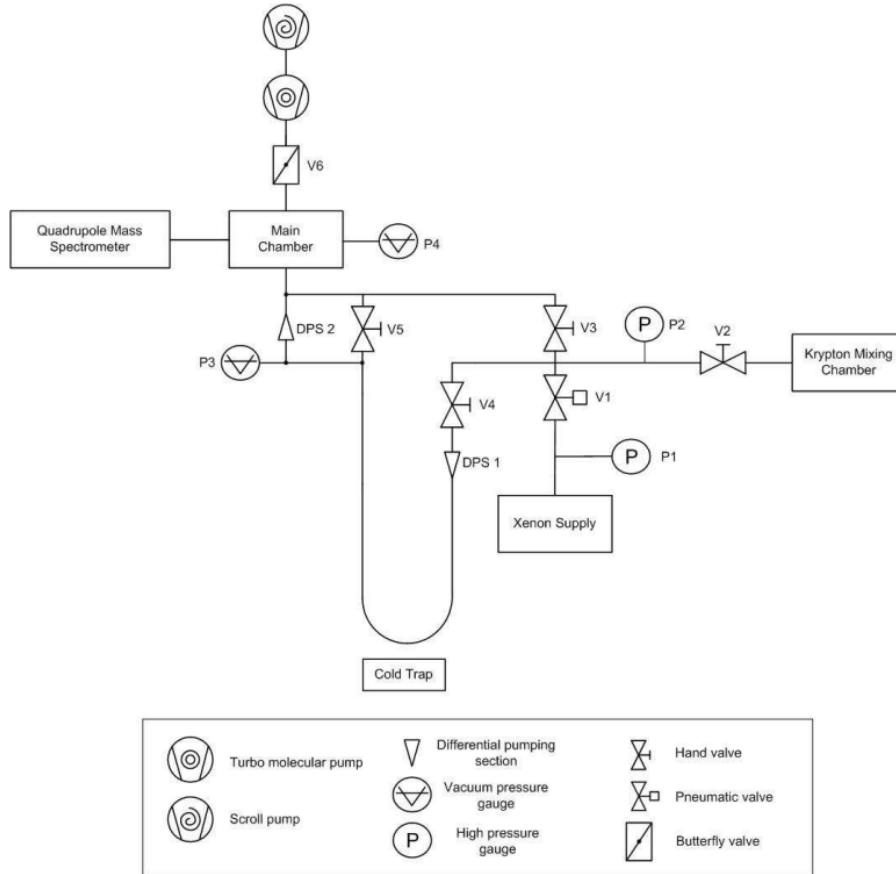

Figure 5.18: *Schematic drawing of the set-up for the measurement of absolute concentrations of krypton in xenon down to the ppt-level using a RGA in combination with a liquid nitrogen cold trap [Bro13].*

5.5.2 ^{83m}Kr tracer method

The second tool is a radioactive tracer method, using a ^{83}Rb-source that provides ^{83m}Kr. The radioactive krypton decays in two steps into its ground state ^{83}Kr, which is stable, with half lifes of 1.83 h and 154.4 ns, emitting conversion electrons and gammas with energies of 32.15 keV and 9.4 keV, respectively. A decay scheme of this process is shown in figure 5.19.

The source is inserted into the xenon supply line of the distillation column and can be opened and closed by a hand valve, giving the possibility of doping the feed gas. The radioactive ^{83}Rb with a half
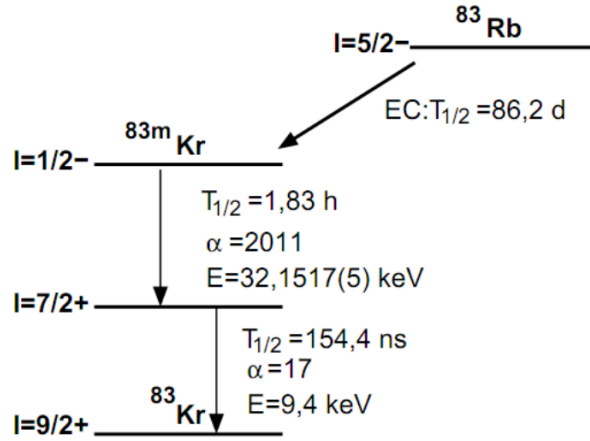
Figure 5.19: *Decay scheme of* ^{83}Rb *[Ost08].*

life of 86.2 d is bound in zeolite beads in order to hinder the rubidium from entering the supply line and thus to avoid a radioactive contamination of the xenon gas, while the krypton can leave the source unattached. Due to the very low doping concentration in the range of $\sim 10^{-16}$, the short half life of 1.83 h and the stable decay product, the xenon is only contaminated by very low concentrations of the stable ^{83}Kr, which is not crucial. Detailed information about such a source is shown in [Han11].

During the doping, the gaseous xenon is excited by the emitted electrons from the decay of ^{83m}Kr and produces scintillation light at a wavelength of 172 nm as a result [Mon07]. As already explained, xenon is transparent for its own light and thus the scintillation, which is proportional to the doped concentration, can be measured with the same type of PMT as used for the XENON100 detector. The photo sensitive detector is housed in a stainless steel T-piece as shown in figure 5.20. For further enhancement of the light yield, a PTFE foil is fixed inside the tube. Several tests about the reflectivity of PTFE for gaseous as well as liquid xenon have been investigated in Muenster and will be presented in [Lev14].

Due to the fact that the doped ^{83m}Kr has the same chemical properties as the ^{85}Kr and will behave identically in the distillation process as consequence, three of these so-called ^{83m}Kr-monitors have been assembled in Muenster and have been installed to the input line, the off-gas line, as well as the return line as shown in figure 5.21 for the off-gas line.

With the comparison between the measured rates in the input and both outputs relative to each other, an estimation of the separation efficiency can be made. In order to ensure the possibility of comparing the different rates, a normalization by the prevail flows and pressures during the process as well as a calibration beforehand have to be done. A first measurement during distillation without calibration will be shown in chapter 6. This method is currently under development and will be presented in more detail in [Ros14].

After the assembling of the cryogenic distillation column was completed, first distillation tests have been done and will be presented in the next chapter.
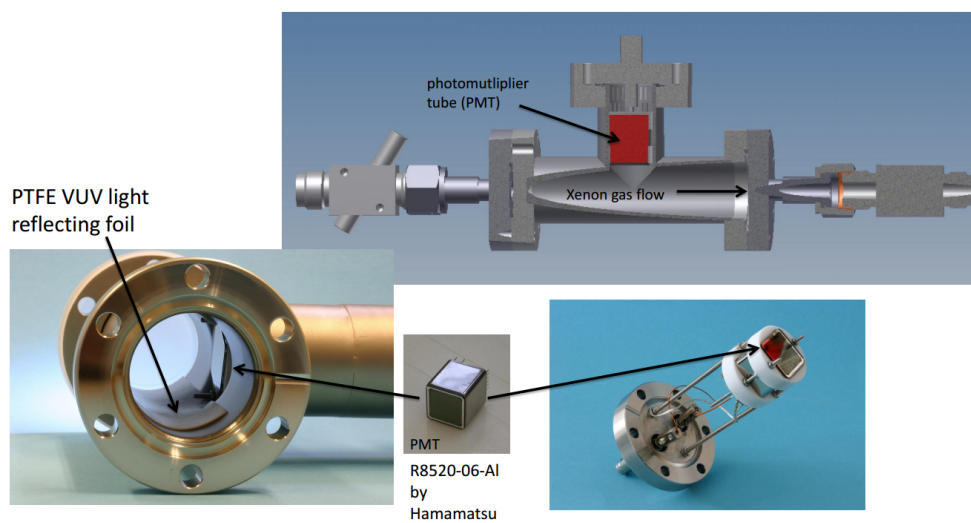
Figure 5.20: *Set-up of a ^{83m}Kr-monitor. A schematic drawing as well as pictures during the assembling are shown.*
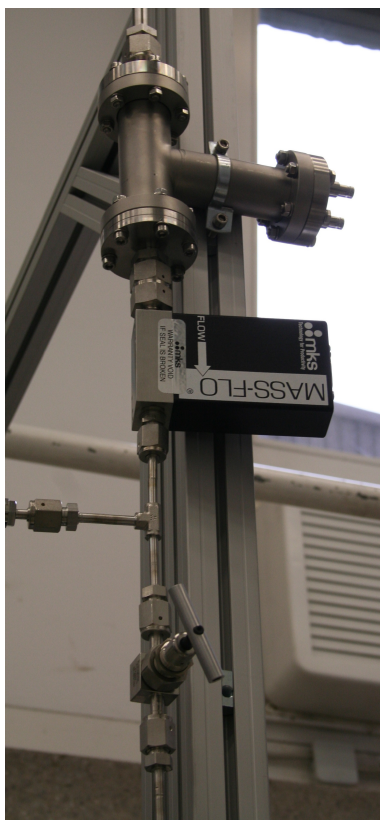

Figure 5.21: *Installation of one ^{83m}Kr-detector to the off-gas line.*

6 First tests of the cryogenic distillation column in Muenster

After the final construction of the column, the different sensors of the system and the slowcontrol have been tested. It was pumped down and baked at about $100\,°C$ in order to reduce contaminations from the walls. After that, a cooling power test of the cold head CP140T at the top condenser has been done with the evacuated system and will be presented in this chapter. Furthermore, reproducibility measurements with the gas feed valve (GF1) have been taken and will be shown as well.

The filling process of the distillation column will be explained, followed by first distillation tests with a bottom regulated pressure mode. At the end of this chapter, a short outlook on the determination of the separation efficiency will be given.

All measurements, shown in this chapter, have been taken in cooperation with Stephan Rosendahl, who may use different aspects of the results in his upcoming PhD-thesis as well.

6.1 Cooling power of the coldhead CP140T

The cooling power at the top condenser is a key parameter in order to allow a stable operation and a successful distillation process. According to the calculation in section 4.4, $150\,W$ are required for the liquefaction of the up-coming xenon that is fed back to the column tube.

In figure 6.1 a cooling power diagram of the coldhead CP140T provided by Leybold is shown. The COOLPOWER 140T has a cooling power of $150\,W$ at a temperature of $80\,K$ and about $180\,W$ at a temperature of $100\,K$, according to the diagram in figure 6.1. Unfortunately, the temperature range for the distillation process between $163\,K$ and $183\,K$ is not specified in more detail by the company and therefore is rather unknown. Thus, the cooling power at a temperature of $178\,K$ was roughly estimated, using the existing data, to be around $250\,W$.

A cool down test with the evacuated system has been done in order to verify this value and will be presented in this section.

The inside of the column was evacuated to a level of $3.0 \times 10^{-7}\,mbar$, using a dry magnetic bearing turbo pump from the Muenster gas system, and an insulation vacuum of $1.3 \times 10^{-6}\,mbar$ was applied to the system. In consequence, the net cooling power at the top equals the heating power that is needed to keep the system at a defined temperature, provided by the installed heat cartridges. A measurement of the heating power, and thus the cooling power, at different temperature set-points has been done and is shown in figure 6.2. At a temperature of $80\,K$ and of $100\,K$ the cooling power can estimated from the measured diagram to be about $(125 \pm 5)\,W$ and $(95 \pm 5)\,W$, respectively. The comparison between these numbers and the provided values by Leybold gives a difference of about $(55 \pm 5)\,W$ in both cases. Thus, the original cooling power can be determined to be around $(260 \pm 8)\,W$ at the operating temperature of $178\,K$, adding a heat loss of $(55 \pm 5)\,W$ to the measured cooling power of
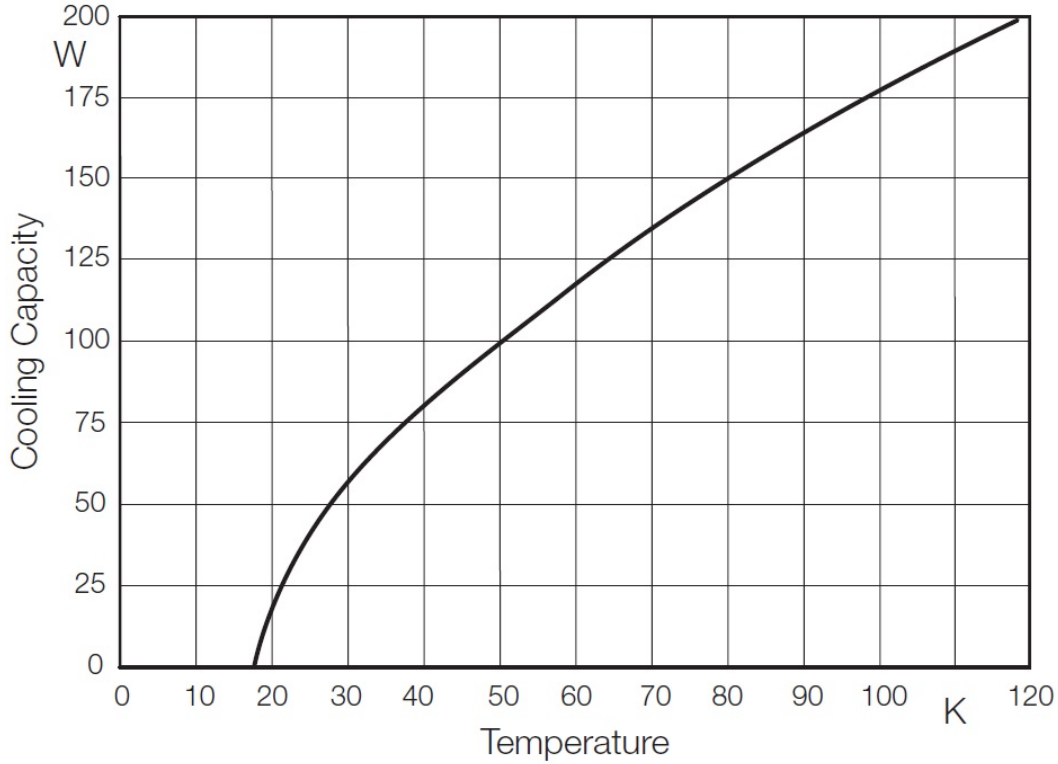
Figure 6.1: *Cooling power against temperature set-points of the CP140T provided by Leybold. The operation regime of the distillation process between 163 K and 183 K has not been specified by the company. Diagram taken from [Ley].*

(205 ± 3) W.

Due to the design of the construction, different heat loads at this location are expected.

In a first step, the heat radiation ($\dot{Q}_{rad}$) between the surface of the cold top condenser (A_c) and the warm insulation vessel (A_w) can be estimated, according to [Hae81], with the Stefan-Boltzmann law

$$\dot{Q}_{rad} = f \cdot e_c \cdot A_c \cdot \sigma \cdot \left(T_w^4 - T_c^4\right), \tag{6.1}$$

using the emissivity e_c of the cold surface A_c, the Stefan-Boltzmann constant σ, the temperature of the insulation vessel T_w and of the cold top condenser T_c, and the geometry and emissivity dependence f that is given by:

$$f = \frac{1}{1 + A_c \cdot e_c(e_w^{-1} - 1)/A_w}. \tag{6.2}$$

For the estimation, it was assumed that the cooling tower consists only of stainless steel and is on average a cylindrical vessel with a diameter of 65 mm and a height of 350 mm. Neglecting the copper is not crucial, because its emissivity is a factor 10 lower in comparison to stainless steel. In consequence, the calculated heat radiation can be seen as the upper limit. The emissivity e_c was chosen conservatively to be 0.15 [Hae81]. The emissivity e_w of the covering part of the insulation vessel, which is made of
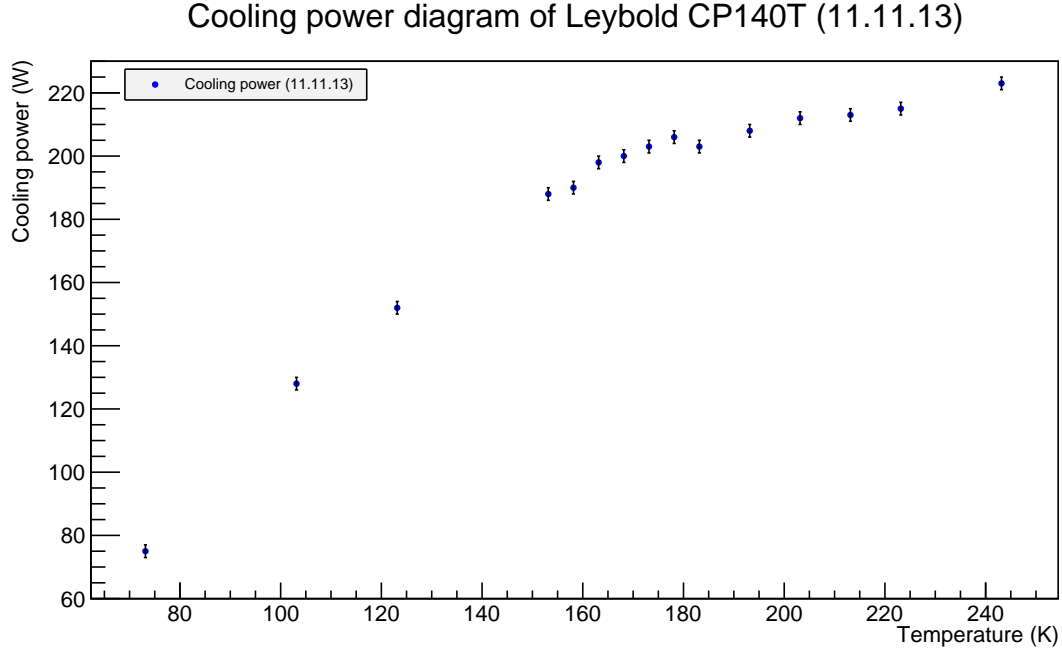
Figure 6.2: *The cooling power of the top cooling tower for different temperature set-points measured at the copper coldfinger. The cooling power equals the measured heating power that is required to keep the defined temperature in the evacuated system. In the operating regime between 163 K and 183 K the cooling power was measured to be around 200 W. The errorbars of the temperatures are smaller than the symbols. The errorbars of the cooling power were estimated by the fluctuations shown on the display of the used power supply.*

stainless steel and has a diameter of 400 mm and a height of 350 mm, is the same as for the top condenser. With that, f can be calculated:

$$f = \frac{1}{1 + 0.14\,\mathrm{m}^2 \cdot 0.15 \cdot (0.15^{-1} - 1)/0.44\,\mathrm{m}^2} = 0.78 \tag{6.3}$$

With $\sigma = 5.67 \times 10^{-8}\,\mathrm{W/m^2K^4}$, the temperature $T_w = 300\,\mathrm{K}$, and the temperature $T_c = 178\,\mathrm{K}$, the heat radiation can be obtained:

$$\dot{Q}_{rad} = 0.78 \cdot 0.15 \cdot 0.14\,\mathrm{m}^2 \cdot 5.67 \cdot 10^{-8}\,\mathrm{W/m^2K^4} \cdot \left((300\,\mathrm{K})^4 - (178\,\mathrm{K})^4\right) = 6.78\,\mathrm{W} \approx 7\,\mathrm{W} \tag{6.4}$$

The heat radiation has an impact of 7 W to the cooling power of the coldhead.
Another influence is given by the bellow that connects the bottom of the top condenser with the packing tube. According to [Hae81], the heat transfer can be calculated with

$$\dot{Q}_{Bellow} = \frac{A}{L} \int_{T_1}^{T_2} \lambda(T)\,\mathrm{d}T, \tag{6.5}$$

using the cross section A=4.27×10^{-4} m^2 of the connection between the bellow and the top condenser, the length L=0.273 m of the bellow and the thermal conductivity $\lambda(T)$ of stainless steel. Taking the values for the integral from [Hae81], the heat load for a temperature of 178 K at the top condenser and a temperature of 300 K at the end of the bellow, measured by the top PT1000 (TI16), is determined to be:

$$\dot{Q}_{Bellow} = \frac{4.27 \cdot 10^{-4}\,\mathrm{m}^2}{0.273\,\mathrm{m}} \cdot \left(3060\,\mathrm{W/m} - 1170\,\mathrm{W/m}\right) = 2.96\,\mathrm{W} \approx 3\,\mathrm{W} \tag{6.6}$$

Adding this number to the heat radiation, a heat loss of about 10 W can be explained. The loss of the remaining 45 W are unknown at the moment. Possible explanations can be the heat transfer over the electrical wiring, the liquid nitrogen copper line, that is filled with air and connected to the outside, as well as the properties of the assembling of the coldhead to the top flange of the column. This has to be investigated in more detail.

However, the required 150 W for the distillation process can be provided by the CP140T over the operation range between 163 K and 183 K as shown in figure 6.2.

6.2 Conductance measurement of gas feed valve

In this part, measurements of the reproducibility of the gas feed valve (GF1) depending on the different positions will be presented. The read-out as well as the repeatability of the different positions of the valve, depending on the changes in the resistance of the potentiometer, have been tested at different flows. In order to compare the different measurements, the conductance L can be determined as a first step to be:

$$L = \frac{\bar{F}}{\Delta P}, \tag{6.7}$$

using the flow in the system and the difference in pressure before and after the valve [Pfe10].

The system was filled with around 1.1 bar of gaseous xenon and all lines had been closed, except for the supply line (open V1), the return line from the reboiler (open V2) and the gas feed valve (GF1). In a second step, the xenon was circulated through the gas feed valve using the Muenster gas system at a fixed flow given by the input flow controller (FIC01). The output controller (FIC02) was fully opened and thus turned into a flowmeter. Consequently, the flow before and after the gas feed valve could be established. After a few minutes of circulation, the flow in the system was almost identical at each location, so it is given by:

$$\bar{F} = \frac{F_{FIC01} + F_{FIC02}}{2} \tag{6.8}$$

The pressure before (P_{GI}: PI21) and after (P_{LO}: PI22) the valve is measured by pressure sensors. The difference ΔP can be calculated with these values.

Equation 6.7 is valid for a molecular flow in the system, but during measurements at 5 slpm and even 10 slpm with gaseous xenon, the flow is laminar or could even be turbulent. Thus, the conductance L has to be normalized by pressure and depends upon a specific geometric factor given by the construction of the valve, called geometric conductance (L_{geo}) in this case, that is rather unknown:

$$L = L_{geo} \cdot (P_{GI} + P_{LO}) \quad [\text{Pfe10}] \tag{6.9}$$

Using this equation it is possible to obtain the geometric conductance, which has a unit of $l\,s^{-1}\,bar^{-1}$. It should be independent from the pressures and flows in the system and should be reproducible for same valve positions at different flows and pressures. It was calculated from:

$$L_{geo} = \frac{L}{P_{GI} + P_{LO}} \tag{6.10}$$

Before the tests, the offsets of the pressure sensors were measured at the evacuated system and have been taken into account for the calculations. The uncertainties of the measured signals are dominated by the accuracy of the sensors. The statistical uncertainties as well as the accuracy of the measuring unit of the cRIO with a resolution of 16 bit are a factor 20 and two orders of magnitude lower, respectively. Therefore they have been neglected and a Gaussian propagation of uncertainty have been done using the systematic errors of the different sensors.

The actual position of the valve can be procured by measuring the resistance of the potentiometer using a multimeter (METRAHIT One) with an accuracy of $\pm 0.1\,\Omega$. The fully opened position corresponds to a resistance of $727\,\Omega$ and the closed position to $36\,\Omega$. With that, a translation into a percentage regime can be done by:

$$\text{position}_\% = (\text{position}_\Omega - 36\,\Omega) \cdot \frac{100\,\%}{691\,\Omega} \tag{6.11}$$

In figure 6.3, a geometric conductance measurement over the full range at a flow of 5 slpm (Measurement 1) is shown. Following this measurement, the valve was closed step by step starting at 100 %. The geometric factor stays almost the same at $(6.47 \pm 0.01)\,l\,s^{-1}\,bar^{-1}$ over the range between 40 % and 100 %, starting to fall for smaller positions. During the distillation process, the gas feed will only make up a small fraction of the total feed, and therefore the last 10 % of the range are of the highest interest. In total, two measurements at a flow of 5 slpm and two measurements at a flow of 10 slpm have been done for this region and are presented in figure 6.4 and 6.5 (Measurement 2-4). The two figures differ in the starting position of the valve. In the first figure, the valve was turned from an open to a closed position, while in the second figure, the valve was turned from the closed position to an open one.

It can observed that for the different starting positions, the calculated values are slightly different. Due to the construction, it is not possible to move the valve with a high accuracy from the closed position, because it is slightly stucked and cannot be moved smoothly. Therefore, it's advisable to start the adjustment of a certain position from a more opened position to allow reproducibility.

The comparison of the values in figure 6.4 shows that for a fixed flow and pressure the geometric factor can be reproduced very well. The two measurements at 10 slpm (pink and black) are almost congruent. Nevertheless, the comparison between the two different flows and thus pressures gives about a factor 2 difference for the geometric factor at different positions. This discovery is an indication that the obtained geometric factor is dependent upon the flow and pressure against the assumption above.

One possible explanation could be, that the prevail regime in the system is not laminar, but turbulent. The type can be determined by the estimation of the Reynolds number for the two different flows using:

$$Re = \frac{\rho \cdot v \cdot d}{\eta} \quad \text{[Pfe10]} \tag{6.12}$$

According to [NIST], the gaseous xenon has a density of ρ=5.96 kg/m^3 and a dynamic viscosity of η=2.26 × 10^{-5} kg/s m for a temperature of 20 °C and a pressure of 1.1 bar. The fully opened valve
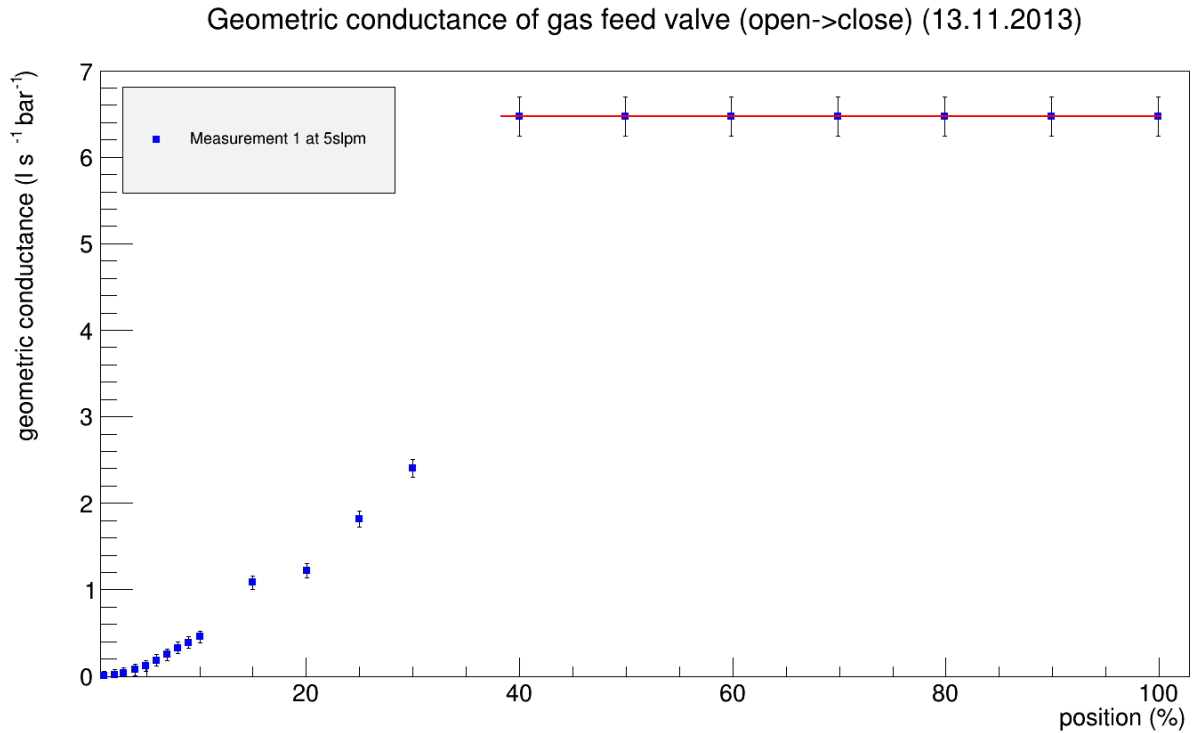
Figure 6.3: *Geometric conductance measurement at two different flows for the full range. The valve started at 100 % and was closed step by step. Over the range down to 40 % the geometric conductance is constant at 6.47 l/s bar. Afterwards it started to decrease.*

correspond to a quarter inch line and thus has a inner diameter of d=0.004 57 mm. The velocity v can be obtained by the flow and the cross section A of the through-flow. The normalized flow has to be translated from slpm into l/s beforehand using the following equation:

$$F(\text{l/s}) = F(\text{slpm}) \cdot \frac{293\,\text{K} \cdot 1.013\,\text{bar}}{273\,\text{K} \cdot p(\text{bar}) \cdot 60} \tag{6.13}$$

The value $p(bar)$ gives the actual absolute pressure in the system and is slightly different at 5 slpm and 10 slpm. With that, the velocity can be calculated from:

$$v = \frac{F(\text{l/s})}{A} \tag{6.14}$$

5 slpm correspond to a velocity of v_5=4.88 m/s and 10 slpm correspond to a velocity of v_{10}=9.39 m/s. Using equation 6.12, the two Reynolds numbers are:

$$Re(5\,\text{slpm}) = 5873 \quad \text{and} \quad Re(10\,\text{slpm}) = 11\,300 \tag{6.15}$$

The Reynolds numbers, assuming a cold xenon gas at an operation temperature of $-98\,°$C, can be calculated in addition for the prevail flows and pressures. Due to the change of the temperature,
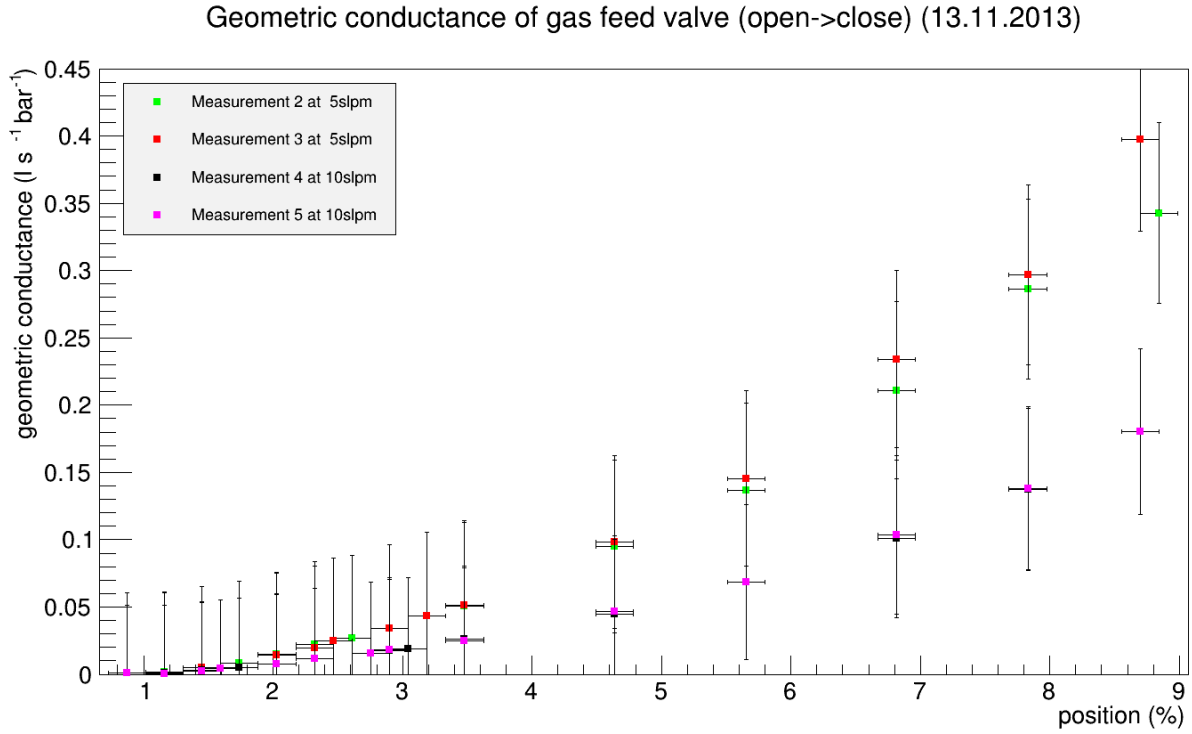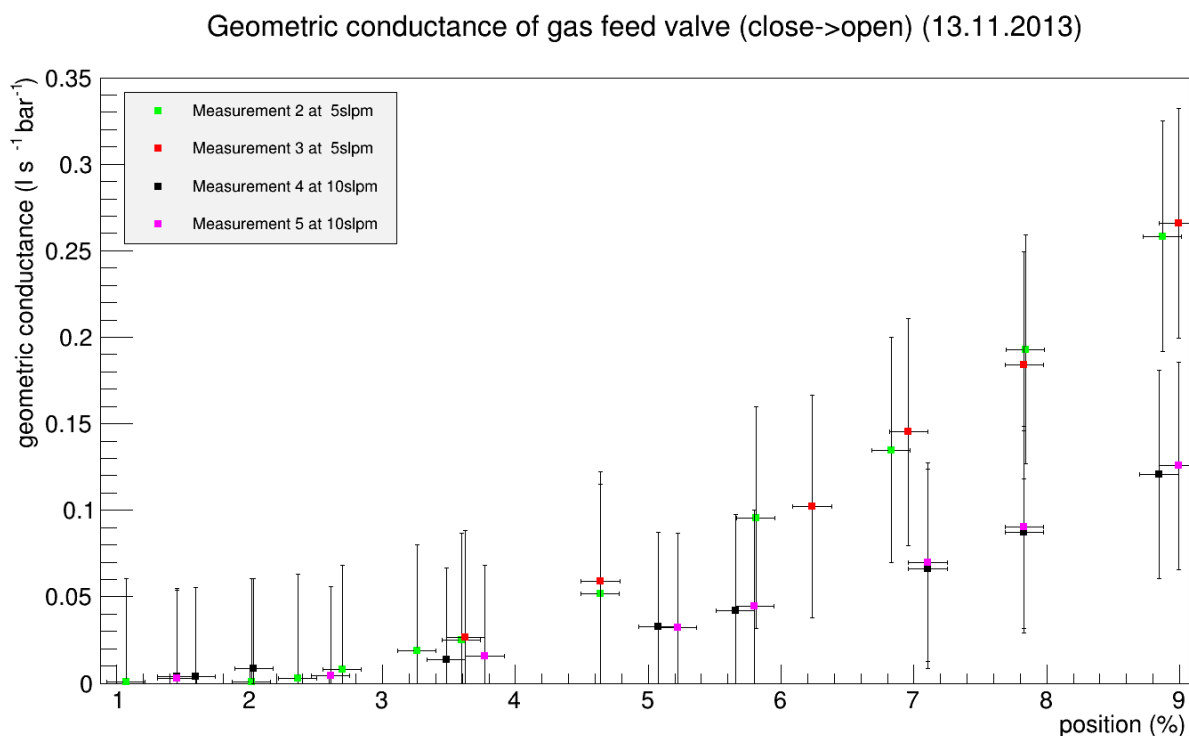
Figure 6.4: *Geometric conductance over the range of the last 9 % at two different flows starting from a open position. For fixed flow and pressure, the geometric conductance is reproducible as shown for measurement 2(green) and 3 (red) as well as for measurement 4 (pink) and 5 (black). The values of the two flows differ with a factor of about 2, which indicated that the geometric conductance is not independent from flow and pressure. That can be explained by the Reynolds numbers of 5873 and 11300 at flows of 5 slpm and 10 slpm for a fully opened valve. These values correspond to a turbulent regime in the system.*

the density is now ρ=10.21 kg/m^3 and the viscosity is η=1.43 × 10^{-5} kg/s m [NIST]. The velocities, corresponding to the flows, can be determined to be v$_5$=3.05 m/s and v$_{10}$=5.85 m/s. The Reynolds numbers for a cold regime can be calculated to be:

$$Re(5\,\mathrm{slpm})_{cold} = 9922 \qquad \text{and} \qquad Re(10\,\mathrm{slpm})_{cold} = 19\,030 \tag{6.16}$$

According to [Pfe10], a turbulent regime is prevail for Re>4000. This is already fulfilled for a fully opened valve for warm as well as for cold xenon gas and by closing more and more, these values will even increase. For turbulent flows the determination of the conductance is not trivial and will not be deeper investigated in this thesis.

However, the "proof-of-principle" for using a potentiometer as read-out for the actual valve position was shown. It is possible to reproduce the values at fixed flows and pressures.

In a next step, a reference voltage will be applied to the construction in order to monitor the position with the LabVIEW based slowcontrol. Using the slowcontrol, more detailed tests about the

Figure 6.5: *Geometric conductance over the range of the last 9 % at two different flows starting from a closed position. For fixed flow and pressure, the geometric conductance is reproducible as shown for measurement 2(green) and 3 (red) as well as for measurement 4 (pink) and 5 (black). The values of the two flows differ with a factor of about 2, which indicated that the geometric conductance is not independent from flow and pressure. That can be explained by the Reynolds numbers of 5873 and 11300 at flows of 5 slpm and 10 slpm for a fully opened valve. These values correspond to a turbulent regime in the system.*

conductance for different temperatures, flows and pressures can be done.

6.3 Filling process of the distillation column

After the system is baked out and flushed with xenon, the filling process of the distillation column can be prepared. It is divided into three major parts: Pre-cooling, filling of the reboiler and filling of the preseparator.

In a first step, the overpressure of the storage bottle is used in order to push the xenon forward through the supply line into the direction of the system, stopping at the closed input flow controller (FIC01). By opening the gas feed valve (GF1) and setting the input flow to a value of 4 slpm, gaseous xenon is added to the system. The input flow rate is stopped once the absolute pressure in the distillation column has reached a value of about 2.5 bar, which is measured with the help of all three absolute pressure sensors (PI21, PI22, PI24), as the valve GF1 is open and there is no liquid in the preseparator

and the reboiler. This value corresponds to an amount of about 28 sl xenon in the system, which can be estimated by the time interval of the opened flow controller.

In a next step, the coldhead of the top cooling tower, which is regulated by the top heat cartridges, as well as the coldhead of the preseparator are turned on and set to a fixed temperature of $-98\,°C$ and $-80\,°C$, respectively. It's not advisable to use a temperature bottom regulation for the filling, because there is no high mass transfer and thus no temperature transfer between the reboiler and the top condenser. As a consequence, a top regulation for the top condenser was chosen during the filling process. The preseparator's temperature is always regulated by its installed heat cartridges.

Due to the cooling, the xenon is liquefied at the top and streams down, pre-cooling the different components of the system. As a result, the pressure in the column decreases. After these preparations the set-up is run over night.

The next day the main filling process can be performed, which is visualised by one filling example in figure 6.6 and 6.7.

In the first figure, all important parameters are shown. Included are the input flow, the absolute pressures, the key temperatures in the preseparator, top condenser and reboiler, as well as the temperatures along the packing tube. In the second figure, the differential pressure and the four temperatures in the reboiler are displayed, providing the reboiler liquid level measurement.

P_{Column} (PI24) is the most important pressure sensor during the process, because it measures the pressure inside the packing tube. This parameter was decreased to a value of 1.75 bar during the night. The top condenser and the preseparator kept their fixed temperatures as expected. The temperature measured by the Si-diode (TIC13) as well as the four PT1000 sensors (figure 6.7, diagram 2) inside the reboiler was reduced to a value of about $10\,°C$. In the "Key temperature" plot in figure 6.6, only the interesting temperature range is shown. Due to this, the temperature of the reboiler starts to be visible after 80 min (blue line). The top packing tube sensor (TI16) had already reached the same temperature as the top condenser, while the second sensor (TI17) was cooled down to $-80\,°C$. Unfortunately, the third sensor (TI18) was defect during this measurement. The forth sensor measured a temperature of $-34\,°C$. Following the value of nearly 0 mbar, provided by the differential pressure (ΔP27) in the reboiler shown in figure 6.7, no liquid xenon was collected in the reboiler over night.

The incoming xenon is pre-cooled, yet not liquefied by the preseparator, due to the pre-set temperature of $-80\,°C$, and is guided to the very top of the column through the gas feed valve. The heat exchanger does not participate in the pre-cooling, as there is no cold liquid xenon flowing through the return line and thus through the exchanger in this process. At the top, the xenon is liquefied, streaming down the packing material and thus cooling the system from the top to the bottom. Due to the fact that the xenon is evaporated by the warm reboiler, the pressure increases as a consequence of the filling. If the pressure gets too high, the input flow is stopped, allowing the system to stabilize again. This phenomenon can be observed in figure 6.6 over the first 130 min during four time intervals at a flow rate of 4 slpm. The reduction of the temperature of the packing material, indicated by the PT1000 sensors along the tube as well as the reduction of the temperature in the reboiler, is a confirmation of an effective cooling process. At this point, a total amount of about 160 sl have been added to the distillation column.

Between 130 min and 220 min the input flow was increased step by step up to a value of 7 slpm, and yet the pressure only increased from 1.9 bar to 1.97 bar. This can be explained by the following:
The reboiler reached its operation temperature of $-95\,°C$ and as a result, the xenon was no longer
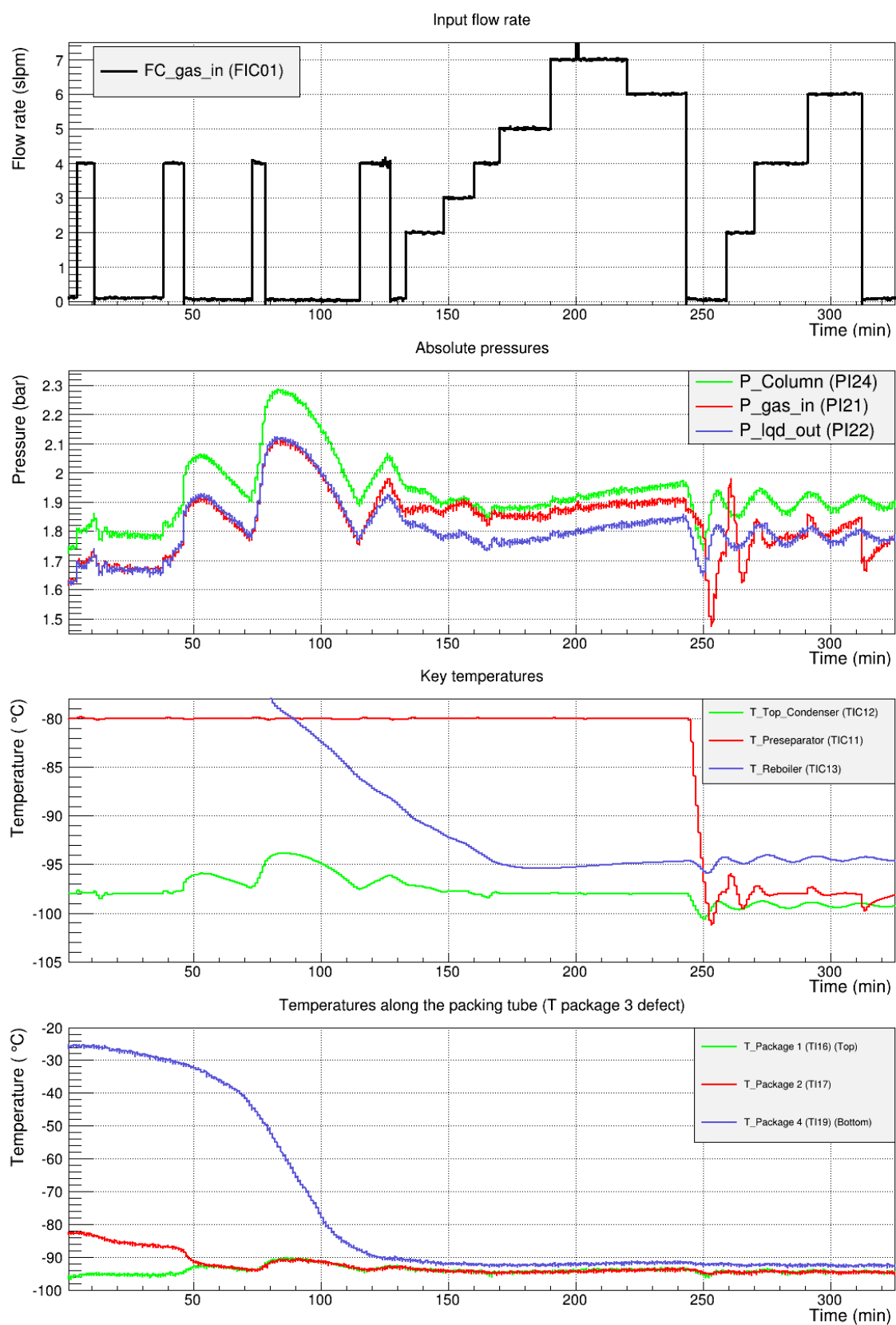
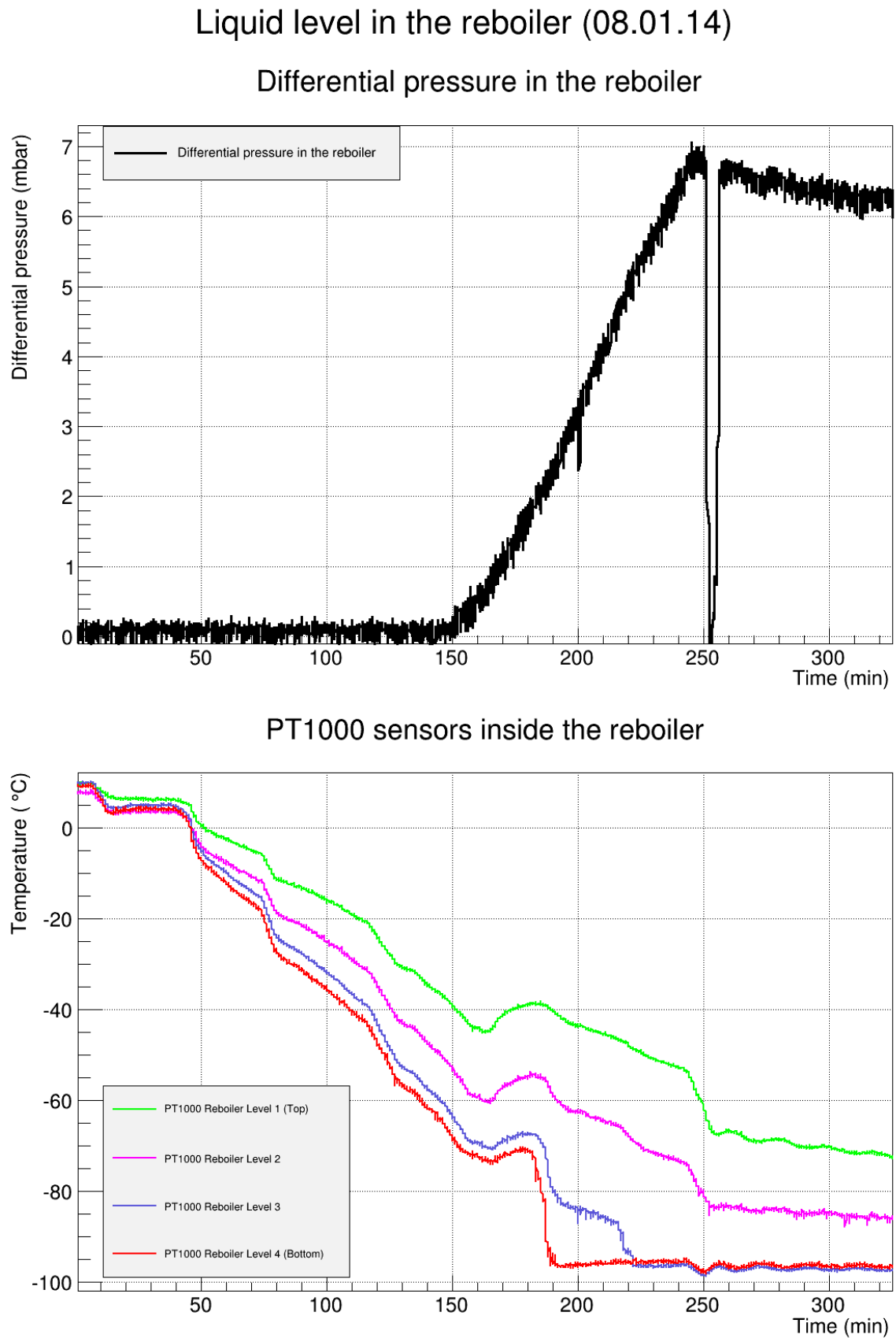Figure 6.6: *Example for a filling process of the distillation column.*

Figure 6.7: *Reboiler liquid level during the shown filling process.*

evaporated but was collected at this location, and thus, no increase in pressure could be observed. The rise of the differential pressure in the vessel, starting after 150 min, hints at an increasing liquid level. This is confirmed by the PT1000 sensors in the reboiler, shown in the bottom diagram in figure 6.7. The first sensor is covered in liquid after 190 min at a temperature of $-96\,°C$, while the second sensor follows after 220 min. Thus, the liquid level is higher than 2 cm, according to the calculations in 5.1.2. Between 220 min and 245 min, the input flow was reduced to a value of 6 slpm, and stopped afterwards. At this point, a total amount of about 710 sl have been added to the cryogenic system. Taking this into account, the amount of xenon along the packing material and thus the number of monolayers, covering the surface, can be estimated and will be presented in the next subsection.

The last step of the filling process is to fill up the input condenser with liquid xenon in order to provide a liquid feed for the distillation process. Therefore, the gas feed valve (GF1) was closed and the preseparator set-point was changed to a temperature of $-98\,°C$, which can be observed in the diagram "Key temperatures" in figure 6.6 (red line). The pressure in the preseparator dropped as a consequence of the sudden change in temperature, but stabilized again after a few minutes. The main regulation was switched to a bottom regulated pressure mode at the same time in order to prepare for the distillation process and thus the pressure in the column and the reboiler dropped as well, following the new set-point. With that, the sudden drop in the differential pressure measurement in the reboiler can also be explained. This regulation will be presented in section 6.4.

The input flow was increased step by step between 260 min and 310 min to a rate of 6 slpm and about 230 sl of xenon have been added to the preseparator.

After these three steps of the filling process, the system contains 940 sl$\approx$1000 sl, which corresponds to an amount of about 6 kg xenon, ready for a continuous distillation as explained in section 6.4.

Estimation of the number of monolayers after the filling

The concept of vapour pressure is valid once there is at least one monolayer covering the surface of the packing material as described in section 4.3. For the given design parameters a value of about 150 000 ML has been estimated. In this subsection, the number of monolayers for the given operation parameters is evaluated, using the total amount in the column as well as the amount of xenon in the reboiler:

After the main filling process, a volume of $\sim(700 \pm 20)$ sl xenon has been added to the packing tube and the reboiler, which corresponds to a total mass of about (4.2 ± 0.1) kg.

According to the PT1000 sensors in the reboiler, the liquid level is at least at a height of 2 cm. Taking the density at the given operation parameters into account, the height and thus the amount of xenon in the reboiler can be obtained by measuring the differential pressure in the reboiler as explained in section 5.1.2. With σ=2866.7 kg/m^3 at T=$-97\,°C$ and P=1.9 bar [NIST] follows:

$$h_{6.4\ mbar} = (2.3 \pm 0.1)\,\text{cm} \tag{6.17}$$

This height corresponds to a volume of about V=(1.13 ± 0.05) l, which can be translated into m$\approx(3.2 \pm 0.1)$ kg. According to the pressure of 1.9 bar, an amount of about (20 ± 5) sl of the xenon is gaseous, streaming up the tube. This equals to a mass of about (0.12 ± 0.03) kg. As a result, the remaining (0.9 ± 0.3) kg of xenon are distributed along the packing material as liquid. Under the assumption of a uniform distribution and with the required amount of m$_{Xe,ML}$=3.03×10^{-3} g of xenon for one monolayer (section

5.1.2), the total number of monolayers can be determined to be:

$$N_{ML} \sim 297\,000 \pm 47\,000 \tag{6.18}$$

According to the estimation above, the concept of vapour pressure is valid for the given parameters, used in the explained filling process.

6.4 Distillation test with bottom regulated pressure mode

During the distillation process, the amount of xenon that has to be evaporated in the reboiler due to mass conservation depends on the amount of xenon that is liquefied at the top. Therefore, a bottom regulation is favourable over a top regulation. The evaporated xenon describes a mass flow that can be translated into the pressure in the system. The heat transfer is solely a result of the mass transfer and therefore the temperature in the system follows the pressure and not vice versa. Thus, a pressure regulation is preferred for the cryogenic distillation in order to achieve a stable operation.

The results of a distillation performance test, also testing the bottom regulated pressure mode, are visualised in figure 6.8 and 6.9. During the first 280 min, which are not shown in the diagrams, the distillation column has been filled as explained above, using a top regulated temperature mode. For this measurement, the gas feed valve (GF1) has been closed and the liquid feed port LF2 at the mid height of the packing tube has been opened slightly and thus the operation was performed with a liquid feed.

The filling process from section 6.3 is not connected to this example.

The first diagram of figure 6.8 shows the process variable of the regulation mode, namely the pressure P_{Column} (PI24) inside the column tube (blue scale), as well as the corresponding control variable, namely the heating power at the bottom (red scale). The input flow rate (FIC01) is presented in the second diagram, while the differential pressure (ΔP27) in the reboiler (green scale), indicating the liquid level in the vessel, is visualised in the third diagram along with the output flow rate (FIC02) at the reboiler (blue scale). In the last diagram, the key temperatures at the preseparator, top condenser and reboiler can be observed.

The top diagram in figure 6.9 provides the information about the reboiler liquid level, indicated by the four PT1000 sensors (TI23, TI24, TI25, TI26) (black scale) as well as the differential pressure in the reboiler (grey scale). The second diagram presents the temperatures along the packing material (TI16, TI17, TI18, TI19), while in the third and fourth diagram, the differential pressure along the column (ΔP26) and the off-gas flow rate (FIC03) are shown.

As previously explained, the feed gas is provided by the overpressure of a storage bottle. The off-gas as well as the purified xenon are sucked out by using storage bottles that are cooled down with liquid nitrogen, creating an under-pressure in the bottles. With that, a bottle to bottle distillation can be performed.

In the prevailing example, the pressure inside the packing tube (figure 6.8, diagram 1) was set to a value of 1.7 bar (blue scale). The regulating heating power at the bottom (red scale) was slightly oscillating at the beginning, but converged to a constant value of about 150 W. Due to the fact that the heat cartridge at the top was not turned on, this value corresponds to the fully available cooling power for the given distillation process. The key temperatures (figure 6.8, diagram 4) at the top condenser (green line) and reboiler (blue line) are more or less constant, following the constant pressure in the
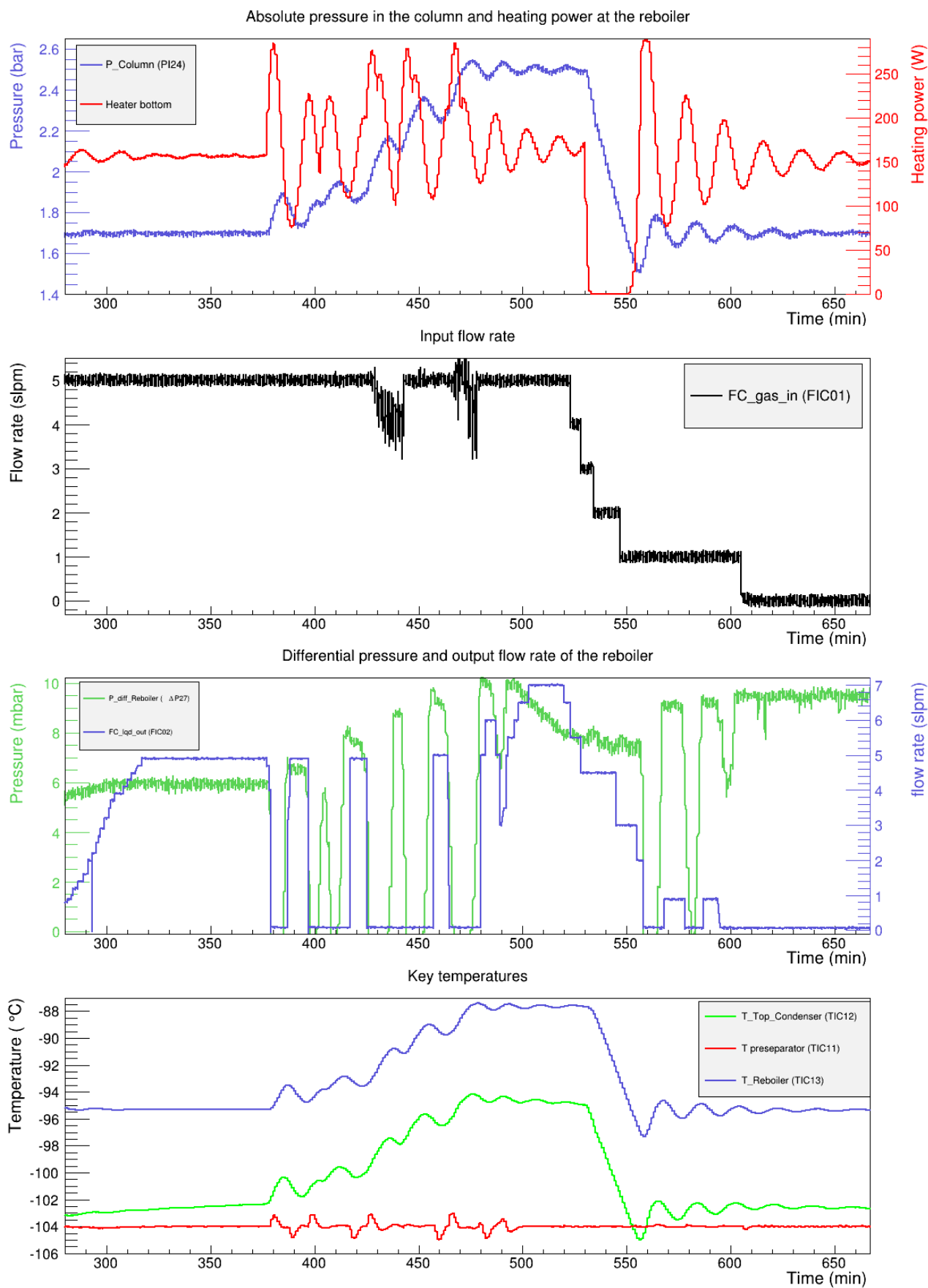
Figure 6.8: *First distillation test with pressure regulation (Page 1 from 2).*
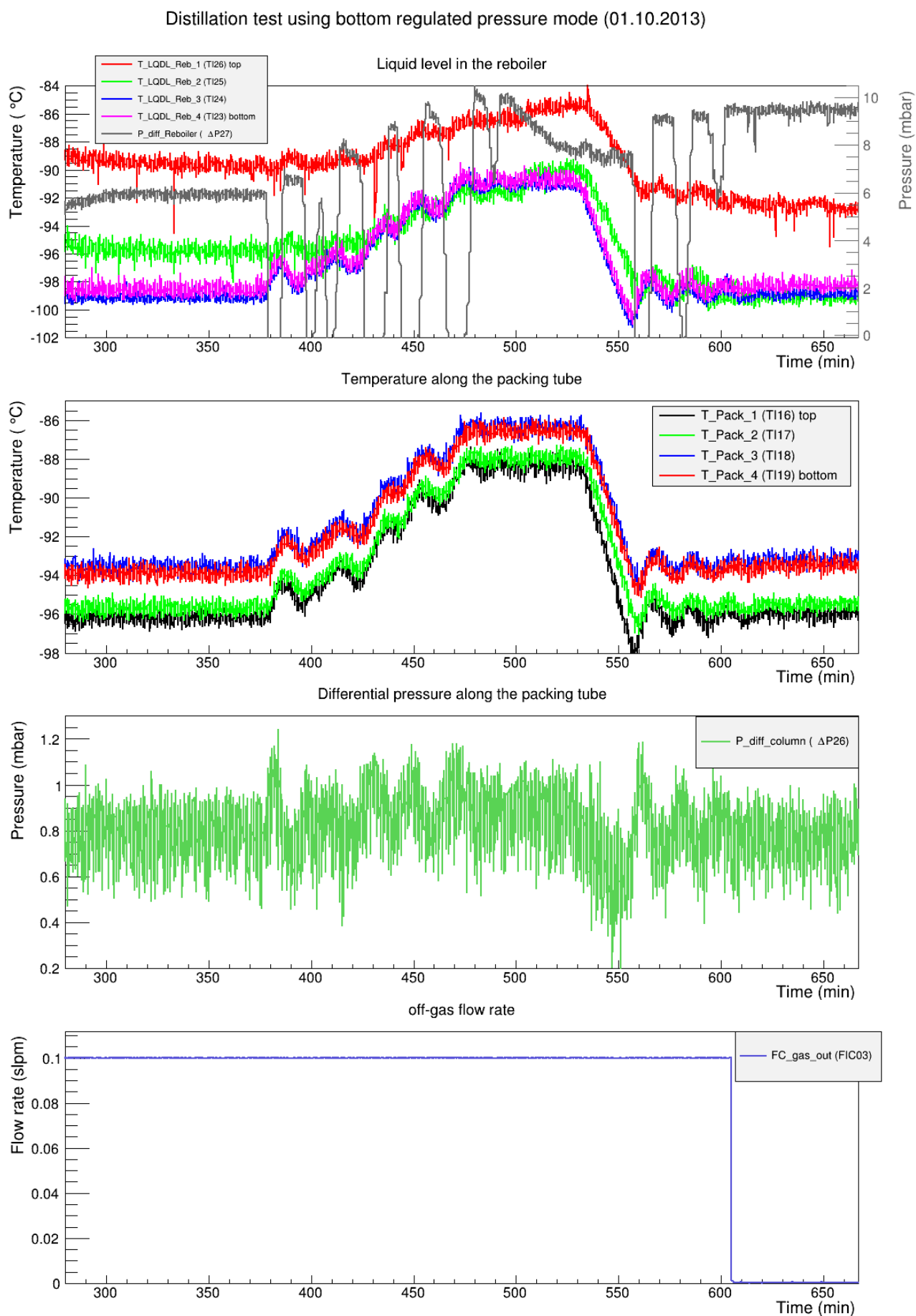
Figure 6.9: *First distillation test with pressure regulation (Page 2 from 2).*

system. The preseparator (red) is exempt from this, due to the fact that the temperature at this spot is controlled by its own heat cartridges. Furthermore the temperatures along the packing material (figure 6.9, diagram 2) as well as the temperatures in the reboiler (figure 6.9, diagram 1, black scale) are on a constant level.

The input flow (FIC01) was fixed at 5 slpm (figure 6.8, diagram 2), while the off-gas controller (FIC03) was opened to 0.1 slpm (figure 6.9, diagram 3). For a stable continuous distillation, the liquid level in the reboiler has to be kept constant, which can be monitored by keeping the differential pressure (ΔP27) along the reboiler constant. The level inside the vessel depends on the xenon that is coming down from the packing material as liquid, the amount that is evaporated as well as the amount of xenon that is taken out at the bottom of the reboiler. Thus, the level can be controlled by changing the output flow of the flow controller FIC02. An automated regulation has been implemented to the slowcontrol, but has not been tested yet. Therefore, the regulation was done manually. It can be observed (figure 6.8, diagram 3) that the output flow rate (blue scale) was increased successively between 280 min and 315 min, until it reached a flow of 4.9 slpm, while the differential pressure (green scale) had been slightly increasing, before converging to a constant level. The height of the level can be determined to be slightly more than 2 cm, according to the differential pressure of around 6 mbar and the indication by the two PT1000 sensors TI23 and TI24 in the reboiler (figure 6.9, diagram 1).

Starting from 315 min, a stable continuous distillation at a pressure of 1.7 bar, a temperature of $-103\,°C$ and a flow rate of 5 slpm was performed for about 75 min. The pressure drop along the whole column tube (figure 6.9, diagram 3) was roughly at a constant value of 0.8 mbar, which is near to the optimal operation point of 1 mbar and gives the possibility of further increasing the cooling power, using liquid nitrogen for example. In consequence, a higher mass flow in the system can be achieved and thus the separation efficiency can be enhanced. Due to the fact that this operation was taken at full cooling power, the floodpoint of the column can not be reached with the current set-up.

During this first distillation test, a ^{83m}Kr doping measurement has been taken and will be briefly presented in section 6.5.

After this "proof-of-principle", the pressure regulation was tested in more detail by trying to reach a pressure of 2.5 bar and run the system in a stable operation. Therefore, the pressure was increased in steps of 0.1 bar between 375 min and 475 min, finally reaching the defined set-point shown in the top diagram of figure 6.8 (blue scale). The heating power required for the pressure enhancement is regulated by the PID-circuit as explained in 5.4.1 and is visualised by the red scale. It is shown how the pressure responds to the heating power and vice versa during the convergence to the defined set-point. The power and thus the pressure are oscillating around the set-point with a decreasing amplitude after each regulation step. This convergence is perturbed by the fast increasing of the set-point up to 2.5 bar, but is visualised very nicely between the interval of 470 min and 530min. All temperatures in the system are following the pressure changing, except the value of the preseparator, as it was expected. The input flow and the off-gas flow are kept at 5 slpm and 0.1 slpm, respectively. Between 430 min and 450 min the pressure in the system increased to a level similar to the overpressure provided at the storage bottle and thus the input flow went down a bit. As a consequence, the overpressure of the bottle was increased, regaining the old value.

Due to the big fluctuations of the heating power, the differential pressure sensor in the reboiler was disturbed during the pressure enhancement and it can be observed that at each pressure step, the liquid level is increased up to a value of about 10.2 mbar. This is also indicated by the PT1000 sensor

TI25, corresponding to a height of 4 cm. The regulation by the output flow controller FIC02, in order to keep the level constant, was not successful. After the set-point of 2.5 bar had been reached, the output flow was set to a higher value of 7 slpm in order to reduce the liquid level. The pressure drop along the column was enhanced and oscillated around 0.9 mbar, following the key pressure.

After 530 min, the pressure in the system was directly set back to 1.7 bar without any steps in between. The previously described and explained convergence process can be observed. Again, the temperatures in the system, except for the preseparator, are following the pressure change nicely.

In addition, the input flow was reduced in steps of 1 slpm until it was fully closed, in order to see the response of the liquid level and thus of the output flow FIC02. The output flow has to be decreased in the same steps in order to keep a constant level.

After 605 min, the input as well as both output flows have been stopped and the liquid feed port has been closed. Thus, the operation was turned from a dynamic mode into a full reflux mode, which means that the full amount of xenon is streaming up and down in the column tube, while nothing is added or removed. With this mode the system can be turned into some kind of stand-by mode, giving the possibility to leave the system over night at safe conditions.

6.5 Outlook: Determination of the separation efficiency

A radioactive tracer measurement has been taken during the distillation test shown in section 6.4. The corresponding rates of the three detectors, which are proportional to the concentration of ^{83m}Kr, are shown in figure 6.10 for a time interval between 250 min and 500 min. The Rb-source has already been opened before the shown interval and the rate of the input line (gas in, green) was therefore already at about 25 Hz. The rate at the off-gas line (gas out, blue) starts to increase after the output flow is set to 0.1 slpm, converging to a constant value of about 68 Hz. Around 315 min, the equilibrium has been reached and a stable distillation was performed for about 60 min as also shown in figure 6.8.

Due to the fact that the krypton monitor at the off-gas line, which has the lowest detector efficiency, has a higher rate than the input flow, the presence of separation can be confirmed. However, the height of the separation factor can not be derived from the shown diagram alone.

Despite the fact that the flow of the return line was increased to a value of 4.9 slpm, there was no increased rate measured at this location. Calibration tests with warm xenon gas have shown that this PMT works properly and has the highest light yield. Taking this into account, there is probably no high activity in the liquid output and thus no measurable signals present. This could be an indication that there is no more krypton in the purified xenon and thus lead to the conclusion that this distillation process is highly effective. A more likely explanation would be, that the residence time of the radioactive krypton in the liquid xenon inside the preseparator as well as inside the reboiler is of such a length that most of the ^{83m}Kr has already decayed down to a level that cannot be detected by the krypton monitor.

Therefore, the residence time is a crucial parameter for the determination of the separation efficiency and needs to be investigated in great detail.

Starting from 380 min, the dependence of the measured rate from the prevail pressure can be observed. Due to the changed set-point from 1.7 bar to 2.5 bar in steps of 0.1 bar in the distillation run (section 6.4, figure 6.8), the pressure in the system is oscillating and as a result, the rate is following these
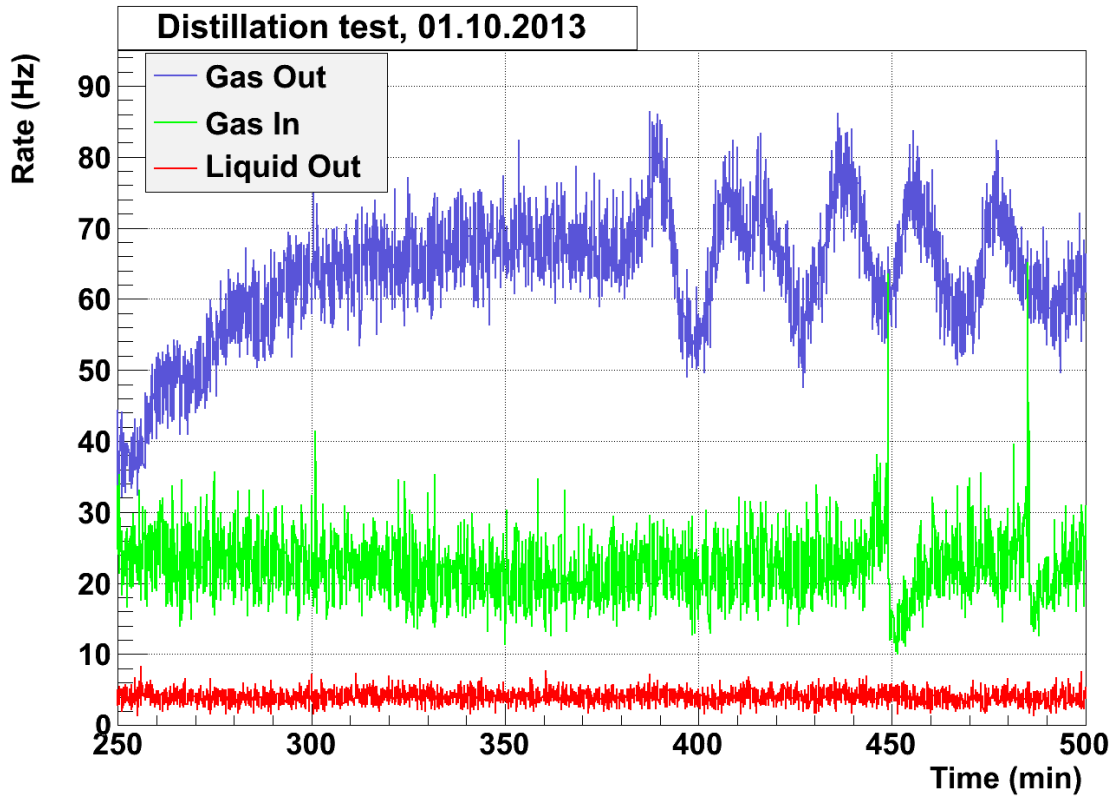
Figure 6.10: *Radioactive tracer measurement during a cryogenic distillation test. The comparison of the rate at the supply line (gas in, green), the return line (liquid out, blue) and the off-gas line (gas out, blue) indicates the presence of separation of krypton and xenon. The height of the separation factor cannot be derived from this diagram without the normalization by the prevail pressure and flow.*

fluctuations. As a consequence, a normalization of the rate by the prevail pressures and in addition by the flows is required in order to compare the different rates.

To summarize, the presence of separation from krypton and xenon has been confirmed. The determination of the height of this factor is dependent upon the detector light yield, the prevail pressures and flows as well as the residence times in the preseparator and reboiler.

In addition, a calibration measurement for the three detectors have to be taken into account. Once all parameters are characterised, the height of the separation factor can be obtained and by using this factor, the HETP-value of the structured packing material for such low concentrations of krypton in xenon can be specified.

The method is currently under further investigations and will be presented in more detail in [Ros14], along with a final determination of the efficiency.

7 Conclusion

After presenting the most compelling pieces of evidence and the properties of dark matter in the first chapter, the XENON Dark Matter Project was introduced as one experiment in the field of the direct detection of Weakly Interacting Massive Particles (WIMPs), using liquid xenon as a scattering target. The next generation experiment XENON1T, designed for one ton of fiducial xenon, is currently under construction and aims to be an entire order of magnitude more efficient in terms of sensitivity to the spin independent WIMP nucleon cross section than any other current experiments (σ_{SI}=2 × 10^{-47} cm^2). For such high detector volumes, the intrinsic contamination of xenon, such as the radioactive ^{85}Kr (β-decay, t$_{1/2}$=10.76 y, Q$_E$=687 keV), is one of the most crucial parameters for the final background level and thus the sensitivity. Allowing an upper limit of 1 evt/(y ton keV) background rate by this beta emitter, it was shown that the required concentration of ^{nat}Kr in Xe has to be on the sub-ppt level. Starting from the ppb level for commercial available xenon, krypton has to be reduced by a factor of 10^4 - 10^5. This can be done by a cryogenic distillation column, due to the difference in vapour pressure of krypton and xenon. Therefore, a new distillation column has been designed in Muenster with the help of the McCabe-Thiele method, based on the required design parameters for the XENON1T experiment. Using the obtained McCabe-Thiele diagram, in which the concentrations of krypton in the gaseous phase and in the liquid phase of xenon are plotted against each other, the number of theoretical distillation stages that are needed for the achievement of the pre-defined separation factor has been determined to be 9 for a liquid feed and 10 for a gaseous feed. In combination with the Height Equivalent for one Theoretical Plate (HETP)-value, specific for the used structured packing material, the final height of the column was calculated to be 3 m packing material and 5 m total, enlarging the HETP-value by a conservatively factor of 10.

In order to ensure easier handling and also for a number of performance tests, the project was split into two phases, starting with a height of 1 m packing material.

The complete 1 m distillation column, along with all its piping, its key components such as the pre-separator, top condenser and reboiler, its electrical wiring as well as an automated LabVIEW based slowcontrol, has been assembled during this thesis in Muenster, beginning with only one big stainless steel vessel as the starting point. The experimental set-up has been presented in detail, along with two possibilities to measure the separation efficiency, namely the ^{83m}Kr tracer method and the RGA method combined with a liquid nitrogen cold trap.

As a first test, the cooling power of the top coldhead CP140T has been obtained by measuring the heating power that is needed to keep a pre-defined temperature. At the operation temperature of 178 K for the distillation process, the cooling power was measured to be (205 ± 3) W. The comparison between the data, provided by the company Leybold, and the measured data, a heat loss of roughly (55 ± 5) W has been found, of which only 10 W can be explained by heat radiation and heat bridges. Further investigations have to be done.

However, the required cooling power of 150 W, calculated from the design values, can be provided by the installed cooling tower.

The reproducibility of the read-out of the actual position of a newly designed cold valve, using a potentiometer connected via two gears to the shaft of the valve, has been confirmed for fixed flows and pressures. A geometric conductance has been calculated in order to compare the conductance at different flows (5 slpm and 10 slpm). Due to the fact that the prevail flows have been turbulent, shown by the calculation of the Reynolds numbers for warm and cold temperatures, the geometric conductance was not independent from the flows and pressures and therefore different for the two flows.

It was shown that the system can be filled with liquid xenon, using a top regulation on the temperature of the top condenser. Applying the determination of the liquid level inside the reboiler and thus the determination of the amount of xenon inside this vessel and using the total amount that was added during the filling example, the amount of liquid xenon along the packing material has been estimated. With that, a number of $(297\,000 \pm 47\,000)$ monolayers has been obtained.

A stable distillation has been performed and was described in detail. The measurement was done at a pressure of 1.7 bar, a temperature of 170 K and a flow of 5 slpm, which is close to the given design parameters. However, just recently, a stable distillation process at a pressure of 2 bar, a temperature of 178 K and a flow of 8.3 slpm has been achieved, meeting the required design values exactly, which will be shown in [Ros14].

In addition, the separation of krypton and xenon was confirmed for the displayed process, using the radioactive tracer method, while the height of the separation factor has to be studied in more detail. Therefore, the distribution of the ^{83m}Kr in the system during a doping measurement has to be fully understood. The most crucial and yet very unknown parameter of this method is the residence time of krypton in the liquid reservoirs of xenon in the preseparator and reboiler.

Once the separation efficiency can be obtained, either by the radioactive tracer method or by the RGA method, which is currently under improvement, the dependence of this factor from different feed compositions and different heights of the feedpoint can be investigated in more detail.

Finally, after these measurements have been finished, phase two of the distillation project can be started by extending the height of the column up to 3 m packing material and a total height of 5 m, which will be the topic following this thesis.

Once the required concentration of natural krypton in xenon on the sub-ppt level is achieved, the completed set-up will be shipped to LNGS in Italy in order to obtain more than 3 tons of ultra pure xenon, which will be used as the detector material for the XENON1T experiment.

Bibliography

[Abe08] K. Abe (XMASS Collaboration), Distillation of Liquid Xenon to Remove Krypton, arXiv:0809.4413, 2008

[Amb95] M. Ambrosio et al. (MACRO Collaboration), Vertical muon intensity measured with MACRO at the Gran Sasso Laboratory, Phys. Rev. D 52 (1995) 3793.

[Ang08] J. Angle et al. XENON Collaboration, First Results from the XENON10 Dark Matter Experiment at Gran Sasso National Laboratory Phys. Rev. Let. 100, 021303 (2008)

[Apr09] E. Aprile and T. Doke, Liquid Xenon Detectors for Particle Physics and Astrophysics, Rev.Mod.Phys.82:2053-2097,2010, arXiv:0910.4956v1, (2009)

[Apr10] E. Aprile (XENON1T), XENON1T at LNGS, Technical Design Report, October 2010

[Apr11] E. Aprile et al. (XENON100), Study of the electromagnetic background in the XENON100 experiment, Phys. Rev. D 83, 082001 (2011), arXiv:11101.3866

[Apr12a] E. Aprile et al. (XENON100), The XENON100 Dark Matter Experiment, Astropart. Phys. 35 (2012), 573-590 , arXiv:1107.2155

[Apr12b] E. Aprile et al. (XENON100), Dark Matter Results from 225 Live Days of XENON100 Data, Phys. Rev. Lett. 109, 181301 (2012), arXiv: 1207.5988

[Beg91] K. G. Begeman et al., Extended rotation curves of spiral galaxies - Dark haloes and modified dynamics, Mon. Not. R. Astron. Soc. 249 (1991) 523

[Ber04] G. Bertone et al., Particle Dark Matter: Evidence, Candidates and Constraints, Phys. Rep. 405 (2005) 279-390

[Bro10] E. Brown, Search for Low Mass Dark Matter with the XENON100 Experiment and Simulations for 1 ton and 10 ton Dark Matter Detectors, PhD thesis, University of California, Los Angeles, (2010)

[Bro13] E. Brown et al., In situ measurements of Krypton in Xenon gas with a quadrupole mass spectrometer following a cold-trap at a temporarily reduced pumping speed, 2013 JINST 8 P02011, arXiv:1212.5136, 2013

[Che99] C. Y. Chen et al., Ultrasensitive Isotope Trace Analyses with a Magneto-Optical Trap, Science 286 (1999) 1139

[Clo06] D. Clowe et al., A direct empirical proof of the existence of dark matter, Astrophys.J.648:L109-L113, (2006)

[Con13] S. M. Consonni (on behalf of the ATLAS Collaboration), Higgs search at ATLAS, arXiv:1305.3315, 2013

[Des05] DESY Hamburg, Presse-Bildarchiv, `http://www-hep2.fzu.cz/ecfadesy/store/Popularizace/TeslaPhotos/susy_en.jpg`, 21.01.2012

[Fen10] J. L. Feng, Dark Matter Candidates from Particle Physics and Methods of Detection, Annu. Rev. Astron. Astrophys. 2010. 48:495–545

[Fix09] D. J. Fixsen, The temperature of the Cosmic Microwave background, Astrophys.J. 707, 916, arXiv:0911.1955v2, 2009

[Fre06] K. Freese, The dark side of the universe, Nuclear Instruments and Methods in Physics Research A 559 (2006) 337-340

[Hae81] R. A. Haefer, Kryo-Vakuumtechnik, Springer, Berlin, Heidelberg, New York, (1981)

[Han11] V. Hannen et al., Limits on the release of Rb isotopes from a zeolite based 83mKr calibration source for the XENON project, 2011 JINST 6 P10013, arXiv:1109.4270v2, 2011

[Jun96] G. Jungman et al., Supersymmetric Dark Matter, Phys. Rept., 267 (1996) 195-373

[Lev14] C. Levy-Brown, Studies of Light Propagation And Reflection off of Teflon in Liquid Xenon Detectors in the Context of the XENON100 and XENON1T Dark Matter Experiments , upcoming PhD thesis, WWU Münster, 2014

[Ley] Leybold Vakuum, Kaltköpfe - Einstufiger Kaltkopf COOLPOWER 140 T, manual

[Loh07] B. Lohrengel, Einführung in die thermischen Trennverfahren, Oldenbourg Wissenschaftsverlag GmbH, 2007

[LUX13a] LUX Collaboration, First Science Results from the LUX Dark Matter Experiment ,`http://luxdarkmatter.org/talks/20131030_LUX_First_Results.pdf`, 2013

[LUX13b] LUX Collaboration, First results from the LUX dark matter experiment at the Sanford Underground Research Facility, arXiv:1310.8214, 2013

[McC05] W. L. McCabe, J. C. Smith and P. Harriot, Unit operations of chemical engineering, McGraw-Hill Education, seventh edition, 2005

[Mon07] C. M. B. Monteiro, Secondary Scintillation Yield in Pure Xenon, JINST 2 P05001, arXiv:physics/0702142, 2007

[NIST] National Institute of Standards and Technology, homepage www.nist.gov

[Ost08] B. Ostrick, Eine kondensierte ^{83m}Kr-Kalibrationsquelle für das KATRIN-Experiment, PhD thesis, WWU Münster, 2008

[Ost03] J. P. Ostriker and P. Steinhardt, New Light on Dark Matter, Science 300 (2003) 1909

[Pfe10] Pfeiffer Vacuum GmbH, Vacuum Technology - Compendium, 2010

[Pla13a] Planck Collaboration, Planck 2013 results. XV. CMB power spectra and likelihood, arXiv:1303.5075v2, 2013

[Pla13b] Planck Collaboration, Planck 2013 results. XVI. Cosmological parameters, arXiv:1303.5076v1, 2013

[Pla13c] Planck Collaboration and ESA, Planck cosmic recipe, `http://spaceinimages.esa.int/Images/2013/03/Planck_cosmic_recipe` , 2013

[Ros14] S. Rosendahl, upcoming PhD thesis, WWU Münster, 2014

[Sch11] J. Schulz, Design of a 2-Phase Xenon Time Projection Chamber for Electron Drift Length Measurements, diploma thesis, WWU Münster, 2011

[Sel12] M. Selvi (XENON1T collaboration), Independent calculation of the number of background events due to Kr85 in LXe, internal note, 2012

[Sul] Sulzer Chemtech; 22.13.06.40 – IV.10, page 6

[Whi83] S. D. White et al., Clustering in a neutrino-dominated universe, Astrophysical Journal, 274:L1-L5, 1983

[Zwi37] F. Zwicky, On the Masses of Nebulae and of Clusters of Nebulae, Astrophys. J. 86, 217, (1937)

Danksagung